

**PERFORMANCE-BASED FRAGILITY AND RESILIENCE
ASSESSMENT OF COASTAL BRIDGES SUBJECTED TO
EXTREME WAVE LOADS**

by

Jesika Rahman

A thesis

submitted to the Faculty of Graduate Studies
in partial fulfilment of the requirements for the
Degree of Master of Science

in

Civil Engineering

Supervisor

Dr. Muntasir Billah

Assistant Professor – Dept. of Civil Engineering

Lakehead University

Thunder Bay, Ontario

August 2022

© Jesika Rahman, 2022

Author's Declaration Page

I hereby declare that I am the sole author of this thesis. This is a true copy of the thesis, including any required final revisions, as accepted by my examiners. I understand that my thesis may be made electronically available to the public.

Abstract

Bridges are vulnerable to severe damage due to extreme wave-induced loads from natural disasters, including storm surges, tsunamis, and hurricanes. The frequency of these hazards has been increasing recently as a direct impact of global warming. Enhancing the resilience of coastal bridges toward extreme waves is very important and quantification of the vulnerability of these structures is the very first step in designing a resilient bridge system. Design of most bridges in earlier times had no particular focus on the failure mechanism due to wave-induced forces. Only recently, after the collapse of the major bridges around the world due to tsunamis and hurricanes, research is being conducted to identify the resulting force and response of the coastal bridge system. However, the majority of these researches are focused on superstructure behaviour only. Therefore, studies on the response of both substructure and superstructure members of the coastal bridges are still inadequate and need to be addressed. The primary objective of this study is to identify the resilience of coastal bridges under extreme wave loads via the development of component and system-level performance-based fragility assessment using nonlinear finite element modeling in OpenSees. This study is based on numerical analysis where the finite element model of the bridge is developed considering both material and geometric nonlinearities. The modeling technique is validated against existing experimental results of a single column under cyclic lateral loading. This study also presents a simplified wave load calculation method considering the dynamic nature of the wave. The wave load calculation method is also verified and the validation results show that the difference between the numerical simulation results and the experiment is within 10%. A total of 20 bridge models having different material properties (concrete compressive and steel yield strength) and reinforcement ratios are developed for the fragility and thereby resiliency analyses. The hazard intensity measures considered for this study are wave period, wave height, and still water depth. Latin hypercube sampling technique is used to generate 100 sets of intensity parameters and therefore, a total of 100 wave force time histories are generated. Each bridge model is applied with 100 wave force time histories and the component responses are recorded each time. The engineering demand parameters include pier drift, deck transverse displacement, bearing, and shear key deformations. The wave loading analysis is divided into two scenarios where the first one depicts the case when waves reach only the piers leaving a positive clearance height between the deck and water surface whereas the second one is when waves reach the superstructure by complete inundation of the piers. Multiple stripe analysis

is used to fit the component-level fragility curves and then system-level fragility curves are generated via the series connection assumption. The study reveals that the wave period is the dominant factor affecting the wave load intensity during both scenarios. The deck level loading caused a higher probability of failure than the pier level wave loading scenario. In both loading scenarios considered, the elastomeric bearing and shear keys are found to be one of the most vulnerable components in the system-level fragility curves developed. The system fragility curves generated in this thesis are then used to assess the resiliency of coastal bridges subjected to extreme wave-induced loads. It is observed that the resiliency decreased with an increase in hazard intensity where the bridges are rendered to be in the extremely low resilient class for the lowest wave period and low resilient class due to the highest wave height considered in the study.

Acknowledgements

I express my deepest gratitude to the almighty Allah for the successful completion of my graduate study. I express my sincere gratitude to my advisor Dr. Muntasir Billah for without his first class expertise, exemplary guidance, motivation and continued support this project would not have been successful. I am grateful to Dr. Billah for giving me an opportunity to work with him as part of my graduate studies experience. I would like to thank the OpenSees community for providing the answers I needed for my simulation models. I would also like to thank Vahid Aghaei Doost for helping me develop and debug the OpenSees bridge models. I gratefully acknowledge the support of the Natural Sciences and Engineering Research Council of Canada (NSERC) and the Faculty of Engineering, Lakehead University to pursue my graduate degree. I would also like to thank my friends and well-wishers for without their company and encouragement this journey would have been difficult. Finally, I am immensely thankful to my parents for always being there when I needed them the most and providing continuous guidance, support and inspiration.

Table of Contents

Abstract.....	iii
Acknowledgements.....	v
List of Tables	ix
List of Figures.....	x
Nomenclature.....	xiii
Chapter 1 Introduction	1
1.1 Background.....	1
1.2 Scope of The Study.....	3
1.3 Thesis Outline	4
Chapter 2 Literature Review.....	5
2.1 Introduction.....	5
2.2 Characterisation of Wave-Induced Forces.....	5
2.3 Wave theories.....	7
2.4 Wave load on superstructures	12
2.4.1 Previous Experimental Studies	13
2.4.2 Previous Numerical Studies.....	15
2.5 Wave load on substructures	22
2.5.1 Piers.....	22
2.5.2 Piles.....	23
2.6 Design guidelines.....	27
2.6.1 AASHTO (2008) Guide Specifications for Bridges Vulnerable to Coastal Storms....	27
2.6.2 ASCE 7-16 Minimum design loads for buildings and other structures	27
2.6.3 Canadian Highway Bridge Design Code (CSA S6:19)	28
2.7 Fragility Assessment Studies	28

2.8 Resiliency Assessment Studies	30
2.9 Summary	31
Chapter 3 Finite Element Modeling of the Bridge and Wave Load Calculation Method	34
3.1 General	34
3.2 Description of the case study bridge	34
3.3 Numerical Model of the Bridge	36
3.3.1 Material and Section Properties	36
3.3.1.1 Abutment Backfill Soil	37
3.3.1.2 Elastomeric Bearing	38
3.3.1.3 Shear Keys	39
3.3.1.4 Pounding Element	40
3.3.2 Validation of the numerical model	41
3.4 Wave Load Calculation Method	42
3.4.1 Validation of the wave load calculation method	45
3.5 Summary	46
Chapter 4 Methodology and Development of Performance-based Damage States	47
4.1 General	47
4.2 Methodology	47
4.2.1 Parameter Uncertainty	48
4.2.2 Variation in Component Demands	50
4.3 Damage State Definition	53
4.3.1 Derivation of pier drift-based damage states	56
4.4 Summary	61
Chapter 5 Fragility and Resiliency Assessment of Coastal Bridges under Wave loading	63
5.1 General	63

5.2 Fragility Assessment.....	63
5.2.1 Fragility Analysis Results	64
5.3 Resiliency Assessment.....	72
5.4 Details of Resiliency Assessment Framework.....	74
5.4.1 Resiliency Analysis Results.....	78
5.5 Summary	90
Chapter 6 Conclusions and Future Works	91
6.1 Summary.....	91
6.2 Core Contributions.....	91
6.3 Conclusions	92
6.3.1 Literature Review.....	92
6.3.2 Wave Load Calculation Method	92
6.3.3 Variation in Component Demands and The Most Affecting Wave Parameter	93
6.3.4 Damage State Definitions	94
6.3.5 Fragility Curve Analysis	95
6.3.6 Resilience Assessment Results	95
6.4 Recommendation for Future Studies	96
References.....	98
Appendices.....	111
Appendix A.....	111
Appendix B.....	115

List of Tables

Table 2-1 List of available literature based on different field of wave load studies (excluding studies on wave loads on coastal structures).....	9
Table 2-2 Effect on wave forces due to wave parameters.	10
Table 2-3 Effect on wave forces due to bridge components.....	11
Table 2-4 Comparison of studies with published empirical equations.....	26
Table 2-5 Summary of bridge fragility analysis under extreme wave loads	32
Table 4-1 Uncertainties considered in fragility analysis.....	49
Table 4-2 Pier drift-based damage states adopted in the study.....	55
Table 4-3 Damage states adopted for the components	56
Table 4-4 Definition of the probabilistic distribution functions chosen for goodness-of-fit tests	57
Table 4-5 K-S goodness-of-fit test results at $\alpha = 5\%$ for the chosen distributions to represent the drift data obtained in scenario 1.....	59
Table 4-6 K-S goodness-of-fit test results at $\alpha = 5\%$ for the chosen distributions to represent the drift data obtained in scenario 2.....	60
Table 4-7 Limiting drift values and their corresponding best fit distribution by K-S tests.....	61
Table 5-1 Typical recovery functions used in literature	74
Table 5-2 Definition and distribution of variables used to derive the recovery functions	76
Table 5-3 Resilient ranking scale (Minaie and Moon 2017)	79

List of Figures

Figure 1-1 Typical failures of bridges subjected to extreme waves (a) components of a bridge before hazard event, (b) unseating of the deck, (c) damage to piers when deck to substructure connection is strong and (d) uplift and displacement of footing [adopted from Qeshta (2019)].....	3
Figure 2-1 Classification of wave forces and their corresponding direction on bridge components	6
Figure 2-2 Bridge parameters[adapted from Qeshta et al. (2019)].....	7
Figure 2-3 Linear and non-linear waves [adapted from (Aguñiga et al. 2008)].....	12
Figure 2-4 Schematic representation of total vertical wave load as reported by Ataei et al. (2010).	17
Figure 2-5 Comparison of horizontal and vertical wave loads on decks as reported by Hayatdavoodi and Ertekin (2014).....	18
Figure 2-6 Variation of total horizontal wave force time history due to difference in pier cross-sections by Rahman and Billah (2021)	23
Figure 2-7 Comparison of horizontal wave load time history on bridge piles as reported by Ti et al. (2019).	25
Figure 3-1 Details of the case study bridge (a) elevation view and (b) transverse view at section A-A (The dimensions shown are in mm).	35
Figure 3-2 Numerical model of the bridge pier (a) Displacement-based nonlinear beam column element and (b) Fiber discretization adopted for the piers. (The dimensions shown are in mm).	37
Figure 3-3 Force displacement response of abutment backfill soil	38
Figure 3-4 Force displacement response of elastomeric bearing pad	39
Figure 3-5 Force displacement response of shear keys	40
Figure 3-6 Force displacement response of the impact (pounding) element	41
Figure 3-7 Numerical model technique validation using results of column A2 from Kunnath et al. (1997).....	42
Figure 3-8 Total wave force time history in (a) vertical and (b) horizontal directions	45
Figure 3-9 Validation of wave load calculation method using experimental results from (a) Xiong et al. (2020) and Hong et al. (2021)	45

Figure 4-1 Schematic diagram of wave propagation towards a bridge structure showing (a) scenario 1 and (b) scenario 2 [adapted from Balomenos and Padgett (2018)]	48
Figure 4-2 Framework adopted to develop fragility curves of coastal bridges subjected to extreme waves.....	49
Figure 4-3 Variation in maximum component responses due to scenario 1 on B1	51
Figure 4-4 Variation in maximum component responses due to scenario 2 on B1	51
Figure 4-5 Variation of drift levels in four bridge piers for scenario 1 due to (a) W2 and (b) W5 combinations	52
Figure 4-6 Variation of drift levels in four bridge piers for scenario 2 due to (a) W2 and (b) W5 combinations	53
Figure 4-7 Schematic diagram showing the measurement of shear deformation of the elastomeric bearing pad	54
Figure 4-8 Distribution of the pier drift values corresponding to the four DS for (a) scenario 1 and (b) scenario 2.....	61
Figure 5-1 Process of fitting the fragility curve using MSA (a) Identification of fractions exceeding a DS, (b) Fitting of fragility curve, (c) Compilation of fitted fragility curves across all four DSs	65
Figure 5-2 Fragility curves for the pier drift corresponding to (a and b) ω for scenario 1 and 2, (c and d) H_w for scenario 1 and 2, and (e) d_s for scenario 1	67
Figure 5-3 Fragility curves for the deck transverse displacement corresponding to (a and b) ω for scenario 1 and 2, (c and d) H_w for scenario 1 and 2, and (e) d_s for scenario 1	68
Figure 5-4 Fragility curves for the elastomer bearing deformation corresponding to (a and b) ω for scenario 1 and 2, (c and d) H_w for scenario 1 and 2, and (e) d_s for scenario 1	69
Figure 5-5 Fragility curves for the shear key deformation corresponding to (a and b) ω for scenario 1 and 2, (c and d) H_w for scenario 1 and 2, and (e) d_s for scenario 1	70
Figure 5-6 System fragility curves for scenario 1 corresponding to (a) ω , (b) H_w and (c) d_s	71
Figure 5-7 System fragility curves for scenario 2 corresponding to (a) ω and (b) H_w	72
Figure 5-8 Schematic diagram defining resilience of a structure before and after a hazard event	73
Figure 5-9 Schematic diagram of recovery functions at different damage stages chosen for this study	77
Figure 5-10 Framework adopted for resilience assessment in this study	77

Figure 5-11 Functionality index and variation in resilience index due to wave periods at (a and b) 13.5 sec, (c and d) 12.6 sec, (e and f) 12 sec of scenario 1	80
Figure 5-12 Functionality index and variation in resilience index due to wave periods at (a and b) 13.5 sec, (c and d) 12.6 sec, (e and f) 12 sec of scenario 2	82
Figure 5-13 Functionality index and variation in resilience index due to wave heights at (a and b) 2m, (c and d) 3.42m, (e and f) 3.84m of scenario 1	84
Figure 5-14 Functionality index and variation in resilience index due to wave heights at (a and b) 2m, (c and d) 3.42m, (e and f) 3.84m of scenario 2	86
Figure 5-15 Functionality index and variation in resilience index due to still water depths at (a and b) 7.2m, (c and d) 8m, (e and f) 9.51m of scenario 1.....	88
Figure 5-16 Variation in mean resilience index corresponding to (a) T_w and (b) H_w	90

Nomenclature

Symbols

$A_{bearing}$	Cross sectional area of bearing pad
A_g	Gross area of column cross-section
A_h	Projected area in the horizontal plane
A_v	Projected area in the vertical plane
C_d	Drag force coefficient
C_m	Inertia force coefficient
C_s	Slamming force coefficient
d	Shear key depth
D	Statistic measure of the Kolmogorov-Smirnov test
$D_{critical}$	Critical D value for K-S test
d_g	Girder height
DS	Damage state
d_s	Still water depth
D_{stat}	D statistics of the Kolmogorov-Smirnov test
e	Coefficient of restitution
E_s	Young's modulus of transverse steel
$F(x_i)$	CDF of the chosen probability distribution for the K-S test
F_b	Buoyancy force
f_c'	Concrete compressive strength
F_d	Drag force
F_i	Inertia force
f_{rec}	Recovery function
F_s	Slamming force
$F_{t,h}$	Total wave force in the horizontal direction
$F_{t,v}$	Total wave force in the vertical direction
F_{ult}	Ultimate passive resistance of backfill soil
f_y	Steel yield strength
F_y	Yield force

f_{ys}	Transverse steel yield strength
g	Gravitational acceleration
$G_{bearing}$	Shear modulus of bearing pad
h	Shear key height
$H(\cdot)$	Heaviside step function
$h_{bearing}$	Total bearing pad thickness
H_w	Wave height
k	Wave number
K_{eff}	Effective stiffness of pounding element
k_h	Spring constant
K_{max}	Initial stiffness of abutment backfill soil
K_{pad}	Bearing pad stiffness
K_{t1}, K_{t2}	Initial and post yield stiffness of pounding element
L	Span length
L_a	Width of abutment front wall
L_b	Reinforcement development length
m	Number of IM analysis
n	Number of samples (K-S Test D statistic)
n_{Hertz}	Hertz coefficient
n_j	Number of analysis at each IM
P	Axial load on column
P_j	Probability of the component to exceed a particular DS
$Q(t)$	Functionality with respect to time
Q_b	Bounced back functionality
Q_r	Residual functionality
R	Resilience index
R_f	Failure ratio of backfill soil
S	Spacing between adjacent girders
s	Spacing of reinforcement
t	Instantaneous time
t_0	Time when the hazard event took place

t_h	Investigated time horizon
T_w	Wave period
u	Wave particle velocity in horizontal direction
\dot{u}	Wave particle acceleration in the horizontal direction
U_4	Displacement of shear keys corresponding to the spalling or cracking reaches the entire region of concrete
U_5	Displacement of shear keys corresponding to fracture of steel reinforcement
U_n	Displacement of the shear keys corresponding to large crack or spalling of the concrete
U_y	Displacement corresponding to yielding of steel reinforcement of the shear keys
V_s	Submerged volume
W	Deck width
w	Wave particle velocity in the vertical direction
\dot{w}	Wave particle acceleration in the vertical direction
x_i	Data arranged in ascending order for fragility curve fitting
Y_{ave}	Displacement corresponding to half the ultimate passive resistance
Y_{max}	Maximum abutment displacement
z	Vertical location of wave particle with respect to still water depth at a time instant
z_j	Number of component responses exceeding a DS
α	Significance level
β	Dispersion value of the IM in fragility analysis
δ_i	Idle time interval
δ_m	Maximum displacement
δ_r	Recovery duration
δ_y	Yield displacement
$\varepsilon_{buckling}$	Strain corresponding to longitudinal rebar buckling
ε_{cu}	Strain corresponding to concrete crushing
ε_{sm}	Strain of steel at maximum tensile stress
η	Water surface elevation
θ	Median value of the fragility function
λ	Wavelength

μ	Coefficient of friction of bearing pad
ρ	Density of sea water
ρ_{sv}	Volumetric ratio of transverse steel
ρ_s	Longitudinal reinforcement ratio
σ	Standard deviation
σ_n	Normal stress
ω	Wave frequency

Abbreviations

CDF	Cumulative distribution function
DS	Damage state
EDF	Empirical distribution function
EDP	Engineering demand parameter
FE	Finite element
FSI	Fluid structure interaction
IM	Intensity measure
K-S	Kolmogorov-Smirnov test
LHS	Latin hypercube sampling
PDF	Probability density function
RC	Reinforced concrete
Tcl	Tool command language

Chapter 1 Introduction

1.1 Background

Resilience to natural hazards has been one of the biggest challenges for both coastal and offshore structures. During the events such as earthquakes, tsunamis, hurricanes, floods and storm surges, it is imperative that the transport facilities perform satisfactorily to minimize the risk of collapse as much as possible. The continuous development of coastal infrastructures coupled with more frequent and severe natural disasters taking place in recent times require prevention and recovery strategies during the very early stages in design (Dale et al. 2001, Knutson et al. 2010, Neumann et al. 2015). Since bridges are one of the lifeline structures that link between important facilities, maintaining the desired performance level during and post hazard situations is of high importance. A detailed analysis of the forces that arise due to the site conditions, specific climate and the location of bridge is very important.

Overcoming the impacts of natural hazard on coastal communities is a major challenge, especially as tsunamis and hurricanes are more frequent due to global warming (Holland 2012, Imamura et al. 2019, Emanuel 2020). The unprecedented rise in sea level posed a substantial threat to coastal transportation as the systems are designed based on earlier provisions where the loading mechanisms imposed from these hazards were not included, thus leading to inadequate design. Collapse of coastal bridges are observed due to Ivan (2004), Katrina (2005), Wilma (2005) hurricanes, Tohoku tsunami (2011) and typhoon Haiyan (2013) (Douglass et al. 2004, Robertson et al. 2007, Lukic and Auditor 2009, Kawashima and Buckle 2013, Mas et al. 2015). One of the most expensive disasters affecting the coastal community in the US is Hurricane Katrina (2005) where the overall cost of replacing the damaged bridges was over 1 billion US dollars (Padgett et al. 2008). Enhancing the resilience of coastal bridges towards these natural hazards is of prime importance as these damaged structures not only disrupts traffic and cause economic loss, but delays rescue operations as well (Balomenos et al. 2019). Hurricanes are caused by the greenhouse gas effect where the sea level is seen to rise due to the warm air and low tropical pressures (NOAA 2020). Tsunamis are created due to sudden displacements of the ocean floor, primarily due to earthquakes or volcanic eruptions (Palermo et al. 2013). Extreme waves are a common phenomenon during these hazards (e.g. hurricane, tsunami) affecting the resilience of structures.

Therefore, quantification of wave-induced forces and the corresponding behaviour of the structural components are important for the prevention of potential calamities.

Typical failures of bridges exposed to extreme waves include unseating of bridge decks, failure of substructure to deck connections, and damage to the piers (Ataei et al. 2010, Ataei and Padgett 2013, Balomenos and Padgett 2018, Qeshta 2019, Balomenos et al. 2020). Figure 1-1 illustrates the typical damages seen in bridges due to extreme waves. The severity of the applied wave-induced load varies depending on the location of the structure. Bridges closer to the coast are subjected to lower inundation depth and higher wave heights compared to offshore bridges. As the wave heights are higher, the severity of wave action on the coastal bridges is also higher (Mo et al. 2007). The concept of wave formation is typically described using linear and nonlinear wave theories. Linear wave theory assumes waves to be in simple harmonic motion (Dean and Dalrymple 1991). Nonlinear wave theory is adopted when the linearity is disrupted due to high winds and other natural factors creating waves with sharper crests compared to the linear waves (Aguñiga et al. 2008). Moreover, waves are generally characterized in two types namely the solitary waves which travels without any change in size, and the periodic waves where wave lengths are shorter than that of solitary waves (Cai et al. 2018). Wave induced forces consist of components in both horizontal and vertical directions where the vertical component of the force acting on the superstructure is typically higher than the horizontal component. The wave forces depend on several parameters such as wave height, wave period, still water depth. It is also noted that bridge geometries namely pier cross-section type, pier height, deck width, deck slab thickness, girder type, girder spacing and even presence of nearby structures affect the intensity of wave loads. According to Bonakdar and Oumeraci (2015), wave load on a single slender pile of a pile supported structure is significantly affected by the surrounding piles.

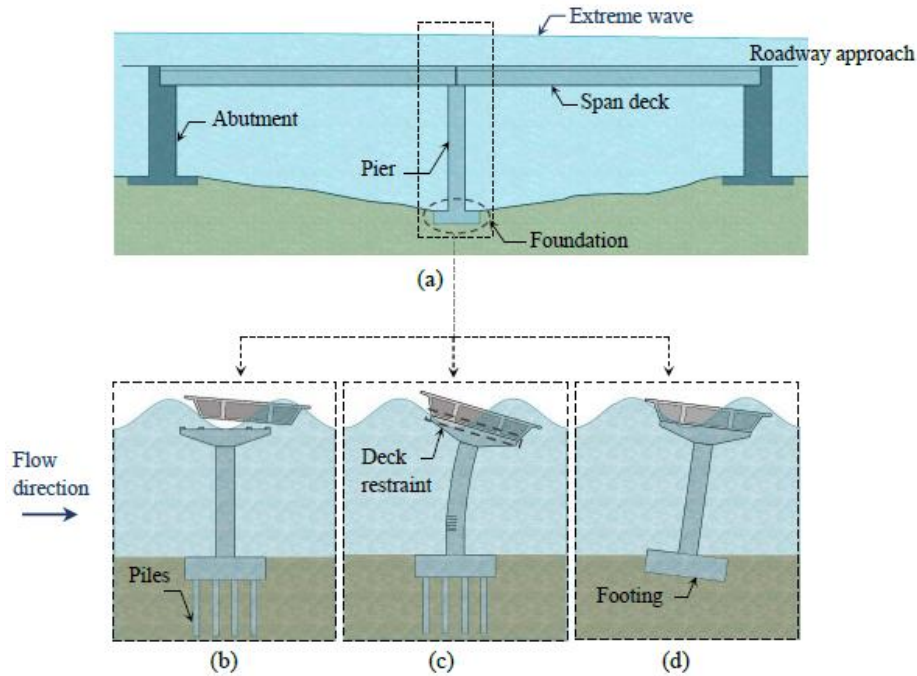


Figure 1-1 Typical failures of bridges subjected to extreme waves (a) components of a bridge before hazard event, (b) unseating of the deck, (c) damage to piers when deck to substructure connection is strong and (d) uplift and displacement of footing [adopted from Qeshta (2019)]

1.2 Scope of The Study

Although there exists a number of researches regarding the behaviour of bridges under extreme wave-induced loads, studies addressing the development of a simplified framework for resilience assessment of the system is scarce. Moreover, no damage states are developed to quantify the wave-induced failure probability assessment of the substructure from the material response, especially the piers. This research addresses this gap in literature and presents a simplified technique to quantify the performance of a typical three span coastal bridge subjected to a wide range of extreme wave-induced loads. This thesis aims to develop the component and system fragility curves and quantify the resilience of coastal bridges subjected to extreme wave loads generated from tsunamis and hurricanes. The research objectives are summarized as follows:

1. To identify the most accurate wave load estimation formula verified by available experimental results and determine the factors affecting the intensity of wave loads.
2. To develop performance-based drift limit states of the substructure component (piers) under extreme wave-induced loads using the material strain-based detection method.

3. To develop a simplified framework and generate component and system-level fragility curves with respect to the hazard intensity parameters considered.
4. To assess the resiliency of the bridge system under various hazard intensity levels.

1.3 Thesis Outline

The thesis is organized in six chapters outlined as follows:

Chapter 1. This chapter provides a general introduction of wave load effects on bridges together with the scope and objectives of this thesis.

Chapter 2. A detailed discussion of past studies aligning with the objectives of this thesis including wave load calculation methods, factors affecting wave load intensity, performance-based limit state development and thereby component and system-level fragility analysis and resiliency assessment are presented in this chapter. A research gap based on the accuracy of time-varying wave force calculation and consequently the assessment of coastal bridge components (especially the substructure) failure probability due to these loads is identified.

Chapter 3. Development and validation of finite element model of the bridge is discussed in this chapter including descriptions of material properties, boundary conditions, fiber discretization and loading protocol. Details of the wave force time history calculation method adopted and its corresponding validation using available experimental studies are also discussed.

Chapter 4. Methodology adopted to derive the component and system-level fragility curves is detailed in this chapter. This chapter also includes the variation of component demands due to changes in the hazard intensity parameters considered. Lastly, the development of performance-based limit states for piers and definition of the limit states of deck transverse movement, elastomeric bearing and shear keys are described in detail.

Chapter 5. Component and system-level fragility curves are generated and analyzed in this chapter. The fragility analysis results are then used to derive the resiliency of the bridge system towards the extreme wave hazard intensities considered.

Chapter 6. The main conclusions and recommendations for future studies is presented in this chapter.

Chapter 2 Literature Review

2.1 Introduction

A number of studies regarding wave action on bridges have been done. However, each study focused on a particular research area among the following: the wave-induced force on superstructures (decks) (Douglas et al. 2006, Jin and Meng 2011, Guo et al. 2015) or substructures (piers and pile groups) (Morison et al. 1950, Bonakdar et al. 2015, Wang et al. 2019), hydrostatic forces (Douglas et al. 2006, Carey et al. 2019), slamming and impulse forces (Navaratnam et al. 2013, Moideen et al. 2019), location of the bridge (coastal and offshore) (Bea et al. 1999, Hayatdavoodi and Ertekin 2014), linear or non-linear wave theory considerations (Kafali 2008, Gullett et al. 2012, Azadbakht and Yim 2015, Seiffert et al. 2015, Hayatdavoodi et al. 2019), numerical simulation of wave properties using fluid–structure interaction (FSI) (Ataei and Padgett 2015, Carey et al. 2019), experimental investigation using wave flumes (Marin and Sheppard 2009, Sheppard and Marin 2009, Zhang et al. 2020), simplified modeling of wave force on the structure (Kameshwar and Padgett 2014, Zhu et al. 2018), analysis of reaction forces due to loads from the simulated wave fields (Hayatdavoodi and Ertekin 2014, Azadbakht and Yim 2015), superstructure either being partially or fully submerged in the sea-water (Hayatdavoodi and Ertekin 2014, Guo et al. 2015, Hayatdavoodi et al. 2019). Moreover, there are several codes addressing the design of bridges in shallow and deep waters (US Army 1984, AASHTO 2008, ASCE 2016). Most of the papers reviewed in this study are based on coastal structures, however, a list of the publications regarding variation in the research fields as discussed above is presented in Table 2-1.

2.2 Characterisation of Wave-Induced Forces

The wave parameters taking part in wave-induced loads are wave period (T_w), wave height (H_w), still water depth (d_s), wave length (λ), wave frequency (ω), water surface elevation (η) and clearance height (z_c) (Sheppard and Marin 2009, Gullett et al. 2012, Qeshta et al. 2019). The wave period (T_w) is defined as the time taken by the sea water wave to complete one cycle. The maximum height reached by the wave from the crest to its neighbouring trough is termed as the wave height. Wave length (λ) represents the distance between two crests/troughs. Similar to sound waves frequency, the water wave frequency is inversely proportional to the T_w . The clearance height (z_c) is the distance between the still water level and the bottom of deck, it is positive when the still water is below the deck and negative when it is above the deck level. These parameters are used

to calculate the total wave load which is principally divided into three main components. The hydrodynamic component includes drag and inertia forces. These are vertical and horizontal forces due to the normal and shear stresses resulting from the inertia against steady-state flows with moderate to high velocity (Azadbakht and Yim 2015). The hydrostatic component is termed as the uplift or buoyancy force resulting from the volume of displaced water due to the submergence of the structure (Finnemore and Franzini 2002). The highly transient forces are termed as impact (slamming) forces caused by the air entrapment and momentum transfer when wave hits the structure (Azadbakht and Yim 2016). The drag, inertia and buoyancy forces are often collectively termed as quasi-static forces. One important factor in accurate estimation of wave force is the coefficient corresponding to each of these components. Several empirical and experimental studies are conducted to determine the most suitable values for the coefficients of drag, inertia and slamming force components (Marin and Sheppard 2009, Sheppard and Marin 2009, Gullett et al. 2012, Montoya et al. 2019). Figure 2-1 shows how the total wave force is classified into different components and their line of action on the superstructure and substructure.

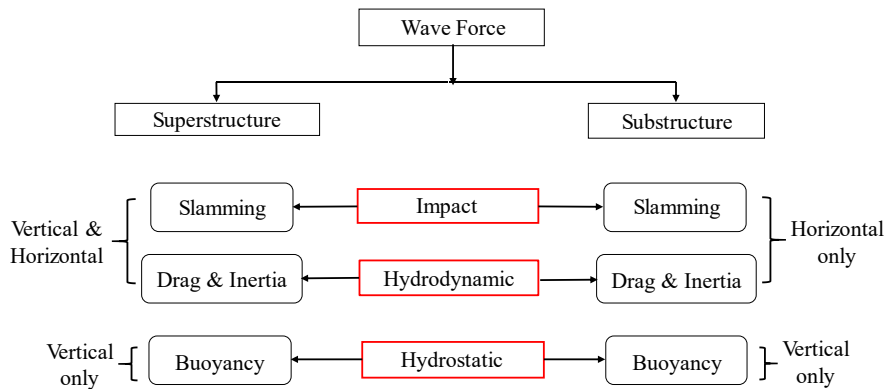


Figure 2-1 Classification of wave forces and their corresponding direction on bridge components

In studies regarding wave loading on structures, the wave conditions are mostly obtained from actual hurricane and tsunami data available from official database involving hind cast (Marin and Sheppard 2009, Sheppard and Marin 2009, Gullett et al. 2012, Kameshwar and Padgett 2014). Some studies have also used assumptions basing on the hydrological conditions of the bridge site (Ataei et al. 2010, Ataei and Padgett 2013, Zhu et al. 2018). Extreme wave conditions are adopted by researchers from the data of wave conditions having return periods such as 25, 100, 300 and even 2500 years (Azadbakht and Yim 2015, Zhu et al. 2018, Ti et al. 2019). It is often seen that Froude scaling is applied to scale the wave profiles in order to replicate the realistic site conditions

in numerical and experimental analysis (Sheppard and Marin 2009, Gullett et al. 2012, Alam et al. 2018). The effect of variation in hazard parameters on the wave-induced loads is summarized in Table 2-2. The parameters relating to bridge geometry that affect the wave load being applied include deck width (W), deck slab thickness, girder height (d_g), span length (L), girder spacing (S), pier cross section, number of girders and railings. Figure 2-2 presents the geometrical parameters of a typical girder bridge subjected to wave actions. Table 2-3 summarizes the effect of bridge geometry variations on the wave load being applied on it. Table 2-4 presents a summary of literature where the results of their studies were compared with other published empirical equations.

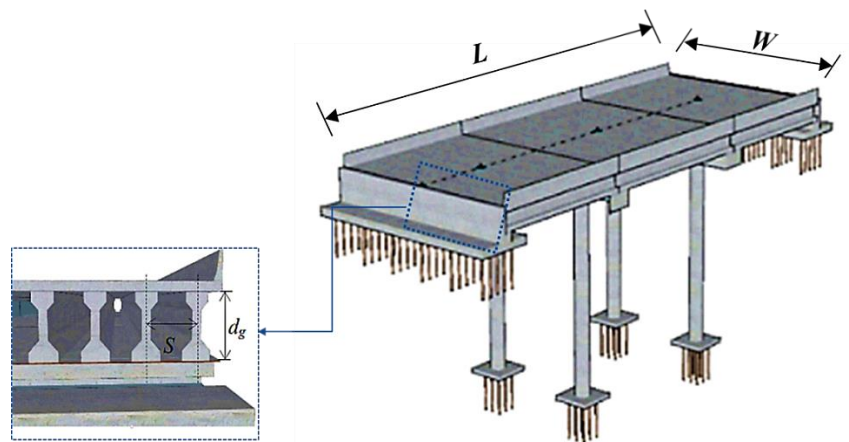


Figure 2-2 Bridge parameters[adapted from Qeshta et al. (2019)]

2.3 Wave theories

The concept of wave formation is commonly described using the linear and nonlinear wave theories. Linear wave theory is the simplest one that assumes the fluid to be incompressible, no dissipation of energy takes place, wave height is smaller than the wave length and still water elevation. Nonlinear wave theory is adopted when natural factors such as wind from different directions disrupts the linearity of wave profile (Aguñiga et al. 2008). Nonlinear waves have sharper crests compared to the linear waves as shown in Figure 2-3. These nonlinearity of wave profiles are often described using the Navier-Stokes wave theory, irregular and cnoidal wave theories, details of which can be found in Ertekin et al. (2014) and Azadbakht et al. (2015). An irregular wave theory is considered when the wave profile is assumed to contain a series of waves having different frequencies and amplitudes. This theory is modeled assuming a linear

superposition of a number of independent regular waves with different frequencies, amplitudes and phases (Zhu et al. 2018). The Green-Naghdi water wave theory, namely the Level 1 GN equation, is adopted by researchers to model a three-dimensional (3D) fluid medium termed as fluid sheet to account for the compressive fluid behaviour (Ertekin et al. 2014, Hayatdavoodi and Ertekin 2015, Hayatdavoodi et al. 2019). It is identified by many researchers that waves in shallow water or coastal areas have high amplitudes and therefore a simple harmonic motion alone cannot be used to define the wave particle motion accurately. The shallow water waves are observed to have isolated crests with flatter troughs consequently generating cnoidal wave forms (Seiffert et al. 2015).

Table 2-1 List of available literature based on different field of wave load studies (excluding studies on wave loads on coastal structures).

Based on Offshore Structures	Linear Wave Theory	Non-linear Wave Theory	Hydrostatic Forces Only	Slamming Forces Only	Both Hydrodynamic and Slamming Force Components
Kaplan (1992 & 1995)	Kafali (2008)	Baarholm and Faltinsen (2004)	Morison et al. (1950)	Navaratnam et al. (2013)	Sheppard and Marin (2009)
Isaacson and Prasad (1993)	Ataei et al. (2010)	Ertekin et al. (2014)	Baarholm and Faltinsen (2004)	Moideen et al. (2019)	Ataei et al. (2010)
Bea et al. (1999)	Gullett et al. (2012)	Hayatdavoodi and Ertekin (2014 & 2015)	Douglas et al. (2006)	Hong et al. (2021)	Ataei (2013)
Baarholm and Faltinsen (2004)	Ataei (2013)	Ataei and Padgett (2015)	Mo et al. (2007)		Ataei and Padgett (2013)
Mo et al. (2007)	Ataei and Padgett (2013)	Azadbakht et al. (2015)	Kafali (2008)		Kameshwar and Padgett (2014)
Balomenos and Padgett (2018)	Kameshwar and Padgett (2014)	Seiffert et al. (2015)	McPherson (2008)		Balomenos and Padgett (2018)
Ti et al. (2019)	Gullett et al. (2020)	Cai et al. (2018)	Jin and Meng (2011)		Rahman and Billah (2021)
Wang et al. (2019)	Zhang et al. (2020)	Winter et al. (2018)	Bonakdar et al. (2015)		
Xiong et al. (2020)	Rahman and Billah (2021)	Hayatdavoodi et al. (2019)	Azadbakht and Yim (2015)		
		Nasouri et al. (2019)	Zhu et al. (2018)		
		Ti et al. (2019)	Carey et al. (2019)		
		Wang et al. (2019)	Nasouri et al. (2019)		
			Ti et al. (2019)		

Table 2-2 Effect on wave forces due to wave parameters.

Wave parameters	Wave force components				
	Buoyant	Uplift	Slamming	Drag	Inertia
Wave period	No significant effect observed.	<ul style="list-style-type: none"> Increased with increase in wave period (McPherson 2008, Jin and Meng 2011). In case of long wave period, the effect due to water depth on the uplift decreased (Jin and Meng 2011). Effect of wave current on the uplift force applied to piers decreased with increase in wave period (Wang et al. 2019). 	No significant effect observed.	<ul style="list-style-type: none"> Smaller wave period caused higher drag force (Guo et al. 2015). Drag force found to be directly proportional to the ratio of wave height to still water depth (Azadbakht and Yim 2016). 	<ul style="list-style-type: none"> At wave heights greater than 1.5m, the inertia force increased with increase in wave period (Gullett et al. 2012).
Wave height	<ul style="list-style-type: none"> Remarkable increase in buoyancy force when wave crest passed below the deck (Azadbakht and Yim 2016). 	<ul style="list-style-type: none"> Uplift force directly proportional to the wave height (Azadbakht and Yim 2016). Effect of wave current on the uplift force applied to piers decreased with increase in wave height (Wang et al. 2019). 	<ul style="list-style-type: none"> The slamming component increased nonlinearly with increase in wave height at zero submergence coefficient. On the contrary, it decreased as the coefficient increased (Zhang et al. 2020). Increasing wave height increased slamming forces when the deck was not submerged (Guo et al. 2015). 	No significant effect observed.	<ul style="list-style-type: none"> Wave height smaller than 1.5m had negligible effect on inertia component when wave period was varied (Gullett et al. 2012).
Clearance	<ul style="list-style-type: none"> Lower clearance caused high buoyancy to be induced on the deck (Henry 2011). 	<ul style="list-style-type: none"> Flat plate and girder bridge model studied showed similar uplift force at zero clearance (McPherson 2008). Uplift increased with increase in clearance height (Huang and Xiao 2009). Study based on inundation coefficients of -0.8, -0.76 and -0.74 showed high uplift forces (Marin and Sheppard 2009). Uplift observed to be inversely proportional to clearance height (Guo et al. 2015). Uplift on deck initially increased, then decreased as clearance height increased (McPherson 2008). 	<ul style="list-style-type: none"> At high negative clearances, a downward slamming force was applied to the deck (Azadbakht and Yim 2015). Highest slamming force applied at negligible clearance heights (Guo et al. 2015). 	No significant effect observed.	No significant effect observed.
Wave length	No significant effect observed.	No significant effect observed.	No significant effect observed.	<ul style="list-style-type: none"> Drag force increased with wave length initially, then decreased upon further increase in wave length (Jin and Meng 2011). 	No significant effect observed.

Table 2-3 Effect on wave forces due to bridge components

Bridge components	Wave force components		
	Uplift	Slamming	Drag
Girders/deck	<ul style="list-style-type: none"> • Increase in uplift reported due to increase in height of girders (Marin and Sheppard 2009). • Larger space in between girders caused smaller uplift force to be applied (Sheppard and Marin 2009). • Deck observed as the most important parameter that contributed most to the uplift forces and can apply force up to 7 times the weight of the bridge (Winter et al. 2018). 	<ul style="list-style-type: none"> • Decreased when number of girders decreased (Sheppard and Marin 2009, Moideen et al. 2019). • Number of spikes in the slamming force time history depend on the number of girders (Marin and Sheppard 2009, Sheppard and Marin 2009, Ataei et al. 2010). • Increased up to three times compared to bridge without girders due to increase in surface area (Henry 2011). • Increasing the depth of girders decreased slamming force applied to the deck (Moideen et al. 2019). 	<ul style="list-style-type: none"> • When a seaward girder failed the drag force reduced by 15% (Azadbakht and Yim 2015).
Railing	<ul style="list-style-type: none"> • Increasing railing height increased uplift forces (Xu et al. 2017). 	<ul style="list-style-type: none"> • Presence of railing caused no change in slamming force (Henry 2011). • Providing railing reduced the air gaps between girders thereby reduced the vertical slamming force on the deck (Moideen et al. 2019). 	<ul style="list-style-type: none"> • More notable increase in drag force than uplift due to increased railing height (Xu et al. 2017). • Less noticeable increase in drag force due to railing as compared to the presence of girders (Henry 2011).
Piers	<ul style="list-style-type: none"> • For the same wave-current, the uplift component increased with increase in diameter of piers (Wang et al. 2019). 	No significant effect observed.	<ul style="list-style-type: none"> • Drag force were not proportional to the length of piers (Montoya et al. 2019).

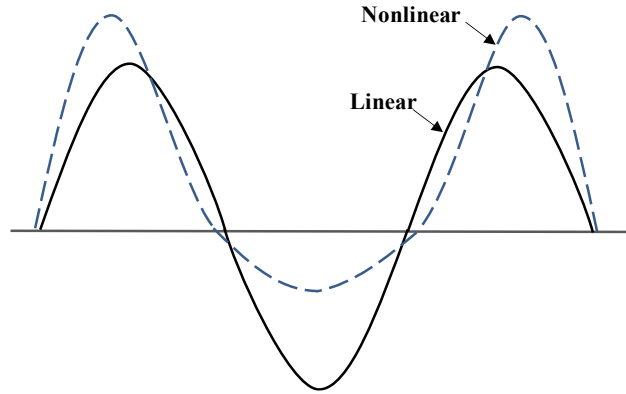


Figure 2-3 Linear and non-linear waves [adapted from (Aguíñiga et al. 2008)]

2.4 Wave load on superstructures

The design of coastal bridges requires quantification of the forces and risks involved. The intensities of waves depend not only on the wave parameter itself but on the structural geometry as well. Sheppard and Marin (2009) reported that the buoyancy forces on the superstructure increased with increase in height of girders. The authors also reported that the spikes in the total wave force time history varied with the number of girders. The high frequency impact (slamming) force was noted to affect the bridge for a duration of $5/8^{\text{th}}$ of the wave period. The experimental observations by Sheppard and Marin (2009) are widely accepted and reproduced by many researchers including the development of wave load calculation guidelines by AASHTO (2008). Winter et al. (2018) reported that the buoyancy force is mostly contributed by the deck where the force can be as high as up to 7 times the weight of the bridge. It was also observed that the vertical impulse force due to waves increased due to increase in girder spacing. Moideen et al. (2019) identified that the slamming force due to wave actions decreased when the number of girders decreased. A decrease in the force was also observed when the height of girders was reduced. Most prominent studies of wave loads on coastal and offshore bridges are focused on wave-induced loads on superstructures. Such is the study by Ataei et al. (2010) where bridge decks were analyzed during hurricane-induced extreme wave loads. The maximum quasi-static wave force magnitude was calculated following the AASHTO (2008) guideline. A sinusoidal profile was generated with amplitude equal to the maximum quasi-static force and time period equal to the wave period as it was observed that the wave forces are in phase with the waves (Kaplan et al. 1995). Following the observations by Sheppard and Marin (2009), Ataei et al. (2010) considered the impact force as a sinusoid with the maximum force calculated from AASHTO and a time period equal to $5/8^{\text{th}}$ of

the wave period. The impact force time history was then superimposed with the quasi-static force to compute the total wave force time history to be applied on the bridge deck.

2.4.1 Previous Experimental Studies

Douglas et al. (2006): The estimation of wave forces on coastal bridge decks is first studied empirically by Douglas et al. (2006) after Hurricane Ivan and Hurricane Katrina took place. The authors provided expressions for uplift (F_v) and drag force (F_h) components as shown in Equations 2-1 and 2-2 respectively.

$$F_v = c_{v-\nu a} F_v^* \quad (2-1)$$

$$F_h = [1 + c_r(N-1)] c_{h-\nu a} F_h^* \quad (2-2)$$

The static wave forces were calculated from these expressions where F_v^* and F_h^* are reference vertical and horizontal forces, $c_{v-\nu a}$ denotes the empirical coefficient of vertical force, c_r is the reduction coefficient due to horizontal force on internal girders and N denotes the number of girders. The authors assumed a linear relationship between the hydrostatic pressure and forces at the deck front.

Sheppard and Marin (2009): The studies by Kaplan (1992) and Kaplan et al. (1995) is extended in this paper by including wave tank experiments to formulate a theoretical model to predict the wave loading on coastal bridge superstructures. Physical models of different types of superstructures, namely, flat slab, girder slab, girder slab with overhangs, girder slab with overhangs and railings were developed to analyze the response of each when subjected to different wave load conditions. The physical tests included variation in water surface elevation, clearance height, wave period and wave heights as well as the number of girders. The vertical and horizontal responses were measured through pressure transducers and load cells at the deck bottom. Separate models were used for the high frequency slamming force determination. A low-pass Butterworth filter was used to separate the high frequency and low frequency (quasi-static) forces. The results show that the slamming force had a period that approximated to $5/8^{\text{th}}$ of that of the wave. Drag and inertia force coefficients were determined empirically and a theoretical model was then developed and validated using the post Hurricane Ivan (2004) damage data of the of I-10 Escambia Bay Bridge (Douglass et al. 2004). Noteworthy to mention is that the added mass expression included in the quasi-static term improved the theoretical model significantly. The authors also proposed a formula for the slamming force by waves on the flat slab. The results of their work has been

implemented by AASHTO (2008) to formulate the expressions for determining the wave-induced loads on coastal bridges.

McPherson (2008): The study by Douglas et al. (2006) is extended here in order to add the effect of overtopping water to the uplift force as this phenomenon causes an additional downward force on the deck. The total uplift ($F_{v,total}$) and drag ($F_{h,total}$) forces were calculated by Equations 2-3 and 2-4. The vertical force is the summation of hydrostatic, buoyancy and air entrapment forces whereas the horizontal component includes hydrostatic force on back and front sides of the deck only. Although identified as part of wave load, the air entrapment force has been neglected in their investigation.

$$F_{v,total}=[(\gamma\delta A_z-F_w)]+[\gamma Vol_B]+[(n-1)0.5\gamma\delta A_z]+0.5\rho C_l A_z v^2 \quad (2-3)$$

$$F_{h,total}=0.5[(\eta_{max}+h-h_G)]+[(\eta_{max}+h-h_D)A_x\gamma]+[0.5(h-h_G)^2 L_B\gamma]+0.5\rho C_D A_x v^2 \quad (2-4)$$

The uplift force from Equation 2-3 is dependent upon the vertical and horizontal projected area of the deck (A_z and A_x), the distance between deck bottom and crest of the wave (δ), volume of water displaced by the bridge section (Vol_B), unit weight of water (γ), η_{max} as the wave crest elevation above still water depth (h), h_G and h_D as the difference in height from girder and deck respectively. F_w represents the downward force created by the overtopping water and n represents the number of girders.

Henry (2011): This paper also conducted an experimental study to determine the wave forces acting on bridge decks due to storm surge. A Moog shake table was used to generate waves in the water tank by shaking the table at a frequency (ω_s) calculated using the formula given in Equation 2-5. The variables in the equation include: L as the length of water tank, gravitational constant (g) and h as the depth water in the tank. Two types of decks namely flat slab and girder decks, were studied with different clearance heights and the resulting vertical, horizontal and overturning moments analyzed. The author identified that the lateral component consisted of slamming, inertia and drag forces whereas the vertical wave load component included impact pressure due to variability of air entrapment, positive and negative slowly varying pressures.

$$\omega_s = \sqrt{\frac{g\pi}{L} \tanh\left(\frac{h\pi}{L}\right)} \quad (2-5)$$

Guo et al. (2015): The authors conducted experimental analysis to determine the hydrodynamic forces acting on the coastal bridge superstructure due to hurricanes. Both vertical and horizontal components of the quasi-static and slamming forces were extracted from underwater load cells

installed to the bridge model. Due to modeling of the full bridge, including substructure and other adjacent bridge components, the authors have identified their study as a unique one. The parameters used in the investigation are wave period, wave height, clearance height with partial and full submergence cases. The results signify that the maximum vertical slamming force occurred at zero clearance height and that the horizontal slamming force could be neglected. The drag force, however, was observed to be inversely proportional to the wave height. The authors also compared their experimental results to those obtained from the theoretical formulas by Douglas et al (2006) and AASHTO (2008) and found that the theories overestimated the wave-induced forces remarkably.

Huang et al. (2019): This study is based on the effect of solitary wave forces on coastal bridge box-girder superstructure using experimental analysis. A piston-type wave maker is used to generate the solitary waves. The wave maker used to generate the extreme solitary waves was programmed following the method by Goring (1978). Variables in their study includes wave height, water depth and submergence coefficients. The results obtained were further analyzed to study the vulnerability of coastal bridge decks towards solitary waves.

2.4.2 Previous Numerical Studies

Barholm and Faltinsen (2004): The study by Bea et al. (1999) was extended by Baarholm and Faltinsen (2004) where the offshore platform decks subjected to extreme wave loads were studied using three theoretical methods and an experimental analysis. The wave loads were theoretically modeled assuming the fluid to be incompressible and irrotational. The two-dimensional fluid flow was explained by Laplace's equation, and the theoretical methods involve the Wagner-based method and Green's second identity. It is noteworthy to mention that only the quasi-static force was analyzed by the authors and good agreement was found between the experimental and theoretically calculated results for the deep water conditions as studied.

Huang and Xiao (2009): Wave force simulation using the RANS equation and RNG $k-\epsilon$ model in ANSYS similar to Zhang et al. (2020) was also done previously by Huang and Xiao (2009). The effect of Hurricane Ivan (2004) on the deck of I-10 Escambia Bay bridge in the coasts of Florida was modeled in this paper. The authors stated that, since the vertical uplift exceeded the weight of the simply supported deck, the vertical lift was considered as the major concern for damage of superstructures. Their numerical results were compared with those obtained from empirical relations by Douglas et al. (2006) and Bea et al. (1999).

Jin and Meng (2011): The authors here provided a method for computation of wave loads on the superstructure of coastal highway bridges. In their numerical study done in *Flow-3D* software, the authors provided simplified equations for calculating the uplift (F_{v0}) and drag (F_{h0}) forces on coastal bridge decks assuming that drag force increases linearly with depth of inundation and that the pressure decreases linearly along the height between wave crest and storm water elevation. The expressions adopted by the authors for calculating wave loads are shown in Equations 2-6 and 2-7 where F_b accounts for buoyant force, $C_v(T)$ and $C_h(T)$ are coefficients to include the effect of wave period (T) in vertical and horizontal directions, respectively. The length, width and depth of the bridge deck are denoted by L_x , L_y and L_z , respectively.

$$F_{v0} = F_b + 2\rho g \eta_{max} L_x L_y C_v(T) \quad (2-6)$$

$$F_{h0} = 2\rho g \eta_{max} L_y L_z C_h(T) \quad (2-7)$$

SERRI Report (Gullett et al. 2012): This is a report on coastal highway bridge decks subjected to storm surge and wave loadings due to hurricanes which used the linear wave theory to model the wave particle kinematics. A wave load model including vertical and horizontal load components was developed in *Fortran*. The vertical force components included drag, inertia, slamming and buoyant forces whereas the drag, inertia and slamming forces only make up the horizontal components. The expressions used for calculating these loads were adopted in modified form from (Bea et al. 1999) and (Sheppard and Marin 2009) as shown in Table A of Appendix A. A numerical model of the bridge superstructure was developed in the FE software *ABAQUS* where the time variant wave load model was applied to the bridge model in an element by element basis using *Fortran*. The model was verified using the experimental study by Bradner et al (2009). The drag and inertia coefficients in each direction were determined by choosing a value that matched the reaction force from the simulated bridge model to that of the data as obtained from experiments (Bradner et al. 2009). The slamming load coefficient was taken from the study by Isaacson and Prasad (1993). However, a buoyancy coefficient was included in the expression to account for an additional vertical lift experienced as a result of entrapped air in the bridge deck.

Ataei et al. (2010) and Ataei and Padgett (2013): Wave loadings due to hurricane-generated storm surge on coastal bridge decks were computed using the equations given by AASHTO (2008). The authors here modeled the time history of the wave loads by taking a sinusoidal profile of the quasi-static loads that was assumed to have a period equal to that of the wave and amplitude equal to the maximum quasi-static load as calculated from the AASHTO equations. The slamming force

was also modeled as a sinusoid using the same approach by taking its time period to be $5/8^{\text{th}}$ of that of the wave period according to the observations by Sheppard and Marin (2009). The quasi-static and slamming force time histories were then superimposed to obtain the total wave-induced load on the bridge deck, a schematic representation is given in Figure 2-4. The moment induced due to sudden changes in force when wave passes over the deck was also calculated. The bridge was modeled and applied with the calculated loads and moments in *OpenSees* (McKenna et al. 2013).

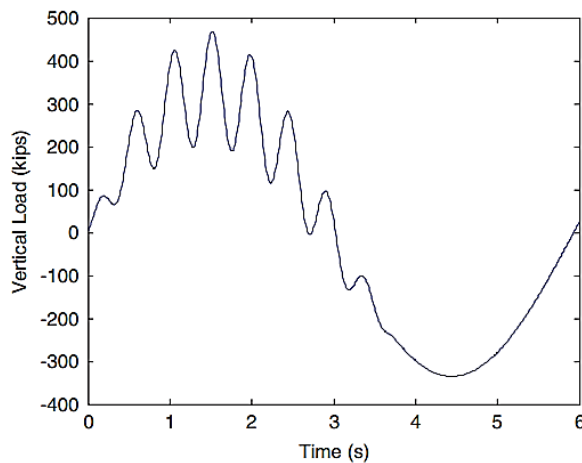


Figure 2-4 Schematic representation of total vertical wave load as reported by Ataei et al. (2010).

Kameshwar and Padgett (2014): This study also used AASHTO equations to calculate the maximum vertical and horizontal forces by waves and modeled the load-time histories as sinusoids. The time period in their study, however, were modeled as uniform variable which was then used to determine the wave length thereby randomizing both time period and wave length inputs. The moment-time history was determined using the vertical force applied to the bridge deck. Their study assumed that the wave load was distributed uniformly throughout the length of the deck.

Hayatdavoodi and Ertekin (2014): The authors here studied vertical and horizontal loads generated by waves due to storm surge on four coastal bridge decks numerically using *OpenFOAM* and theoretically using Level 1 GN equations and long-wave approximation (LWA) techniques. The bridge deck and wave tank were simulated using an unstructured mesh in *OpenFOAM*. The comparison of horizontal and vertical forces as obtained from the three types of modeling are represented in Figure 2-5. It was observed that the total vertical reactions were greater than those of the horizontal reactions on the deck for all the scenarios studied. The results obtained from the

models developed were then compared with those obtained from AASHTO (2008), Douglas et al (2006) and McPherson (2008) formulas. It was noted that when the water level did not overtop the deck, the deck slab (with no girders) horizontal reactions were underestimated by all three empirical formulas. However, the girder deck horizontal forces obtained from AASHTO equations showed best compliance with those obtained from *OpenFOAM* results. Interestingly, the vertical force on slab with no girders obtained from the empirical formulas were higher than those found *OpenFOAM* analysis results. The authors finally reported that the GN equations were less computationally difficult. Moreover, since it provided comparable results to that from *OpenFOAM*, the GN equations could be a viable option for calculating loads on submerged bridge decks.

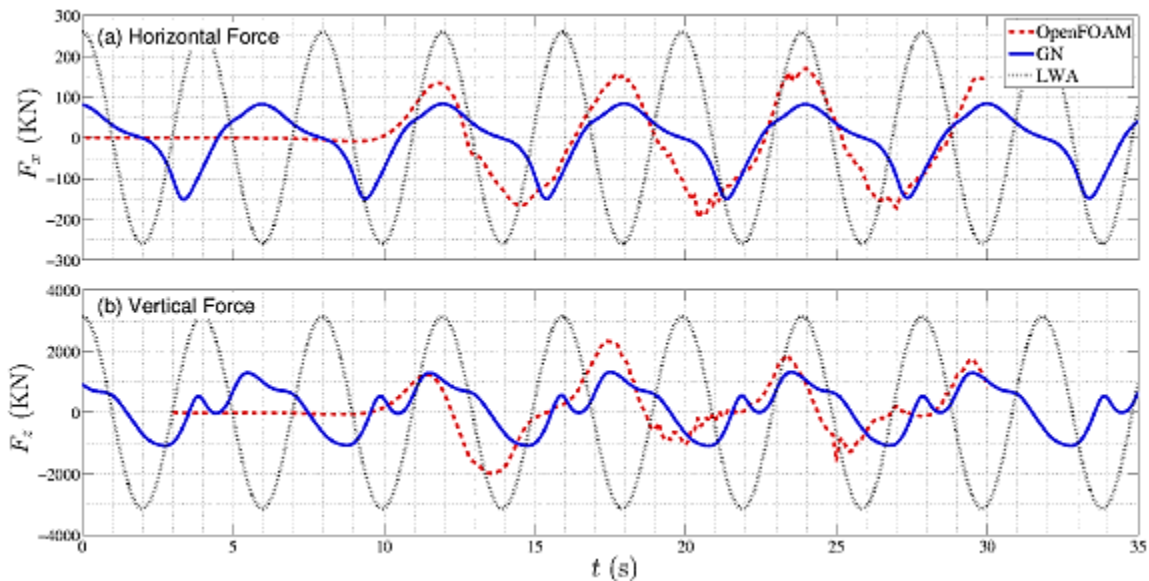


Figure 2-5 Comparison of horizontal and vertical wave loads on decks as reported by Hayatdavoodi and Ertekin (2014)

Ataei and Padgett (2015): This study incorporated FSI of coastal bridge deck under hurricane-induced wave loads. The model was developed in *ADINA* where the variables considered for boundary condition were kinetic energy, rate of energy dissipation and average flow velocity. The deck and column reaction due to the applied hydrodynamic loads, displacements in both directions and lateral drift of columns were recorded throughout the study.

Azadbakht and Yim (2015): This paper investigated the tsunami wave load on coastal girder bridge decks by dividing their study into two stages, one signifying the event when tsunami water surface elevation reached the bottom chord of the deck and then overtopping the deck. The other

stage represented a situation when full inundation of the entire bridge occurred. The vertical, horizontal and overturning moment acting on the bridge superstructure were calculated using finite element (FE) analysis in *LS-DYNA* where the numerical code was developed to solve the Navier-Stokes equation. The pressure distribution obtained from the software analysis were integrated to determine the forces acting on the deck. A total of five different tsunami conditions were applied in their study and the model was validated with experimental results. The force coefficients were determined empirically. The authors have proposed formulas for calculating the maximum horizontal and vertical loads as shown in Equations 2-8 to 2-10. Their study assumed that the tsunami free surface remained uniform across the deck width implying that the total bridge was inundated when tsunami flow reached a certain height in the seaward side of the bridge.

$$F_{H\ max} = 0.5\rho g(2h_0 - L_h)L_h + 0.5C_d\rho v^2 L_h \quad (2-8)$$

$$F_{DV\ max} = C_{DV}[\rho g(h_0 - L_g - T_d)L_v + 0.5C_{vs}\rho v^2 L_{sb}] \quad (2-9)$$

$$F_{UP\ max} = C_{UP}\rho gV + 0.5C_l\rho v^2 L_v \quad (2-10)$$

The terms used in Equations 2-8 to 2-10 are: $F_{H\ max}$, $F_{DV\ max}$ and $F_{UP\ max}$ denoting maximum horizontal force, maximum downward vertical force and maximum vertical uplift force, respectively. On the other hand, C_d , C_{DV} , C_{UP} , C_l and C_{vs} represent the coefficients for drag, empirical downward vertical force, uplift force, lift and slamming forces, respectively. V denotes the volume of bridge, ρ as the density of the water. L_g denotes the height of girder whereas L_h and L_v represent the height and width of the deck. L_{sb} is the effective length for the vertical slamming force acting on bridge deck.

Cai et al. (2018): This study used dynamic-mesh updating method in *ANSYS* to develop the numerical model of the coastal bridge superstructure under the action of solitary waves due to hurricane by simulating the fluid domain in *FLUENT*.

Winter et al. (2018): To analyze the force demands posed by different components in a coastal bridge deck subjected to tsunami like wave loadings, this study incorporated Open Source Field Operation and Manipulation (*OpenFOAM*) to numerically simulate the bridge deck and the FSI. A dam-break approach was selected to model the wave impact on deck and the program solved Navier-Stokes continuity and momentum equations. The field variables chosen to define the boundary condition of the FSI were volume fraction, dynamic pressure, components of velocity and turbulent kinetic energy and the dissipation rate of kinetic energy. Variables considered for parametric study of the deck were the number of girders and superelevation angle. The demands

by girders, deck and traffic barriers were analyzed from the vertical and horizontal reactions obtained. Upon comparing with the experimental results by Nakao et al. (2013), their model was validated.

Carey et al. (2019): This paper studied the multihazard risk assessment of coastal soil-foundation bridge system subjected to tsunami wave loadings using numerical analysis in *OpenSees* (McKenna et al. 2013). A constant drag force, as shown in Equation 2-11, was applied to the bridge at different heights to cover the events ranging from partial to full inundation. A drag coefficient, (C_D) of 2.0 and the projected area of the entire deck width (B) were considered to determine the wave induced horizontal load with flow velocity (v) to be constant over time. For a constant flow height, the drag force was calculated and applied to the model for pushover analysis while incrementing the flow velocity until the drift limit state was reached. The process was repeated for another flow height and the results analyzed.

$$F_D = 0.5 C_D \rho B (h v^2) \quad (2-11)$$

Hayatdavoodi et al. (2019): The study Hayatdavoodi and Ertekin (2014) was extended to include parametric study on bridge decks submerged in shallow water subjected to hurricane-induced nonlinear wave loads. Cnoidal and solitary wave loads applied on the FE model of the submerged deck was programmed using the Level 1 GN equations. The results were then compared with those obtained from computational fluid dynamic (CFD) and experimental analysis and a satisfactory agreement was achieved. Wave height, wave period, deck length and deck submergence height are the variables considered in the study. When compared among the solitary waves, it is observed that, both vertical and horizontal forces applied on the deck increased linearly with increase in deck length. However, the vertical force increased up to a constant with increasing submergence depths. Among the cnoidal wave comparison results, the vertical force increased linearly with increase in wave height and this effect is even more prominent when the submergence depth is small. On the other hand, the vertical wave force decreased nonlinearly with increase in submergence for the cnoidal wave models studied.

Montoya et al. (2019): Another numerical study on vulnerability of coastal highway bridge under extreme hurricane loads which used the Coupled Eulerian-Lagrangian (CEL) technique available in *ABAQUS* to capture the response of two major highway bridges damaged by Hurricane Katrina (2005). The authors modeled the velocity profile of the periodic waves using Stokes's second order theory. The results were then compared with those obtained from Douglas et al. (2006) and

AASHTO (2008) equations. It was observed that although the average shear and uplift forces were within the range as obtained from AASHTO equations, the peak value from simulation exceeded that of the AASHTO estimations. The authors lastly recommended future studies to understand this pulse type impact force on bridges.

Moideen et al. (2019): The solution of incompressible fluid using Navier-Stokes in an open source software named *REEF3D* was implemented in their paper to carry out a parametric study of coastal bridge decks subjected to tsunami and storm surge. Only vertical wave loads were considered and the parameters considered were number of girders, depth of girder and wave height. It was observed that, as the ratio of wave height to water depth increased, the maximum vertical wave impact force increased. However, the impact force was found to decrease when air gap between the girders increased. Interestingly, the authors observed that there was a negligible effect of girder depth on vertical impact loads. Also, providing railing and overhangs reduced the air-entrapment and thereby decreased the impact force on decks.

Gullett et al. (2020): The results from the SERRI report were then utilized in this study where wave force calculation on bridge decks during hurricane storm surge is done using a software named as *AMBUSH*. This software incorporates four modules: FE modeling in *ABAQUS*, wave load calculation in wave load software (*WLS*) and the compilation of the bridge model to the wave load using the Element Data Transfer (*EDT*). The results from *AMBUSH* were compared to AASHTO Guide specifications (2008). It is reported that although there is a good correlation with AASHTO, the *AMBUSH* required further improvements for the cases when wave strikes in an angle. It is also reported that further refinement of the software is needed in order to examine the internal stresses of the members for vulnerability analysis.

Zhang et al. (2020): Coastal box girder bridge deck subjected to hurricane storm surge and wave are studied by Zhang et al. (2020) both experimentally and numerically. Their experimental analysis included wave flume tests with varying current velocities, wave height, wave period and submersion coefficient (ratio of the height difference from girder bottom to the surge water level to the height of the girder). The wave-current force induced on the deck were numerically investigated using the RANS equation and RNG $k-\varepsilon$ model available in *FLUENT*. From both the tests, a low frequency (quasi-static) and a high frequency (slamming) force was recorded. The numerical results were compared with those from the experiments and only 8% variation between the results were observed which implied the numerical model's high accuracy.

2.5 Wave load on substructures

Studies regarding impacts of extreme wave loads on substructure components are scarce as most literature focus on the superstructure components of bridges. However, a few studies have been done that gave the basic idea of the behaviour and possible failure mechanism of piers and piles of bridges. The geometrical parameters and surrounding site conditions of these members are also seen to affect the wave-induced loads significantly. For instance, the effect of varying pier lengths on the force demand due to the action of hurricane induced wave loads is reported in Montoya et al. (2019). The numerical results revealed that increase in pier lengths did not impart any increase in vertical uplift or shear forces. The following sub-sections briefly present the methods adopted to formulate the wave loads on the piers and piles.

2.5.1 Piers

Kafali (2008): This study used linear wave theory model to determine the wave particle kinematics and then applied zero-mean stationary Gaussian process by Pierson-Moskowitz spectrum to define a spectral density function to derive the wave velocity. The author then used the Morison formula (1950) to find out the horizontal force due to waves acting on columns. In the paper, wind loads were considered to act at the deck whereas the wave loads were assumed to act at the submerged part of the bridge column (the submerged length of the column equals the water depth).

Wang et al. (2019): The authors here studied the response of circular bridge piers subjected to simultaneous earthquake and wave-current actions. The total force was decomposed into diffraction hydrodynamic pressure, incident hydrodynamic pressure along with the pressure associated with earthquake. The wave-current interaction was modeled using diffraction theory and the equations for determining the total force used in the study is presented in Table A.

Hong et al. (2021): This experimental study presents the effect of breaking wave loads on sea-crossing bridge piers. The breaking waves were generated using focused wave theory where three different wave heights were used as variable conditions. Three different cross-sections of the piers were also studied. It is observed that the breaking wave load on the square pier is higher than that on circular pier although they both had the same projected surface dimensions. It is also reported that as the diameter of the circular pier increased, the breaking wave load acting on it also increased.

Rahman and Billah (2021): This study incorporated three different pier geometries and identified the variations in wave loads being applied. The total horizontal wave force was calculated based

on the linear wave theory comprising the drag, inertia and slamming forces. It is concluded that, similar to the observation by Hong et al. (2021), the square section piers were subjected to wave loads of higher magnitude than the circular piers having identical projected surface. The study also compared the oblong section piers with the same projected dimension as the circular and square section piers and reported that the highest wave load was applied on the oblong piers. The comparison shown by the authors is presented in Figure 2-6.

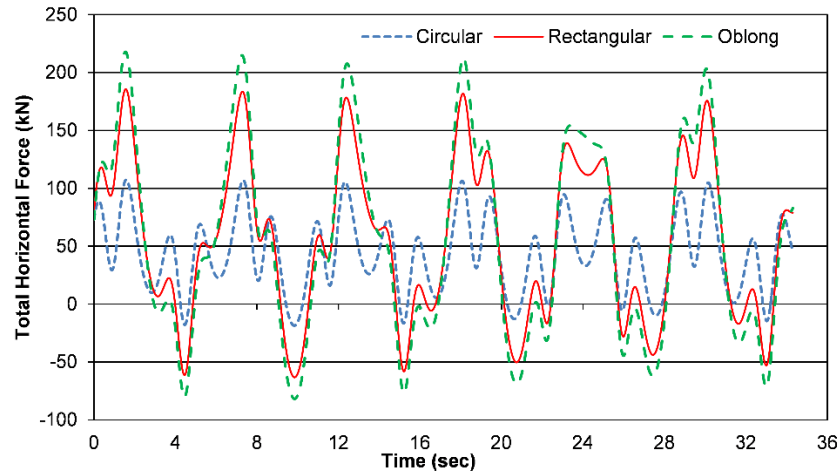


Figure 2-6 Variation of total horizontal wave force time history due to difference in pier cross-sections by Rahman and Billah (2021)

2.5.2 Piles

Morison et al. (1950): The earliest model proposed for wave load calculation on piles was by Morison et al. (1950). The authors provided expression for the horizontal load consisting of drag and inertia terms with empirically determined coefficients. The equation proposed, as shown in Table A, is widely used by researchers for its high applicability.

Bonakdar et al. (2015): In this study formulas for predicting the wave loads on a slender pile among a group of piles is developed using artificial intelligence and machine learning technique. The hybrid M5 tree-genetic programming (M5MT-GP) model developed was able to provide a total of 12 formulas to assess the pile group effect based on the flow regime, relative spacing between piles and orientation of the group piles. According to the authors, the formulas were only valid for non-breaking waves with a particular set of structural and hydrodynamic conditions.

Balomenos and Padgett (2018): The vulnerability of wharf/pier structures in port facilities due to hurricane-induced storm surge and wave forces is studied in this paper. Equations provided by

McConnell et al. (2004) is used to calculate the wave forces on the horizontal members. On the other hand, the wave force on vertical members were calculated from the expressions by FEMA (2013). This numerical study is done in OpenSees where the piers were exposed to both breaking wave and hydrodynamic loads.

Zhu et al. (2018): This paper investigated coastal bridges applied with combined action of wave, wind and vehicular loads. The authors applied the irregular wave theory to model the time histories of wave particle velocity and acceleration. Morrison equation (Morison et al. 1950) is applied to calculate the wave force which included drag and inertia forces only. The coefficients used in calculation of drag and inertia forces were taken from the specifications of AASHTO (2008). The effect of group pile was noted, where the wave load is assumed to act only on the pile groups owing to the fact that the water level did not reach the high elevation of the long span slender coastal bridge studied.

Nasouri et al. (2019): This study presents the numerical analysis of hydrodynamic response of coastal bridges where both girder superstructure and pier substructure components were modeled. The FE model of the bridge was done in *ABAQUS* and the wave load was applied to the structure using the CEL technique. It is reported that the shear and uplift forces increased with increase in velocity. It is also noted that the shear forces are significantly affected due to changes in the angle of impact of the waves.

Ti et al. (2019): This paper investigated the stochastic response of a long span cable stayed sea-crossing bridge under the action of wave loads numerically. Both linear and nonlinear forces due to the stochastic waves were modeled in the hydrodynamic solver *AQWA* and was then fed to the bridge model developed in *ANSYS*. Single summation method was used to generate stochastic waves in the model and the diffraction theory was used to solve both the first order linear and nonlinear wave loads. The nonlinear wave load was defined as the summation of the first order and second order wave loads. The wave force and moment time history obtained from *AQWA* were applied at the centroid of the bridge cap as point loads in the model in *ANSYS* and thereafter the responses analyzed. A comparison of the wave force in horizontal direction obtained by the methods from their study is presented in Figure 2-7. It is observed that the nonlinear wave forces remarkably increased the dynamic response of the pile foundation.

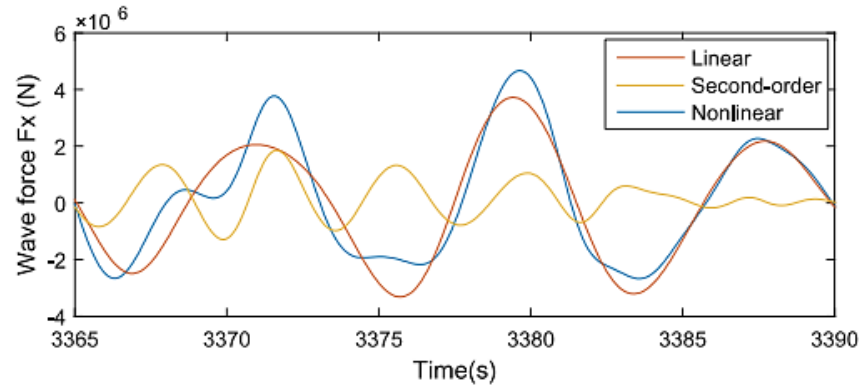


Figure 2-7 Comparison of horizontal wave load time history on bridge piles as reported by Ti et al. (2019).

Table 2-4 Comparison of studies with published empirical equations

Reference	Empirical formulas			
	AASHTO (2008)	Douglas et al. (2006)	Bea et al. (1999)	Morison et al. (1950)
Huang and Xiao (2009)	--	<ul style="list-style-type: none"> • Uplift force calculated using this formula was 6.3% lower than that from numerical analysis. • The horizontal force was overestimated by 39.4% compared to numerical results. 	<ul style="list-style-type: none"> • Uplift force obtained from numerical analysis was 21.1% higher than that obtained using this method. • Horizontal force was overestimated by 86.8% compared to numerical results. 	--
McPherson (2008)	--	<ul style="list-style-type: none"> • Overestimated the measured vertical force applied on the deck. 	<ul style="list-style-type: none"> • Underestimated the measured total vertical force on the deck. 	--
Hayatdavi and Ertekin (2014)	<ul style="list-style-type: none"> • Most accurate estimations obtained for girder bridge decks. 	<ul style="list-style-type: none"> • Overestimated the vertical wave force on bridge decks compared to that calculated by OpenFOAM. • Underestimated the horizontal wave force on decks compared to the OpenFOAM results. 	--	--
Ataei and Padgett (2015)	--	--	--	<ul style="list-style-type: none"> • Overall wave force calculated by this method under predicted those obtained from the FSI.
Guo et al. (2015)	<ul style="list-style-type: none"> • Underestimated the vertical force compared to that numerically obtained when wave heights were small. • Overestimated vertical forces for larger wave heights. • Over predicted the wave force for fully submerged deck under water. • Provided a good estimation for the vertical slamming load on the deck. 	<ul style="list-style-type: none"> • The maximum vertical force at deck for subaerial and zero clearance stages were found within maximum and minimum force as calculated by this method. • When clearance set to zero, the horizontal force estimated by this formula was significantly larger than that numerically obtained. 	--	--
Montoya et al. (2019)	<ul style="list-style-type: none"> • Estimations of uplift and horizontal forces by this method were within the range as those numerically obtained. • Large pulse type force obtained were out of the limits as calculated by this guideline. 	--	<ul style="list-style-type: none"> • Estimations of uplift forces by this method were within the range as that numerically obtained. • Shear force numerically obtained exceeded those predicted by this method. 	--

2.6 Design guidelines

2.6.1 AASHTO (2008) Guide Specifications for Bridges Vulnerable to Coastal Storms

The American Association of State Highway and Transportation Officials (AASHTO) (2008) provided three cases for calculating the maximum load due to waves. The specification is developed based on the study by Sheppard and Marin (2009). The guide takes into consideration the effect of air entrapment at the superstructure, clearance heights, the bridge geometry and wave parameters in the form of specific coefficients. The first case is based on the assumption that the vertical uplift force is the major component whereas the drag force slamming force and overturning moment are only associates. Since the uplift is major component, this case is suitable for design of bridge decks. The second case assumes the drag force as the major component of wave load and consequently slamming, uplift, overturning moments to be the associates. The second case can be used to design substructures to prevent lateral displacements. The third case considers that a prorated distribution of both the drag and uplift forces exist at the overhang seaward portion of the deck. The expressions for the first and second cases are shown in Table A. AASHTO acknowledges that offshore platforms' geometrical and wave characteristics are significantly different than those of coastal bridges. Platforms decks are thin horizontal structures located in deep open waters, while bridge structures have finite thicknesses and are in shallow waters.

2.6.2 ASCE 7-16 Minimum design loads for buildings and other structures

The ASCE 7-16 (2016) specifies guidelines for calculating the design loads on structures by characterizing waves into breaking and nonbreaking waves. According to this guideline, wave loads shall account for the following: waves breaking on any portion of the bridge; uplift forces due to the shoaling waves below; wave runup; wave-induced drag and inertia forces; and wave-induced scour at the base or foundation of the structure. The basic concept of fluid mechanics is used to determine the expression of breaking wave loads on vertical piles or columns as shown in Table A. The drag force is to be applied as a point load at the still water elevation to the pile. An impact force is to be considered when the bridge is likely to have impact from debris, a specific formula is given for its quantification in the design. This code, however, provides a static force with a design flood velocity selected conservatively from the range of values calculated from expressions for maximum and minimum flood velocities.

2.6.3 Canadian Highway Bridge Design Code (CSA S6:19)

According to the Canadian Highway Bridge Design Code (CHBDC) (CSA S6:19), the total water load shall account for the buoyancy, hydrodynamic loads and loads due to wave actions. This code specifies that load be applied in the bridge substructure as: static pressure which is the product of density of water and height of submergence, buoyancy calculated from the volume of water displaced, the stream load calculated as $P = 0.5C_D\rho Au^2$ with C_D as drag coefficient, ρ as density of water, u as the velocity of water at the design flood and A being the projected area of the pier perpendicular to the flow. A lateral load consideration is given in this code by the formula $P_p = 0.5C_L\rho HLu^2$ with C_L as lateral load coefficient dependent upon the angle of incidence of the flow, H is the still water depth, L is the dimension of the pier perpendicular to the flow direction. The code also mentions determining the load due to wave action considering the site conditions. In the event when the site-specific conditions are unknown, the formula $F_w = 10H_w^2$ can be used where H_w denotes the wave height. The force F_w is to act at the mid-height of the wave above the still water elevation. The code provides specific coefficients for the drag force according to the upstream shape of pier and coefficients according to the angle between longitudinal pier axis and flow direction for the lateral load calculation.

2.7 Fragility Assessment Studies

A comprehensive framework is needed to be developed through the observation of the involved risks and failure mechanisms for assessing the vulnerability of bridges in coastal hazardous events. Being the first step of risk and resilience assessment of structures, fragility is the likelihood of exceeding a particular level of damage with respect to a certain intensity measure (IM). Several methods for developing fragility functions of bridges exposed to wave loads are available in literature namely: heuristic, empirical, analytical and remote sensing methods. The analytical method of developing fragility functions has garnered prominence as it can be incorporated into various hazard and damage levels and it is not limited to a specific bridge class or type. Shoji and Moriyama (2007) developed empirical fragility functions considering the inundation depth as the only IM by analyzing statistical data obtained from field surveys of bridges done after the Indian Ocean tsunami (2004). Akiyama et al. (2013) developed a simplified approach to generate the fragility of a concrete girder bridge damaged due to the Tohoku tsunami (2011) considering wave height as the only IM. The authors identified that the probability of damage increased with decreased pier heights. The HAZUS (2013) provided heuristic based method to assess the fragility

of bridges by taking the flow velocity as the IM. Gidaris et al. (2017) reported that the vulnerability increased due to increase in flow velocity. Balomenos et al. (2020) were the first to develop parameterized fragility models for the regional risk assessment of bridges exposed to coastal hazards. Table 2-5 presents a summary of studies based on developing fragility curves of bridges under extreme wave loads.

Ataei and Padgett (2013) developed fragility functions for bridges exposed to hurricane waves considering the unseating failure of the deck. The unseating failure was identified when the capacity exceeded the uplift force by the waves. The wave height and clearance height were taken as the IMs for their study. Kameshwar and Padgett (2014) developed a probabilistic framework to assess the unseating failure of multi-span simply supported concrete girder bridges due to earthquake and hurricane considering wave height and clearance height as IMs regarding the hurricane induced loads. Ataei and Padgett (2015) later on incorporated machine learning to develop surrogate modeling to predict the unseating failure of bridge deck exposed to hurricane-induced wave loads. Qeshta et al. (2021) developed fragility functions of coastal rigid framed bridges subjected to tsunamic-induced hydrodynamic loads. The authors reported that more accurate fragility assessment is done using the two-parameter IM as the force is dependent on both flow velocity and depth.

Huang et al. (2019) experimentally studied the vulnerability of a coastal box girder bridge deck under solitary wave considering wave height, water depth and submergence coefficient as the IMs. The vulnerability was assessed by comparing the bridge deck's capacity with that of the demand posed by the solitary wave. Huang et al. (2022) further analyzed the fragility of box-girder coastal bridges with different connection types under extreme waves using non-linear dynamic analysis. The engineering demand parameters used in their study was the vertical capacity and horizontal deformation of the rubber bearings. The authors used the potential flow theory to generate the wave force time history and identified that when adequate vertical connection was missing, adding lateral blocks did not reduce the probability of damage. The authors also noted that increasing the number of bolted connections reduced the vulnerability of the coastal box-girder superstructure. Zhu et al. (2021) developed fragility surfaces for coastal bridge decks under hurricane waves using numerical models validated by experimental results. The FE modeling was done in ANSYS Fluent where the hydrodynamic load from waves were generated using the solitary wave theory. The

authors developed an overturning failure mode where the component level damage of the bridge could be identified.

Component level fragility functions are mapped to system level fragility to derive the damage probability of the complete bridge system. However, different components experience different level of damage corresponding to a certain IM. Therefore, it is often difficult to assess the vulnerability of the system using the fragility of one component only. There are two ways of obtaining the system fragility by combining the fragilities of the components upon assuming a series or parallel connection among them (Dueñas-Osorio and Padgett 2011). The series connection signifies that each component is important and when damage of a certain level is experienced by one component, the whole bridge system experiences the damage at the same level (Nielson and DesRoches 2007). The parallel connection assumes that a certain damage to the system occurs when all the components experience the same level of damage (Zhang and Huo 2009). Ataei and Padgett (2013) developed limit state capacity for bridge systems exposed to hurricane waves and surge loads. The component level responses, namely abutment displacements, axial strain in columns and pile uplift forces were mapped to global damage states (DS). Kameshwar and Padgett (2014) estimated the system fragility functions basing on the series connection assumption in the multihazard risk assessment of highway bridges exposed to hurricane and earthquake.

2.8 Resiliency Assessment Studies

The resilience estimation of structures under extreme loads has recently become popular (Padgett and DesRoches 2007, Bocchini and Frangopol 2012, Minaie and Moon 2017, Qeshta 2019, Li et al. 2020). As the functionality of the bridge depends upon the damage of its components, namely piers, bearing, shear keys and deck, a probabilistic method of determining the restoration model of bridge under extreme waves is better suited compared to quantification of performance percentage (Qeshta 2019, Qeshta et al. 2021). HAZUS-MH (2011) provided restoration models for structures damaged by tsunami. A method of developing a model for loss of performance of bridges due to tsunami is also provided by HAZUS (FEMA 2013). Godazgar et al. (2022) conducted a preliminary resilience quantification for a Bridge in Quebec, Canada, adopting a framework that utilizes hazard, fragility and restoration assessment. Qeshta (2019) proposed a method of analysing resiliency of coastal bridges under extreme waves by combining the resources (cost) and recovery time. The performance (functionality) quantification was done using the total

travel time and total travel distance data assuming that the residual performance at the instant of the hazard to be 45%. Mohammed and Uddin (2018) studied bridge resiliency during hurricanes where the I-10 Escambia Bay bridge was numerically analyzed under hurricane Katrina using CFD in *StarCCM*. The performance index measured in their study is based on the fraction of the superstructure load carrying capacity to the wave loads being applied on it. Minaie and Moon (2017) developed a simplified qualitative method to quantify bridge resilience via four phases of recovery and restoration. The robustness (residual functionality) was determined combining factors for uncertainties, vulnerability, level of hazard and bridge importance. The recovery time was computed from empirical restoration times and factors to account for the disaster management practices, history of extreme hazard events and bridge type. The authors verified their method of resiliency analysis by comparing their case study with post-event survey data of the I-10 Twin Bridge of Lake Pontchartrain in New Orleans damaged due to hurricane Katrina. Li et al. (2020) also followed the same approach to quantify long term resilience of bridges under multihazard condition including earthquake and extreme wave loads.

2.9 Summary

This chapter presents a detailed summary of the experimental and numerical studies undertaken to study the effects of waves loads on bridge superstructures and substructures to this date. This chapter systematically summarizes the wave load calculation and simulation methods adopted in past studies. Water and wave load estimation methods provided in the design guidelines are discussed. The common methodologies adopted in literature to develop the damage states and thereby the component and system-level fragility functions are also discussed. It is observed that very few research regarding wave load estimation on coastal bridges using the CHBDC (CSA S6:19) guidelines have been done. Moreover, limited research exists regarding strain-based material damage detection technique to develop the component damage states. Further refinement of accurate estimation of the time varying wave forces and the corresponding resiliency assessment technique for the coastal bridges is needed which is highlighted in this chapter. As such, the merits of this thesis are justified in developing performance-based damage states and fragility curves for both the superstructure and substructure components of coastal bridges under extreme wave loading. Finally, an overview of the quantification methods adopted by the researchers for coastal bridge resiliency towards extreme wave loads is presented.

Table 2-5 Summary of bridge fragility analysis under extreme wave loads

References	IM	EDP	Variables	Methodology
Shoji and Moriyama (2007)	Depth of inundation	Ranks termed based on visible damages: A: wash out of the deck B: abutment damage including scouring, erosion of embankment soil and deck displacement. C. Deck attachment damage D. No or negligible damage	--	Empirical method based on damage data and field observations.
Akiyama et al. (2013)	Wave height	Deck uplift, capacity of piers	Concrete compressive strength, steel yield strength, coefficient of friction and model errors.	Method relating the total uplift and drag force to the resistance of the bridge to vertical and horizontal movements.
Ataei and Padgett (2013)	Clearance height and wave height.	Deck uplift and connection strength between superstructure and substructure.	Deck thickness, concrete compressive strength, steel yield strength, density of concrete and connection element strengths.	Using empirical equation by AASHTO (2008).
Ataei and Padgett (2013)	Clearance height and wave height.	Stiffness degradation, lateral and vertical strength degradation.	Concrete compressive strength, steel yield strength, density of concrete and shear strength.	<ul style="list-style-type: none"> • Sinusoidal dynamic analysis in OpenSees. • Maximum force calculated from AASHTO (2008).
Kameshwar and Padgett (2014)	Clearance height and wave height.	Deck unseating	--	Sinusoidal dynamic analysis in OpenSees
Ataei and Padgett (2015)	Clearance height and wave height.	Deck transverse displacement.	Concrete compressive strength, steel yield strength, density of concrete and coefficient of friction.	<ul style="list-style-type: none"> • Using empirical equations by AASHTO (2008) and Douglas et al. (2006). • FSI • Surrogate modeling.
Huang et al. (2019)	Wave height, water depth and submergence coefficient	Deck capacity in vertical and horizontal directions	--	Solitary waves produced via piston type wave maker.
Qeshta et al. (2021)	Flow velocity, flow depth, momentum flux and moment of momentum flux	Pier drift ratio	--	<ul style="list-style-type: none"> • Hydrodynamic drag force applied as pressure in OpenSees analysis. • Nonlinear static pushover analysis done to determine capacity.

Table 2-5 Continued.

References	IM	EDP	Variables	Methodology
Zhu et al. (2021)	Wave height, surge height, wave steepness, trapped air ratio, wavelength and submerged ratio.	Deck overturning and unseating, bearing damage	--	<ul style="list-style-type: none"> • Solitary wave theory for hydrodynamic wave simulation • FE modeling in ANSYS Fluent
Huang et al. (2022)	Significant wave height	Deck and rubber bearing capacity in vertical and horizontal directions.	Concrete compressive strength, steel yield strength, tensile and shear strength of bolt, flange height and width of the web.	Time varying wave load modeled using potential flow theory.

Chapter 3 Finite Element Modeling of the Bridge and Wave Load

Calculation Method

3.1 General

This chapter presents the methodology used to develop the numerical FE model of the coastal bridges exposed to extreme wave loads. The detailed FE model is implemented in OpenSees where a fiber modeling approach is adopted taking the material and geometric nonlinearity into consideration. A total of 20 FE models are developed for the purpose of generating fragility curves for bridges subjected to wave-induced loads. Details of the geometric and material properties of the superstructure and substructure elements are provided. Techniques adopted for fiber discretization, concrete and reinforcing steel modeling, as well as pounding elements, abutment backfill soil, elastomeric bearing, and shear key modeling are illustrated in detail. The modeling technique is then verified against experimental results with satisfactory agreement upon comparison. This chapter then presents the overall methodology of the wave load calculation technique adopted in this study. Linear wave theory is followed to generate wave particle velocity and acceleration in order to compute the time history of the total wave force acting on the bridge. The total wave force is composed of buoyancy, drag, inertia, and slamming force components. The intensity measure (IM) considered are wave period (T_w), wave height (H_w) and still water depth (d_s). Both horizontal and vertical profiles of each wave force component are generated for their application on the bridge piers and deck. The wave load calculation method is then validated using the results from past literature involving experiments with similar wave loading conditions as adopted in this study.

3.2 Description of the case study bridge

The case study bridge selected is a three-span reinforced concrete (RC) I-girder superstructure supported on two abutments at the ends. The RC deck is 12.18 m wide with a thickness of 250 mm and span lengths of 33.0 m, 40.0 m, and 33.0 m, respectively. The spans are supported on two intermediate circular double pier bents connected to RC cap beams. The pier diameter is 1.5 m with heights of 16.5 m and 11.5 m, respectively. The longitudinal reinforcement in the piers is variable whereas the spiral transverse reinforcement is the same with 15 mm diameter with a pitch of 65 mm. The superstructure is assumed to have a strong connection with the substructure to

minimize the relative movement between these two. Elastomeric bearings having a plan dimension of 600×425 mm and a total height of 116 mm are installed to aid in transferring forces from superstructure to substructure. Shear keys are also installed in the transverse direction at the cap beams and abutments to restrain movement of the bridge deck due to the vertical and horizontal components of the uplift and drag forces from waves. Such measures of a strong connection by means of shear keys are adopted in recent studies of bridges exposed to extreme wave-induced loads (Lehrman et al. 2012, Ataei 2013). The schematic diagram of the bridge considered in this study is shown in Figure 3-1. It is assumed that the pier foundations are supported by piles which allow greater lateral strength than that in piers. This strong foundation will ensure that any demand posed on the superstructure due to the extreme waves will be transferred to the piers leading to significant damage. To optimize between reducing the computational expenses and obtaining a reasonable number of data for fragility curve and system resiliency analysis, a total of 20 bridge models are developed with varying material properties and reinforcement ratios in the piers. The details of uncertainty distribution of the bridge model parameters will be presented in the following chapter (Chapter 4).

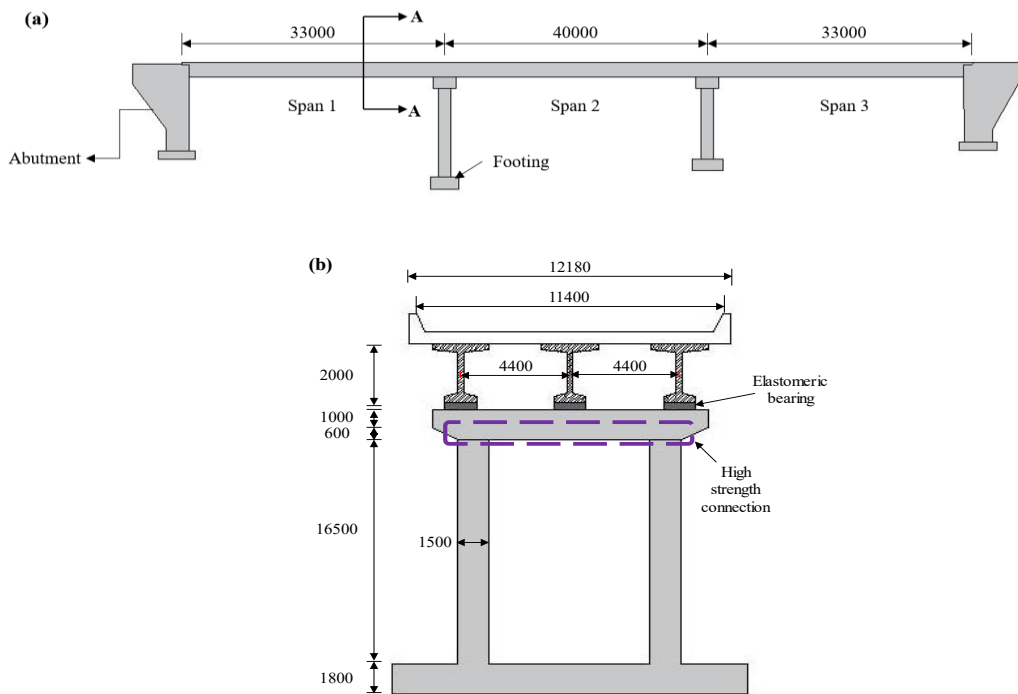


Figure 3-1 Details of the case study bridge (a) elevation view and (b) transverse view at section A-A (The dimensions shown are in mm).

3.3 Numerical Model of the Bridge

The three-dimensional (3D) nonlinear FE modeling of the bridge is done in the Open System for Earthquake Engineering Simulation (OpenSees) platform (McKenna et al. 2013). The FE modeling techniques involving simulation of solid elements are computationally more expensive to develop the required number of models for fragility analysis. OpenSees is an open-source platform which is computationally less expensive and hence is suitable for this study. The model properties and analysis commands are both implemented in the Tool Command Language (Tcl) which is completely programmable. The components of bridge are modeled as line elements that has 3D behaviour to be used in the domain. The deck and girders are assumed as elastic during the wave load interaction, whereas the piers are modeled using fiber section with displacement-based nonlinear beam-column elements. Fibre-based nonlinear beam column element modeling is generally achieved in two different approaches, 1) displacement-based beam column elements via the “*dispBeamColumn*” command and 2) force-based beam column element using “*forceBeamColumn*” command in OpenSees. In the displacement-based beam column element method, the approximate displacement field of the element is defined using the nodal displacements (Scott and Fenves 2006). Several elements are required to represent the distribution of plastic hinge along the member length using this method (Scott et al. 2004). On the other hand, only one element is required to represent the nonlinear response of the structural member with the help of integration points in the force-based beam column element method.

3.3.1 Material and Section Properties

The reinforced concrete material is modeled using *Concrete07*, whereas the reinforcement steel is modeled with *Steel02* material available in OpenSees. *Concrete07* material includes the Chang and Mander’s model (Chang and Mander 1994) to define the monotonic stress-strain relationship for unconfined and confined concrete. Other concrete models available in OpenSees such as the *Concrete02* is also considered. However, the numerical model validation section, later on presented in this study, reveals that *Concrete07* provided the most accurate prediction of the experimental results. *Steel02* material uses the Menegotto and Pinto model (Menegotto and Pinto 1973) later modified by Filippou et al. (1983) to include isotropic strain hardening. The parameters used to represent the transition from initial elastic stage to strain hardening stage are considered as: $R_0 = 10$, $cR_1 = 0.925$ and $cR_2 = 0.15$ with a strain hardening ratio of 0.01. Transverse steel

reinforcements are not explicitly modeled in fiber-based modeling approaches. However, the effect of transverse reinforcements is included in the confined concrete properties. It is assumed that perfect bond exists between concrete and reinforcement and the slip between them is zero. Therefore, the bondslip between concrete and rebars as well as the corresponding strain penetration at the base of pier is neglected. Similar approach is also followed by Qeshta (2019). Nonlinear displacement-based beam column elements are used to model the piers to simulate the distributed plasticity model. The discretized fiber section adopted in this study is presented in Figure 3-2. Pier fiber sections are aggregated to a single material section.

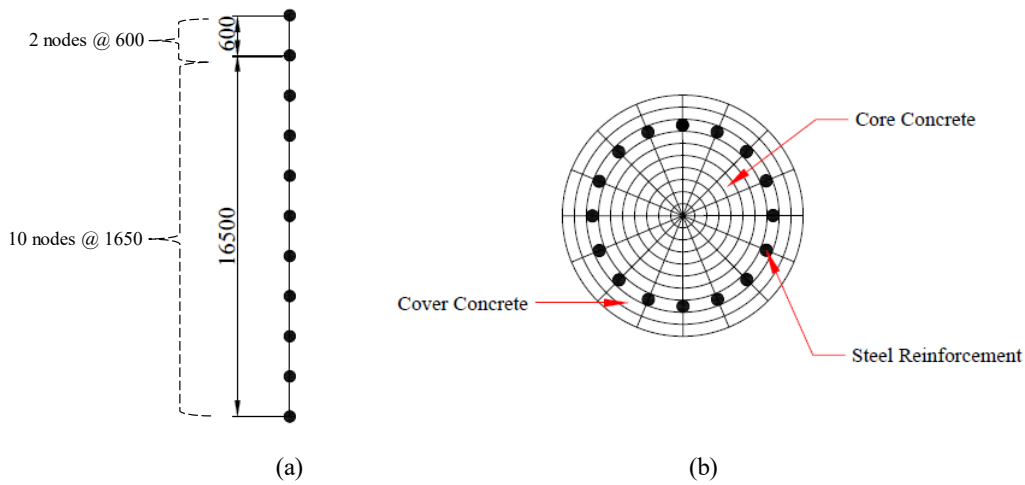


Figure 3-2 Numerical model of the bridge pier (a) Displacement-based nonlinear beam column element and (b) Fiber discretization adopted for the piers. (The dimensions shown are in mm).

3.3.1.1 Abutment Backfill Soil

The response of abutment is composed of two types of resistances; the passive resistance is provided by the backfill soil whereas the active resistance is contributed by the piles alone. As pile foundation modeling is not considered in this study, the modeling of active response is neglected. To capture the response of abutment backfill soil in passive response, a non-linear soil model is adopted using the hyperbolic gap material proposed by Duncan and Mokwa (2001) and Shamsabadi et al. (2007) available in OpenSees material library as *HyperbolicGapMaterial*. Figure 3-3 shows the force displacement response of the abutment backfill soil model used in this study. Equation 3-1 presents the force displacement relation used to simulate the material.

$$F(x) = \frac{x}{\frac{1}{k_{max}} + R \frac{x}{F_{ult}}} \quad (3-1)$$

where K_{max} denotes the initial stiffness, R_f is the failure ratio, and the ultimate passive resistance is denoted by F_{ult} . The recommended values from OpenSees is used to define the material behaviour. The value of K_{max} is taken equal to 20300kN per meter of abutment width, R_f is taken as 0.7 and F_{ult} is considered equal to 326kN per meter of abutment width. The gap in this model is considered to be 2.54cm.

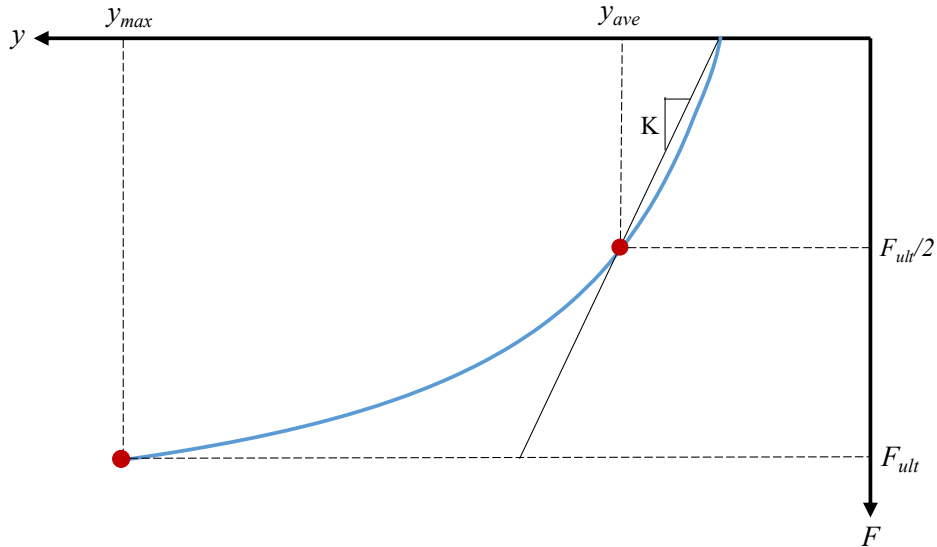


Figure 3-3 Force displacement response of abutment backfill soil

3.3.1.2 Elastomeric Bearing

Elastomeric bearings are one of the most commonly used type of bearings used in RC bridges. They are installed to transfer the forces with the use of friction and their performance is based on their sliding capacity which in turn depends on their initial stiffness. The response of the elastomeric bearing pads reduces to zero once the coefficient of friction is exceeded. With this characteristic in mind, this material can be sufficiently modeled using elastic perfectly plastic material (Ramanathan 2012). The elastomeric bearings are modeled in the transverse direction using *Steel01*. The elastomeric bearings are considered to have high stiffness in the vertical direction, therefore they are modeled as a high stiffness element vertically. Moreover, the bridge bearings considered in this study were not designed to resist the uplift of bearings. The bearings are simply placed under the girders without any positive attachment and just to accommodate rotation and translation. Equation 3-2 presents the formula used to derive the initial stiffness (k_{pad}) of the elastomeric bearings used in this study.

$$k_{pad} = \frac{G_{bearing} A_{bearing}}{h_{bearing}} \quad (3-2)$$

where $G_{bearing}$ represents the shear modulus, $A_{bearing}$ denotes the cross-sectional area and $h_{bearing}$ is the total bearing pad thickness. Figure 3-4 illustrates the force deformation response of the elastomeric bearing pad used in this study. In the figure, F_y represents the yield force which is computed by multiplying the normal force acting on the bearing pad with the coefficient of friction (μ) calculated from Equation 3-3 where σ_n denotes the normal stress on the bearing pad.

$$\mu = 0.05 + \frac{0.4}{\sigma_n} \quad (3-3)$$

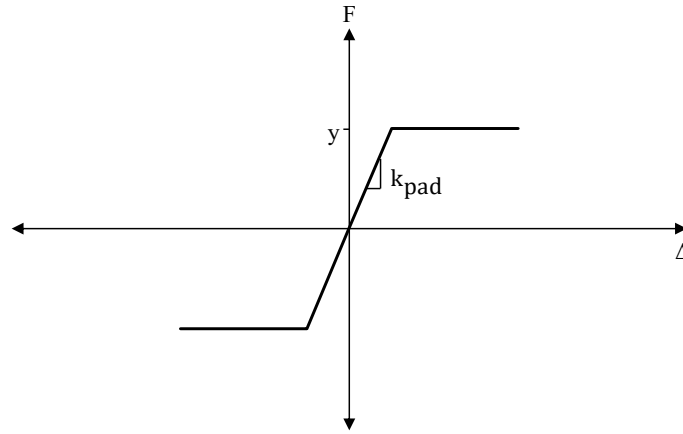


Figure 3-4 Force displacement response of elastomeric bearing pad

3.3.1.3 Shear Keys

As mentioned earlier, shear keys restrain the relative transverse movement between the abutments and the bridge deck. Typical failure of shear keys include flexure, shear friction, shear and bearing (Megally et al. 2002). *Hysteretic* material provided in OpenSees is used to model the shear keys. Following the method provided in CHBDC (CSA S6:19) and the study by Goel and Chopra (2008) the parameters of this hysteretic material are calculated. The force displacement relation for the hysteretic material representing the shear keys used in this study is shown in Figure 3-5. The displacement at each stage of damage experienced by shear keys are calculated using the formulas shown in Equations 3-4 to 3-7. U_y represents the displacement at yielding of steel reinforcement where visible cracks appear. U_n denotes the displacement at the onset of large cracks or concrete spalling, U_4 denotes the displacement when spalling and cracks reach the entire region and U_5 represents the displacement at which fracture of reinforcement takes place.

$$U_y = \sqrt{2}\varepsilon_y(L_d+L_a)\frac{(h+d)}{\sqrt{h^2+d^2}} \quad (3-4)$$

$$U_n = \sqrt{2}\varepsilon_y(L_d+L_a)\frac{(h+d)}{s} \quad (3-5)$$

$$U_4 = \sqrt{2}\varepsilon_{0.005}(L_d+L_a)\frac{(h+d)}{s} \quad (3-6)$$

$$U_5 = \sqrt{2}\varepsilon_{0.007}(L_d+L_a)\frac{(h+d)}{s} \quad (3-7)$$

Parameters used in estimating the displacements required to model the hysteretic response of shear keys are: the width of abutment front wall (L_a), reinforcement development length (L_b), shear key depth (d), shear key height (h) and spacing of reinforcement (s).

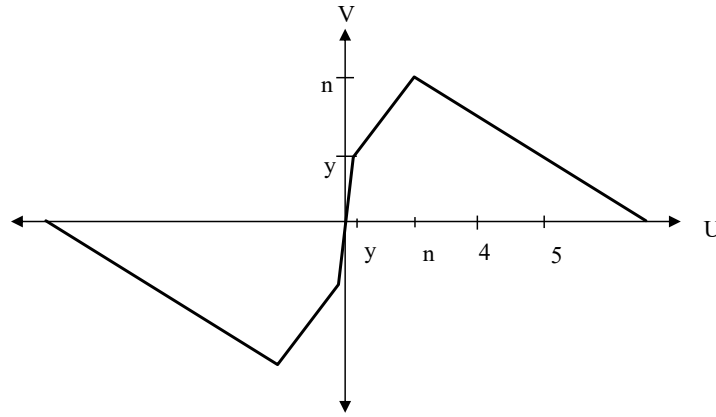


Figure 3-5 Force displacement response of shear keys

3.3.1.4 Pounding Element

The impact between the deck and abutment backwall is modeled using the contact element method developed by Muthukumar (2003). The bilinear truss element model of the pounding element is represented using the *ImpactMaterial* available in OpenSees. Figure 3-6 shows the force displacement response of the impact material used in this study. The stiffness parameters are denoted by K_{t1} and K_{t2} , δ_y and δ_m represent yield and maximum displacements, respectively. The values used to represent the material is computed following those presented by Nielson (2005). The spring constant k_h is taken as 2608 kip-in^{-3/2} per 1.9m width of abutment, the Hertz coefficient (n_{Hertz}) is taken as 3/2, coefficient of restitution (e) is taken as 0.8, δ_y and δ_m are considered as 2.54mm and 25.4mm, respectively. The gap is considered to be equal to 80mm. Effective stiffness (K_{eff}) of the truss contact element is taken as 456kN/mm per 1.9m width of abutment. The initial

and post-yield stiffness parameters (k_{t1} and k_{t2}) are taken as 1116kN/mm and 384kN/mm per 1.9m width of abutment, respectively.

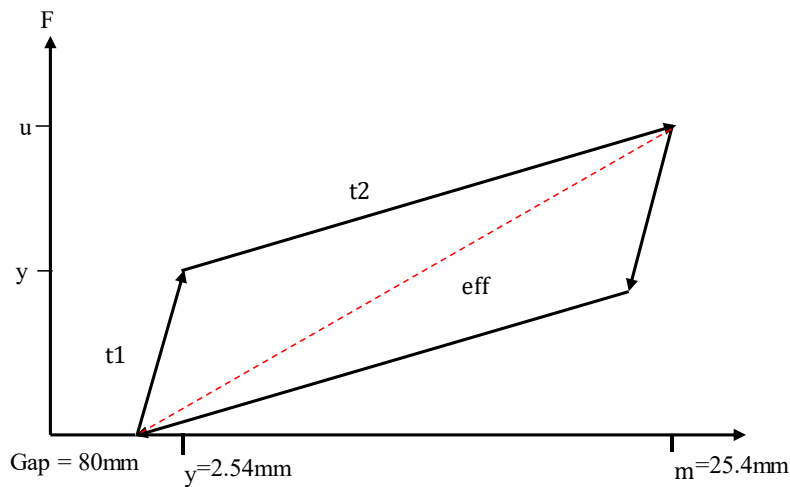


Figure 3-6 Force displacement response of the impact (pounding) element

The deck and girder composite section has a high stiffness, and so it is modeled as a rigid link. Rigid links are also used to connect the piers to the cap beams. Lumped translational and rotational masses are applied to the nodes to represent the mass. Piers are modeled as fixed connections at the base to represent strong foundation. Zero-length elements are assigned to the bearing pad, backfill soil material, pounding elements and shear keys. The wave load per meter is applied to the piers and deck using the uniform element load command (eleLoad) available in OpenSees.

3.3.2 Validation of the numerical model

The accuracy of the bridge modeling technique is verified by comparing the results from numerical analysis with that obtained from a sample column subjected to cyclic displacement loads experimentally. The wave load time history considered in this study is in the form of cyclic load, which is why an experimental result of cyclic displacement load is selected to verify the adequacy of the modeling technique. Moreover, no experimental results involving the force-displacement relationship of bridge piers under wave load exist as of yet. Column A2 from Kunnath et al. (1997) is selected for this purpose. The column under experiment was subjected to three cycles of displacements at 1.0%, 1.5%, 2.0%, 2.5%, 3.0%, 4.0%, 5.0% and 6.0% drift ratios until the column failed. A smaller drift of 0.5% was included in between each drift increment to characterize the system stiffness at the end of each displacement cycle imitating the action of seismic loads on the column. The comparison between the numerical and experimental results is illustrated in Figure

3-7. The initial and hardening stiffness were found to match well with the strength envelope. The comparison shows that the difference between maximum force is 5.27% and that between the total energy dissipated is 4%. Therefore, it can be said that the nonlinear pier modeling technique adopted in this study can predict the response of piers under cyclic displacement loads with satisfactory accuracy. Therefore, the bridge modeling technique is considered acceptable.

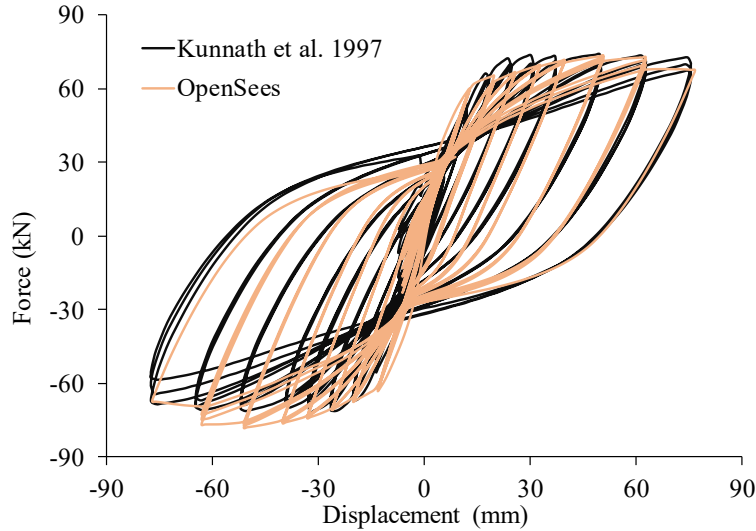


Figure 3-7 Numerical model technique validation using results of column A2 from Kunnath et al. (1997)

3.4 Wave Load Calculation Method

As water waves are dynamic in nature, a time varying wave force history is important to analyze the demand on the structural components. The study is divided into two wave loading conditions. Scenario 1 depicts the case when wave hit the piers only and are therefore not high enough to reach the deck. Scenario 2 presents the case when waves reach the deck after complete inundation of the substructure. The time varying velocity and acceleration profile for the wave particles are generated using the linear wave theory assuming that the wave is propagating harmonically. The wave length (λ) is typically not reported in the hazard data, so the dispersion theory is used to calculate the wave length as shown in Equation 3-8.

$$\lambda = \frac{g}{2\pi} T_w^2 \tanh \frac{2\pi}{\lambda} d_s \quad (3-8)$$

The nonlinear relation shown in Equation 3-8 is based on the gravitational acceleration (g) and the relationship between the T_w and λ . The water surface elevation (η) is calculated using Equation 3-9.

$$\eta = \frac{H_w}{2} \sin(\omega t - kx) \quad (3-9)$$

Variables in Equation 3-9 include the time considered in the analysis (t), horizontal position (x) corresponding to the instant t , wave frequency ($\omega = 2\pi/T_w$) and wave number ($k = 2\pi/\lambda$). For the scenario 1 where wave reaches only the piers, the horizontal velocity and acceleration profiles are generated using Equations 3-10 and 3-11, respectively.

$$u = \frac{\omega H_w}{2} \frac{\cosh k(z+d_s)}{\sinh kd_s} \cos(\omega t - kx) \quad (3-10)$$

$$\dot{u} = \frac{\omega^2 H_w}{2} \frac{\cosh k(z+d_s)}{\sinh kd_s} \sin(\omega t - kx) \quad (3-11)$$

For the scenario 2 when wave load applied at the deck, both horizontal and vertical profiles for velocity and acceleration are also required. Equations 3-12 and 3-13 present the sinusoidal profile for vertical wave particle velocity and acceleration, respectively.

$$w = \frac{\omega H_w}{2} \frac{\sinh k(z+d_s)}{\sinh kd_s} \sin(\omega t - kx) \quad (3-12)$$

$$\dot{w} = \frac{\omega^2 H_w}{2} \frac{\sinh k(z+d_s)}{\sinh kd_s} \cos(\omega t - kx) \quad (3-13)$$

The variable z used in the Equations 3-10-3-13 is the vertical position with respect to the d_s at the instant t . It is important to note that the time period used in each of the vertical and horizontal sinusoidal profiles of the quasi-static components are taken equal to the wave periods of the corresponding hazard parameter combination. Following the previous studies (Sheppard and Marin 2009, Ataei et al. 2010, Ataei and Padgett 2013), the slamming force profile is generated using a time period equal to 5/8th of the wave period to simulate the high transient impact due to wave actions. Although the still water depth varied according to the hazard combination considered in each simulation during the scenario 1, it is considered at a constant depth of 20.35 m for the scenario 2. The total wave force time history is calculated by considering the buoyancy force (F_b), drag force (F_d), inertia force (F_i) and slamming force (F_s). Equations for vertical ($F_{t,v}$) and horizontal ($F_{t,h}$) total wave loads are presented in Equations 3-14 and 3-15. Following the guidelines by CHBDC (CSA S6:19), the formulas for calculating each components are shown in Equations 3-16 to 3-22. It is assumed that the bridge is not skewed and therefore the line of wave action is exactly perpendicular to the bridge components, so lateral load component is neglected. Furthermore, the loads due to wave action (slamming force) are not computed using the empirical estimation formula, rather calculated directly as the site specific conditions of the bridge are known. The $F_{t,h}$ applied to the piers is up to a point where the wave height reached the pier above

the still water level. The wave load component calculation is heavily dependent upon corresponding coefficients, the drag force coefficient C_d is taken as 0.7 for the circular piers and 1.4 for the rectangular projected area of the deck as specified in CHBDC (CSA S6:19). The inertia coefficient C_m is taken as 2 whereas the slamming coefficient C_s is taken equal to π (Isaacson and Prasad 1993, Zhu et al. 2018). The suitability of such selection of coefficients are verified in the validation studies as described in the following section. The vertical and horizontal wave profiles generated for a typical hazard of 2.22 m wave height with a period of 5.5 seconds is shown in Figures 3-8(a) and (b). It is to be noted that the negative component in the vertical force time history represent the suction due to the impact of the wave actions. The overall magnitude of wave load is seen to be higher for the vertical component time history. Furthermore, three distinct peaks are observed during one wave period in both the vertical and horizontal wave force time histories similar to the observations by Marin and Sheppard (2009).

$$F_{t,v} = F_b + F_{d,v} + F_{i,v} + F_{s,v} \quad (3-14)$$

$$F_{t,h} = F_{d,h} + F_{i,h} + F_{s,h} \quad (3-15)$$

$$F_b = \rho g V_s \quad (3-16)$$

$$F_{d,v} = 0.5 \rho C_d A_h w^2 \quad (3-17)$$

$$F_{d,h} = 0.5 \rho C_d A_v u^2 \quad (3-18)$$

$$F_{i,v} = \rho C_m V_s \dot{w} \quad (3-19)$$

$$F_{i,h} = \rho C_m V_s \dot{u} \quad (3-20)$$

$$F_{s,v} = 0.5 \rho C_s A_h w^2 \quad (3-21)$$

$$F_{s,h} = 0.5 \rho C_s A_v u^2 \quad (3-22)$$

In Equations 3-16 to 3-22, the symbol ρ denotes the density of sea water (taken as 1023 kg/m³), V_s represent the submerged volume of the bridge component, A_v and A_h are the vertical and horizontal projected area of the component perpendicular to the wave propagation, respectively.

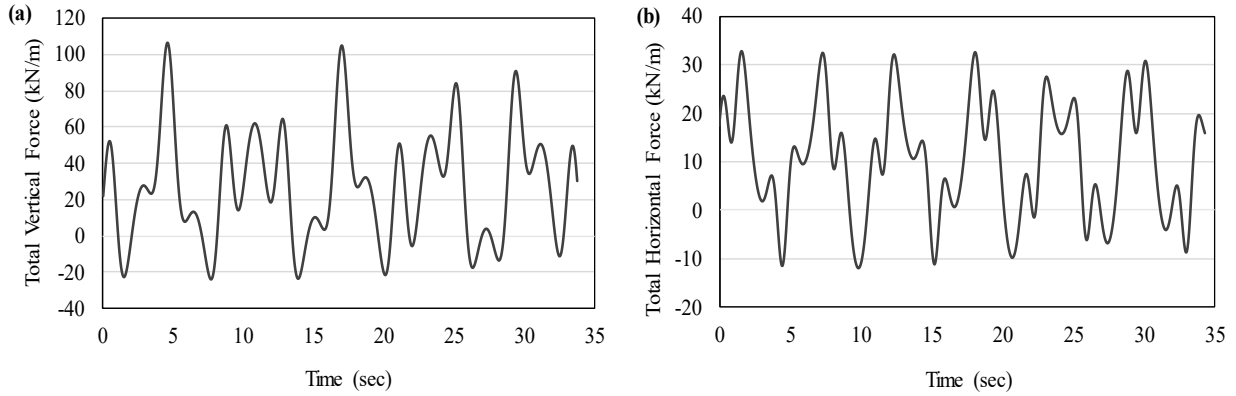


Figure 3-8 Total wave force time history in (a) vertical and (b) horizontal directions

3.4.1 Validation of the wave load calculation method

The wave load calculation method is also verified using the experimental study by Xiong et al. (2020) where a vertical truncated cylinder was tested with inland waves experimentally. The wave maker generated only quasi-static nature wave loads and so the Figure 3-9(a) shows how the numerical results of the quasi-static component (drag and inertia forces) compared with the experimental results. It is observed that, the wave load calculation technique can estimate the quasi-static forces within 7% of the actual obtained. Figure 3-9(b) shows the comparison with the experimental study by Hong et al. (2021) where a vertical cylinder was subjected to breaking wave loads, thus signifying the slamming effect on the structure. The selection of force coefficients (C_d , C_i and C_s) are deemed satisfactory as the calculated wave force profiles are in good agreement with the experimental results.

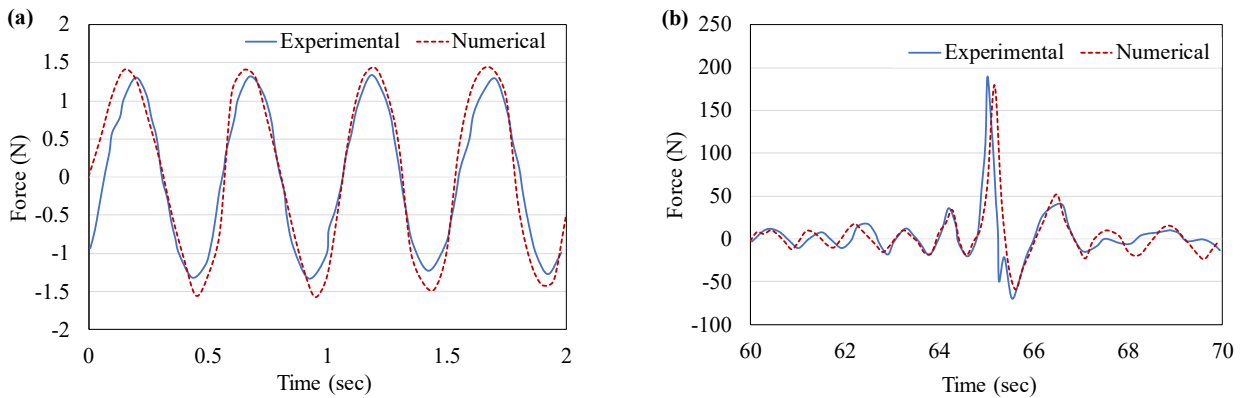


Figure 3-9 Validation of wave load calculation method using experimental results from (a)

Xiong et al. (2020) and Hong et al. (2021)

3.5 Summary

This chapter presents the overall methodology of the FE modeling and wave load calculation techniques chosen for this study. The FE model of the bridge is validated by comparing the results of an experiment involving cyclic displacements on a circular pier performed in past literature with those obtained in the pier FE model developed in this study. The variation in load displacement response of the experimental and numerical piers are within satisfactory limit and therefore the bridge modeling technique is deemed suitable for this study. Wave load calculation method involving the major components in vertical and horizontal directions is elaborately explained including its validation. The quasi-static force component (drag and inertia) and the high frequency impact force component (slamming) are compared with those obtained in experimental results of previous studies. The difference in comparison study is observed to be within 10% implying that the force coefficients considered for calculating the wave force coefficients are satisfactory.

Chapter 4 Methodology and Development of Performance-based Damage

States

4.1 General

This chapter presents the methodology considered in the fragility analysis including an overview of the component demands due to variation in the loading combinations selected in this study. This chapter also includes definitions of damage states developed and adopted to derive the fragility curves in the component level. Analysis results obtained from OpenSees are investigated to identify the variation in component responses due to the changes in hazard intensity levels considered. A detailed description of four damage states chosen for each of the component responses considered including pier drift, deck transverse displacement, elastomeric bearing and shear key deformations is provided. Results obtained from the OpenSees analysis are sorted in MATLAB to aid in the strain-based detection technique followed for identifying the pier drift-based damage state. Goodness-of-fit tests are performed for the drift values obtained at each stage of damage in both loading scenarios to identify the best fit distribution and thereby compute the limiting drift values.

4.2 Methodology

As mentioned in the previous chapter, two loading scenarios are considered in this study. Figures 4-1(a) and (b) present a schematic diagram of a wave profile reaching the superstructure and substructure components of a bridge for the two scenarios considered in this study. The selection of hazard intensity measures include wave period (T_w), wave height (H_w) and still water depth (d_s) based on past studies (Ataei et al. 2010, Gullett et al. 2012, Attary et al. 2017). The nonlinearity of waves arises primarily due to the effect of high winds. As wind is not within the scope of this study, the wave is considered as harmonic (linear). However, the high frequency slamming force presents the highly transient and non-linear nature of the random waves (Sheppard and Marin 2009, Ataei et al. 2010). Figure 4-2 represents the framework adopted in this study that leads to developing the fragility curves of the case study bridges under extreme wave loads. A total of 20 numerical bridge models with varying material properties and reinforcement ratios are generated in OpenSees (McKenna et al. 2013). For scenario 1, where the wave is expected to reach the piers only, a combination of 100 set of wave parameters (T_w , H_w and d_s) are generated using Latin

Hypercube Sampling (LHS) technique. Using the wave parameter combinations, 100 wave force time histories are generated. Each of the 20 bridge models are combined with 100 wave loads giving a total of 2000 simulations of wave loading on the bridge piers to be analyzed. Similarly, the 100 set of wave parameters (T_w and H_w) with a constant still water depth are considered for scenario 2. These time histories of 100 loading cases are then applied to the 20 bridge models so that 2000 further simulations are obtained for analysis. The component responses from these 4000 simulations are then recorded from OpenSees and further analyzed in MATLAB to develop the damage states for different bridge components (i.e. pier, bearing, shear key, deck). The maximum engineering demand parameters (EDP) are computed for each IM and compared with the damage states thus developed to finally generate the component level fragility curves. The system level fragility curves are then mapped using the component level curves assuming that a series connection exists between all the components.

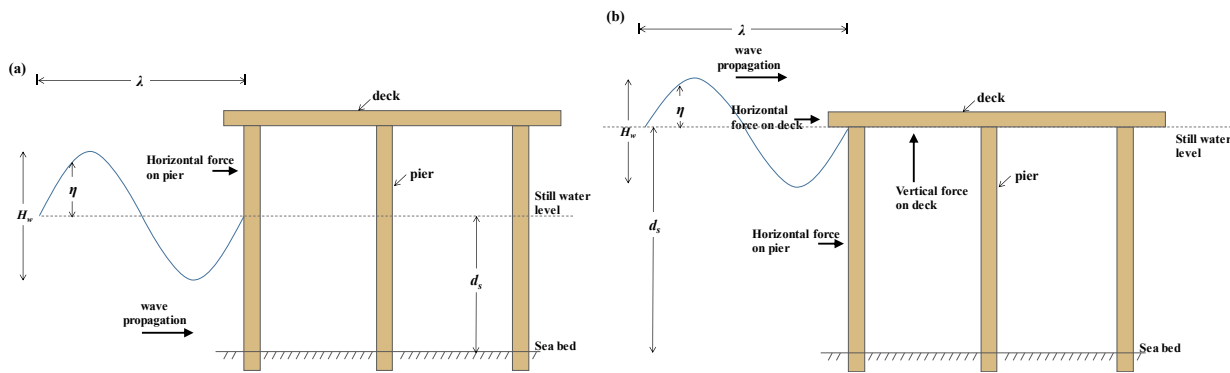


Figure 4-1 Schematic diagram of wave propagation towards a bridge structure showing (a) scenario 1 and (b) scenario 2 [adapted from Balomenos and Padgett (2018)]

4.2.1 Parameter Uncertainty

The combinations of wave parameters are derived using LHS considering the typical and maximum possible values obtained during the most devastating hazard ever experienced by the coastal bridges. The bounding limits for these parameters are considered using the post-survey data of Hurricane Katrina (2005) as a benchmark (Knabb et al. 2005, Robertson et al. 2007, NOAA 2020). Table 4-1 presents the parameters used as IMs in this study and the distribution considered for the analysis. A uniform distribution representing the uncertainties for each of the wave parameters is considered as it is difficult to identify the variation of these features during hurricanes or extreme wave conditions (Ataei et al. 2010, Huang et al. 2022). While the basic geometry of

the bridge models is the same, the material properties and reinforcement ratio are randomly generated, considering commonly used material properties in north American bridge construction, using LHS. As shown in Table 4-1, a normal distribution for concrete compressive strength (f'_c), a lognormal distribution for steel yield strength (f_y) and uniform distribution for longitudinal reinforcement ratio in bridge piers (ρ_s) are considered.

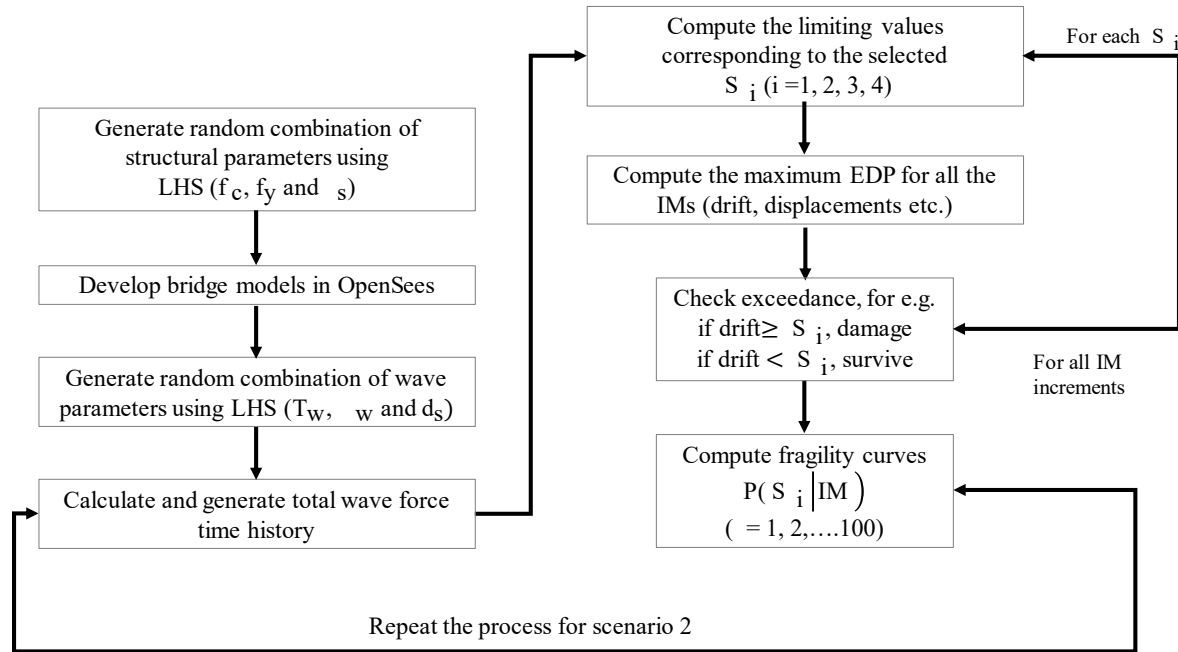


Figure 4-2 Framework adopted to develop fragility curves of coastal bridges subjected to extreme waves

Table 4-1 Uncertainties considered in fragility analysis

Parameter	Distribution	*Distribution Characteristics	Unit	Reference
Time Period (T_w)	Uniform	a = 14.00 b = 3.00	sec	(Robertson et al. 2007, Ataei et al. 2010)
Wave Heights (H_w)	Uniform	a = 16.00 b = 1.84	m	
Still Water Depth (d_s)	Uniform	a = 16.50 b = 3.00	m	
Reinforcement Ratio (ρ_s)	Uniform	a = 1.12 b = 1.50	%	--
Concrete Compression, (f'_c)	Normal	$\mu_{dist} = 30$ $\sigma_{dist} = 4.30$	MPa	(Billah and Alam 2021)
Steel Yield Strength (f_y)	Lognormal	$\lambda_{dist} = 6.13$ $\xi = 0.08$	MPa	(Ataei et al. 2010, Billah and Alam 2021)

*Note: a = upper limit, b = lower limit, μ_{dist} = mean of normal distribution, λ_{dist} = mean of lognormal distribution, σ_{dist} = standard deviation of normal distribution and ξ = standard deviation of lognormal distribution.

4.2.2 Variation in Component Demands

This section describes how the component responses varied with respect to the IM considered and the material properties in the bridge piers. Figure 4-3 shows the variation in maximum responses obtained in the elastomeric bearing, deck transverse displacement and rebar strains for the bridge B1 for the scenario 1. For brevity, only eight load cases are shown in this section for an overall comparison. The value of each IM in the wave load parameter combination considered and material properties of B1 are summarized in Appendix B, Tables B1 and B2, respectively. It is observed that for W2, the responses from all components are the lowest whereas those for W5 is the highest. For instance, the maximum rebar strain observed for W2 is $30247\mu\epsilon$ and that for W5 is at $410070\mu\epsilon$. Similarly, the maximum elastomeric bearing and deck transverse displacements for the load W5 is observed to reach up to 550.33 mm and 700.28 mm, respectively. On the other hand, the maximum displacements observed due to W2 is only 2.65 mm and 11.58 mm for the bearing and deck transverse displacements, respectively. Figure 4-4 shows how the component responses varied for scenario 2 on B1. In general, it is seen that with the same T_w and H_w the maximum displacements and rebar strains obtained for scenario 2 are higher. This provides the fact that the intensity of wave-induced loads when applied at the deck level are higher than the case when waves hit the piers only. In addition to that, the d_s considered in scenario 2 is the highest among all the d_s levels considered in scenario 1. From the formula adopted for wave load calculation as discussed in chapter 3, it is evident that as the d_s increased, the wave velocity and acceleration also increased which increased the total wave force.

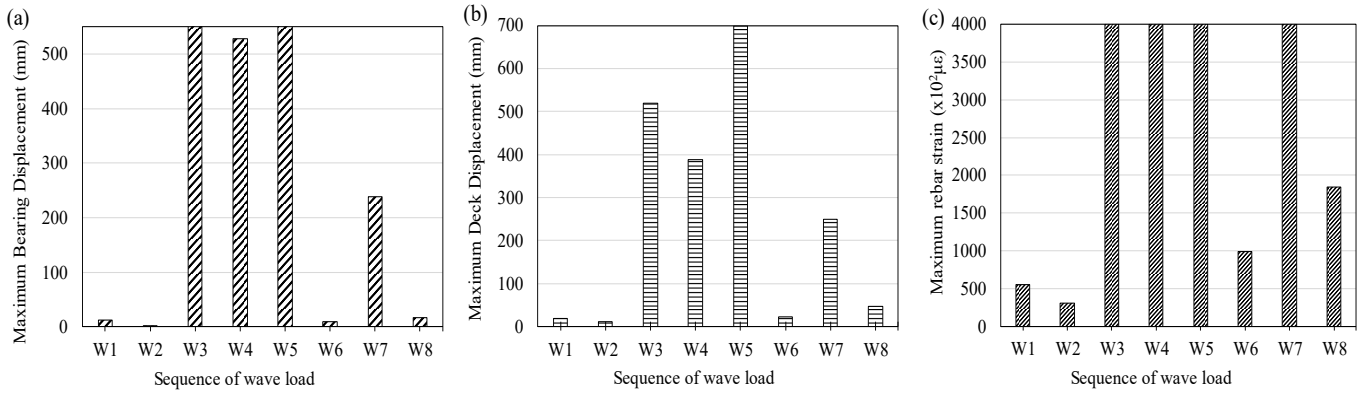


Figure 4-3 Variation in maximum component responses due to scenario 1 on B1

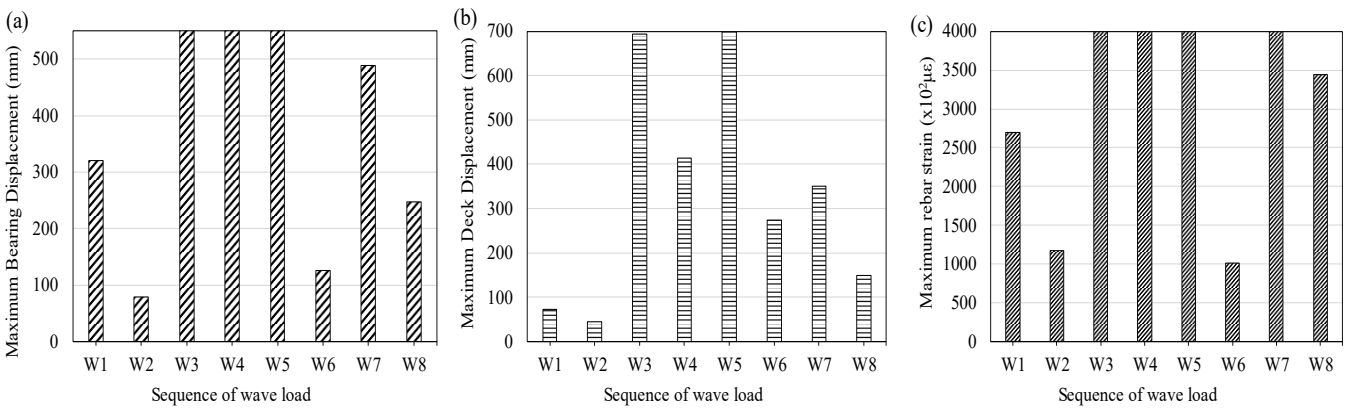


Figure 4-4 Variation in maximum component responses due to scenario 2 on B1

It can also be noted that, for the same d_s , the maximum responses from the bridge components are higher for lower T_w meaning that the intensity of wave load increased with decreasing wave periods. For instance, W2 and W4 has the same d_s at 8.04 m but with a period of 13.18 and 4.27 seconds, respectively. The maximum bearing displacement observed in B1 for scenario 1 are 2.65 mm and 528.88 mm for W2 and W4, respectively (Figure 4-3a). Similarly, the deck transverse displacement of B1 during scenario 2 are 44.19 mm and 413.60 mm for W2 and W4, respectively (Figure 4-4b), even though there is a significant difference in H_w . This identifies the fact that the wave period has the dominant impact on the intensity of the wave-induced loads. Figure 4-5 presents the maximum drift levels corresponding to the material strain at each of the damage stages for scenario 1 when the waves do not reach the deck height. For simplicity, four bridge piers are presented to provide a general idea of the variation in the pier performance with respect to two wave load cases W2 and W5 (Figures 4-5a and b, respectively). It is known that the column drift

capacity depends on the ratio of transverse reinforcement, axial load and the properties of reinforcement as well as concrete. In this study, the axial load and transverse reinforcement ratio are kept constant for all the bridge columns analyzed. It is seen that as the yield strength of reinforcing steel increased the yield drift capacity of the columns increased. For instance, B4 shows the highest yielding drift compared to B1 for both the load cases W2 and W5. Furthermore, the longitudinal reinforcement in B4 is observed to sustain higher buckling drifts. No bar buckling is observed in B4 for the load case W2 whereas a buckling drift of 9.64% is obtained when applied with a more severe load case W5. Similar findings are noted in the study by Kameshwar and Padgett (2014) where the response of columns is significantly affected by changes in steel yield strength. The spalling drifts for both the load cases shown here are found to be within 2% with the highest spalling drift shown by B2. The spalling drifts for all the cases analyzed are found to be within 3.5%. Figures 4-6a and b shows the pier drift levels obtained in scenario 2. It is noted that the drifts at all the damage stages are delayed compared to the pier loading scenario. For instance, the yielding and buckling drifts of B4 observed during scenario 2 with parameters of W5 are 3.42% and 10.87% whereas those obtained for scenario 1 are 1.12% and 9.64%, respectively. This could be due to the fact that the uplift components of the drag and inertia force, along with the buoyancy force created an axial tension in the piers which counterbalanced the axial compressive loads by the weight of the deck and the downward components of the wave force causing a delay in the response of material strain compared to waves on piers only.

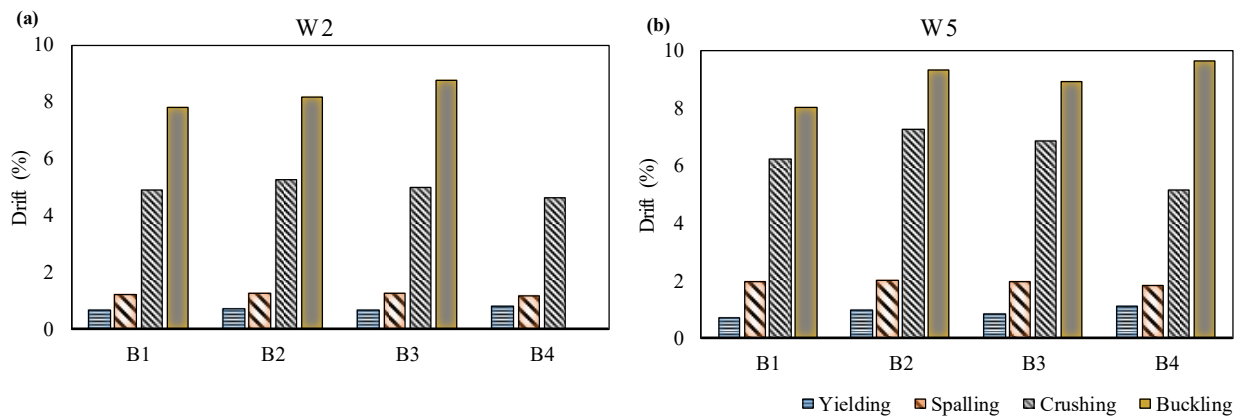


Figure 4-5 Variation of drift levels in four bridge piers for scenario 1 due to (a) W2 and (b) W5 combinations

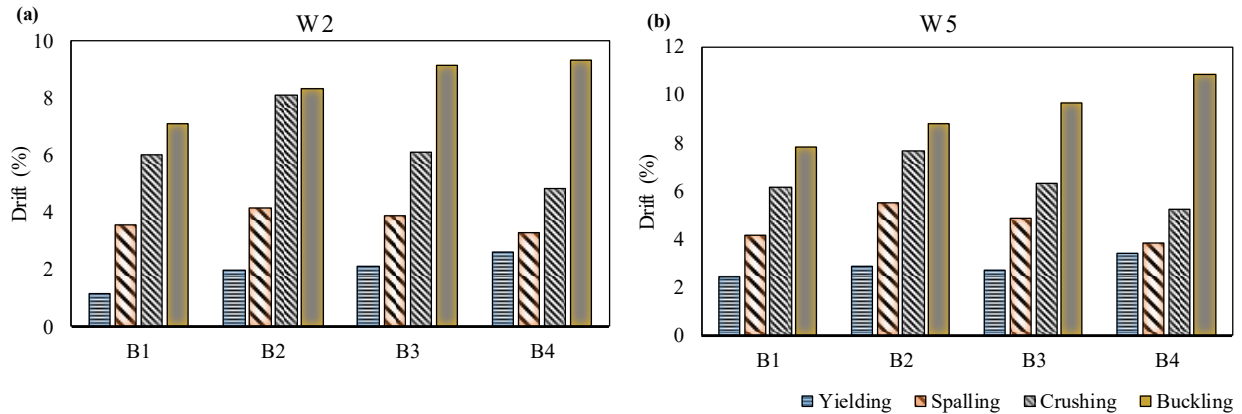


Figure 4-6 Variation of drift levels in four bridge piers for scenario 2 due to (a) W2 and (b) W5 combinations

4.3 Damage State Definition

Selection of proper DSs for the probability of failure analysis is the foremost criteria for successful implementation of performance-based design. According to Holmes (2000), any observable divergence in stiffness or structural strength from the original status, and complete or partial loss of design functionality is termed as a DS. Typical DS definitions are based on component drift or displacements. For instance, Billah and Alam (2016) developed performance-based DS based on pier drifts corresponding to hairline crack of concrete, yielding of longitudinal rebar, spalling of cover concrete and core concrete crushing. The drift levels were identified by strain-based damage detection corresponding to each DS. Ataei and Padgett (2013) developed global performance-based limit states based on the comparison between the load-deformation response of the pristine and damaged structure. The CHBDC (CSA S6:19) has specified four DSs based on the strain limits in concrete and steel reinforcement. The performance levels defined in the CHBDC code (CSA S6:19) are immediate service, limited service, service disruption and life safety. Only recently, the performance-based analysis of bridges under extreme wave loads are being studied and so there is limited literature available on component level DS development of coastal bridges. Most of the available literature is based on seismic loads where DSs for each of the bridge components are developed separately (Billah and Alam 2016, Stefanidou and Kappos 2017, Billah and Alam 2021, Stefanidou et al. 2022). For comparison purposes, the DSs adopted for bearing elements in this study are taken from the studies regarding seismic loads (Stefanidou and Kappos 2017). Figure 4-7 shows the schematic diagram of the shear deformation measurement of the elastomeric bearing pad used to define its DSs. The pier drift-based DSs are derived from material strain-based damage

detection technique following the study by Billah and Alam (2016). Four DSs are chosen for the pier drift levels namely, yielding, spalling, crushing and buckling. For the yielding stage, the onset of first yielding in the longitudinal reinforcing steel in piers is detected. The spalling stage is detected when the cover concrete reached the spalling strain of 0.004 (Priestley et al. 1996). Similarly, the crushing stage is detected when the core concrete reached the crushing strain (ε_{cu}) as calculated from Equation 4-1 (Paulay and Priestley 1992) and the onset of buckling strain (Equation 4-2) (Goodnight et al. 2016) in the longitudinal rebar in piers are identified as the buckling stage.

$$\varepsilon_{cu} = 0.004 + \frac{1 \cdot \rho_{sv} A f_{ys} \varepsilon_{sm}}{f'_c} \quad (4-1)$$

$$\varepsilon_{buckling} = 0.03 + 700 \rho_{sv} \frac{f_{ys}}{E_s} - 0.1 \frac{P}{f'_c A_g} \quad (4-2)$$

In Equations 4-1 and 4-2, ε_{cu} denote the ultimate compression strain, ρ_{sv} is the volumetric ratio of transverse steel, ε_{sm} represents the strain of steel at maximum tensile stress, f'_c is the concrete compressive strength, f_{ys} denotes the transverse steel yield strength, E_s is the Young's modulus of the transverse steel, P represents the axial load on columns and A_g is the gross area of column cross-section.

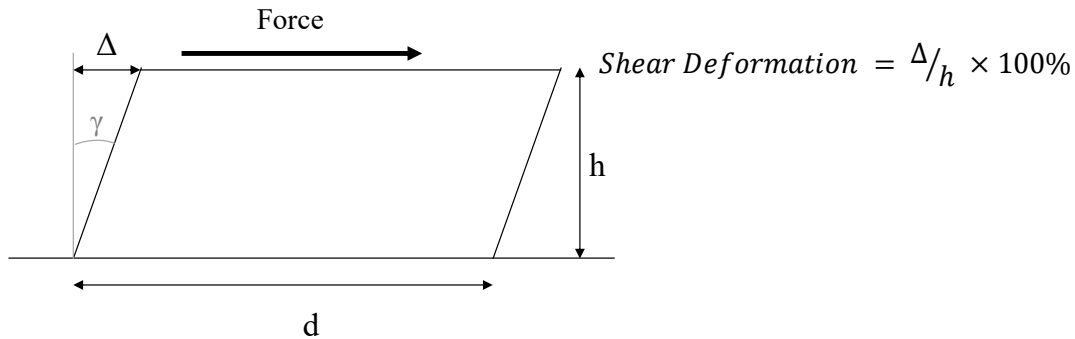


Figure 4-7 Schematic diagram showing the measurement of shear deformation of the elastomeric bearing pad

The pier drift levels corresponding to each of the damage stages are traced and the median drift level calculated from the appropriate distribution are then defined as the pier drift based DSs. Details of the pier drift DSs adopted for piers is summarized in Table 4-2. Table 4-3 summarizes the shear key DSs which are based on the visible damage in material properties corresponding to the displacements U_y , U_n , U_4 and U_5 from Figure 3-5 of Chapter 3. The deck DSs are taken to be

the same levels in transverse displacement as those adopted for shear keys. This is because the transverse movement of the deck is restrained using shear keys, so it is considered that when the shear key exceeds a particular DS the deck will also experience the same damage. In other words, the lateral restraining mechanism of the deck will start to weaken as soon as the shear key begins to fail. The details with respect to the damage states chosen for shear key and deck transverse displacement is summarized in Table 4-3.

Table 4-2 Pier drift-based damage states adopted in the study

Damage Indicator	Damage State	Level of function	Damage description
Rebar Yielding	S -1	Slight	First yield of longitudinal rebar (theoretical)
Cover Concrete Spalling	S -2	Moderate	Onset of cover concrete spalling
Core Concrete Crushing	S -3	Extensive	Core concrete crushing
Rebar buckling	S -4	Collapse	Buckling of longitudinal rebar

Table 4-3 Damage states adopted for the components

Component	Damage State	EDP	Limiting Values	Damage Description
Shear Key	DS-1	Drift	1.65%	Initiation of nonlinear behaviour (yielding)
	DS-2		15%	Visible damage to shear key
	DS-3		36%	Extensive damage, bonding failure
	DS-4		50%	Complete damage
Elastomer Bearing	DS-1	Shear Deformation	20%	Initiation of nonlinear behaviour
	DS-2		100%	Visible damage to the bearing; yielding of steel shims
	DS-3		200%	Lift off at the edge of the bearing, uplift and rocking; bonding failure between neoprene layers and steel shim plates
	DS-4		300%	Lift-off, rotation; unseating, failure of bearings.
Deck Transverse	DS-1	Displacement	7 mm	Initiation of nonlinear behaviour (yielding)
	DS-2		60 mm	Visible damage to deck
	DS-3		150 mm	Extensive damage, bonding failure
	DS-4		215 mm	Complete damage, significant pounding or unseating

4.3.1 Derivation of pier drift-based damage states

The results obtained from OpenSees are further analyzed using MATLAB to identify the limiting drift values corresponding to the strain-based damages. The variation in the drift values obtained for both the scenarios are examined to find out the suitable probabilistic distribution that best represent the variation of limiting drift values for each DSs. Four probabilistic distributions are chosen for this study which includes normal, lognormal, gamma, and Weibull distributions. By comparing the statistical measures from these chosen probabilistic distribution functions (PDF), the best fit function is identified. Goodness-of-fit tests at a particular confidence interval are the statistical tools used for the determination of the best fitting PDF to each limiting drift data variation. The normal distribution was chosen for its applicability in determining the accurate distribution of variables being affected by several factors (Mood et al. 1974). The distribution is symmetrical about the mean and only two parameters (mean and standard deviation) are required for its definition. The lognormal distribution is chosen as the drift data has no negative values and

the data is continuous. Gamma distribution is chosen as it excludes negative values and includes the variation in data that are right-skewed. Weibull distribution is chosen for its capability of representing both symmetrical and skewed distributions while handling high scatter in data points (Wagner et al. 1984, King 1987). Table 4-4 presents the functions of the probabilistic distributions chosen for goodness-of-fit tests for the drift level variations obtained in this study. The goodness-of-fit test compares the actual distribution of the data with the selected theoretical distribution and it is based on a null hypothesis which, if accepted at certain level of significance (α), the distribution is identified to fit the actual data.

Table 4-4 Definition of the probabilistic distribution functions chosen for goodness-of-fit tests

Distribution	Distribution Function	Parameter Definitions
Normal	$f(x) = \frac{1}{\sigma_x \sqrt{2\pi}} e^{-\frac{1}{2}\left(\frac{x-\mu_x}{\sigma_x}\right)^2}$	x = data μ_x = mean of data σ_x = standard deviation of data
Lognormal	$f(x) = \frac{1}{x \alpha_{\ln(x)} \sqrt{2\pi}} e^{-\frac{1}{2}\left(\frac{\ln(x)-\mu_{\ln(x)}}{\sigma_{\ln(x)}}\right)^2}$	$\mu_{\ln(x)}$ = mean of $\ln(x)$ $\sigma_{\ln(x)}$ = standard deviation of $\ln(x)$
Gamma	$f(x) = \frac{x^\lambda}{\beta^\lambda \Gamma(\lambda)} e^{-\frac{x}{\beta}}$ $\Gamma(\lambda) = \int_0^\infty u^{\lambda-1} e^{-u} du$	$\Gamma(\lambda)$ = gamma function $\lambda = \frac{\mu_x^2}{\sigma_x^2}$ and $\beta = \frac{\sigma_x^2}{\mu_x^2}$
Weibull	$f(x) = \frac{\alpha}{\beta} \left(\frac{x}{\beta}\right)^{\alpha-1} e^{-\left(\frac{x}{\beta}\right)^\alpha}$	α = shape parameter $\beta = \frac{\sigma_x^2}{\mu_x^2}$

Two of the most commonly used goodness-of-fit tests are the chi-squared test and Kolmogorov-Smirnov (K-S) test. The chi-squared test deals with data having only discrete values. Moreover, it is best for data having a particular distribution, thus not suitable for a variety of distributions being compared. Continuous data are binned to histogram cells which affects the accuracy of the goodness-of-fit test using the chi-squared method (Michael 1986). Therefore, this test is not suitable for the data obtained in this study. The K-S test compares the empirical distribution function (EDF) with the cumulative distribution function (CDF) of the assumed theoretical distribution. The K-S test allows exact results to be analyzed as opposed to the chi-squared test. This test only deals with continuous data and therefore K-S test is considered for the goodness-of-fit test in this study. The maximum vertical distance between the CDF and EDF is represented by the D test statistics as shown in Equation 4-3.

$$D = \max \left(\left| F(x_i) - \frac{i-1}{n} \right|, \left| F(x_i) - \frac{i}{n} \right| \right) \quad (4-3)$$

In Equation 4-3, n denotes the sample size, x_i denotes the data arranged in ascending order and $F(x_i)$ denotes the CDF of the chosen distribution. The first and second terms in Equation 4-3, represent the vertical distance between the CDF and EDF at the left and right of x_i , respectively. At 5% significance levels, the D statistic (D_{stat}) is compared with $D_{critical}$, as defined in Equation 4-4. The $D_{critical}$ is obtained from the table by Kanji (2006). The chosen probabilistic distribution is considered to fit the actual data at the significance level when the D_{stat} is less than $D_{critical}$. Details of the chosen distributions tested for the limiting drift value data corresponding to each scenario is summarized in Tables 4-5 and 4-6. A detailed step by step process for identifying the best fit distribution is outlined as below:

1. Selecting the damage indicators for each state
2. Using strain-based damage detection technique to find the limiting drift values at each DS.
3. Arranging the limiting drift data corresponding to each DS in ascending order.
4. Estimating the PDF parameters by the method of likelihood estimation.
5. Plotting of the PDF followed by CDF of the selected distribution.
6. Calculating the D_{stat} for the selected distribution using Equation 4-3.
7. Computing the $D_{critical}$ value for the corresponding significance level.
8. Pairing the obtained D_{stat} with $D_{critical}$ and the distribution is termed to fit when D_{stat} is less than $D_{critical}$.

$$P = [D_{stat} \leq D_{critical}] = 1 - \alpha \quad (4-4)$$

The value of $D_{critical}$ depends on the number of data and significance level tested. As the number of piers exceeding a particular DS varied, the variables n and x varied, and so did the value of $D_{critical}$ as seen in the two scenarios at each DS. It is observed that the drift data of all DSs fits at least two distributions. To identify the best fit, the smallest value of D_{stat} is used as it signifies that the difference between the CDF and EDF is the smallest among the ones compared. For instance, in DS-1 of Table 4-5, the data fits well with the normal and Weibull distributions. The normal distribution is identified to be the best fit as its D_{stat} is smaller (0.014) than that obtained for the Weibull distribution (0.029). Similarly, the best fit distribution for DS-1 scenario 2 is also normal with $D_{stat} = 0.017$ as opposed to the Weibull distribution with $D_{stat} = 0.030$. It is seen from Table 4-6 that the normal, lognormal and gamma distribution fits with the data variation in DS-4 of

scenario 2. The smallest D_{stat} value obtained these three distributions is given by the lognormal distribution and hence it is termed as the best fit distribution for the drift limit data at the rebar buckling stage.

Table 4-5 K-S goodness-of-fit test results at $\alpha = 5\%$ for the chosen distributions to represent the drift data obtained in scenario 1.

Distribution	Damage State			
	DS-1	DS-2	DS-3	DS-4
Normal				
D_{stat}	0.014	0.043	0.088	0.085
$D_{critical}$	0.033	0.033	0.036	0.043
Fit	Yes	No	No	No
Lognormal				
D_{stat}	0.059	0.020	0.031	0.032
$D_{critical}$	0.033	0.033	0.036	0.043
Fit	No	Yes	Yes	No
Gamma				
D_{stat}	0.092	0.018	0.060	0.071
$D_{critical}$	0.033	0.033	0.036	0.043
Fit	No	Yes	No	No
Weibull				
D_{stat}	0.029	0.053	0.056	0.042
$D_{critical}$	0.033	0.033	0.036	0.043
Fit	Yes	No	No	Yes

Table 4-6 K-S goodness-of-fit test results at $\alpha = 5\%$ for the chosen distributions to represent the drift data obtained in scenario 2.

Distribution	Damage State			
	DS-1	DS-2	DS-3	DS-4
Normal				
D_{stat}	0.017	0.050	0.072	0.039
$D_{critical}$	0.032	0.033	0.034	0.041
Fit	Yes	No	No	Yes
Lognormal				
D_{stat}	0.056	0.023	0.028	0.024
$D_{critical}$	0.032	0.033	0.034	0.041
Fit	No	Yes	Yes	Yes
Gamma				
D_{stat}	0.080	0.018	0.037	0.038
$D_{critical}$	0.032	0.033	0.034	0.041
Fit	No	Yes	No	Yes
Weibull				
D_{stat}	0.030	0.068	0.031	0.084
$D_{critical}$	0.032	0.033	0.034	0.041
Fit	Yes	No	Yes	No

The median drift values for the DSs calculated from the corresponding best fit distribution are then termed as the limiting drift level for that particular performance state. The median drift levels corresponding to each DS along with their probabilistic distribution are presented in Table 4-7. It is observed that for both loading scenarios the uncertainties in the yielding drift and spalling drift are represented using normal distribution and gamma distribution, respectively. Whereas, the lognormal distribution is found to best fit the uncertainties in the core concrete crushing and rebar buckling drift levels as shown in Figure 4-8. The limiting drift values for scenario 2 with completely submerged piers are found to be delayed compared to the scenario 1. For instance, the limiting drift at the first state in scenario 1 is only 0.91% whereas it is delayed up to 2.34% in scenario 2. Similarly, the cover concrete spalling limiting drift values are 1.48% and 3.61% in scenario 1 and 2, respectively. However, this difference in delayed pier drifts are reduced in higher damage levels considered where the buckling drift levels in scenario 1 and 2 are at 8.78% and 9.93%, respectively. To be more elaborate, the difference in crushing damage state drifts between scenarios 1 and 2 is 18% whereas that difference in the spalling damage state is 59%.

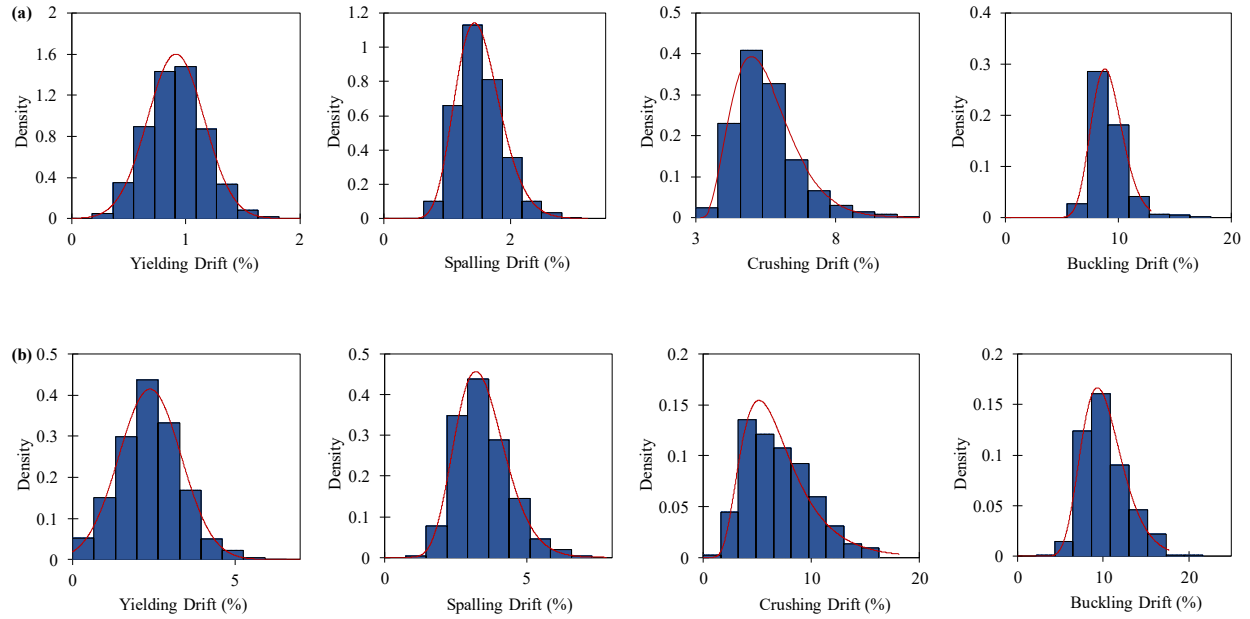


Figure 4-8 Distribution of the pier drift values corresponding to the four DS for (a) scenario 1 and (b) scenario 2

Table 4-7 Limiting drift values and their corresponding best fit distribution by K-S tests

Damage Indicator	Damage State	Limiting Drift (%)		Best Fit Distribution
		Scenario 1	Scenario 2	
Rebar Yielding	DS-1	0.91	2.34	Normal
Cover Concrete Spalling	DS-2	1.48	3.61	Gamma
Core Concrete Crushing	DS-3	5.34	6.53	Lognormal
Rebar Buckling	DS-4	8.78	9.93	Lognormal

4.4 Summary

This chapter explains the overall methodology followed for definition and derivation of component DSs for developing component and consequently system-level fragility curves. It is observed that the wave period is the dominant factor affecting the wave load intensity in both directions. For the same still water depth, the component responses obtained are higher for lower wave periods compared to those obtained due to higher periods. In scenario 2, it is found that the maximum responses of the bridge components analyzed are higher for the same combination of hazard intensity parameters. This identifies that scenario 2 caused greater intensity of wave-induced loads. The elastomeric bearing drift DSs are adopted following the seismic load analysis from past studies. Shear key and deck transverse displacement DSs are adopted based on the visible damage to material properties. This study is the first to employ strain-based damage detection technique to

determine the pier drift –based DSs under the action of extreme wave loads. It is observed that the wave period is the dominant factor affecting the wave load intensity in both directions. For the same still water depth, the component responses obtained are higher for lower wave periods compared to those obtained due to higher periods. In scenario 2, it is found that the maximum responses of the bridge components analyzed are higher for the same combination of hazard intensity parameters. This identifies that scenario 2 caused greater intensity of wave-induced loads. The distribution of drift values corresponding to each of the damage states as identified by K-S tests are normal (rebar yielding), gamma (cover concrete spalling) and lognormal (core concrete crushing and rebar buckling) for both the scenarios. The median drifts thus computed show that the first damage state is crossed when the drift is at 0.91% and 2.34% for scenarios 1 and 2, respectively. Similarly, the spalling limit state is exceeded at 1.48% and 3.61% for scenarios 1 and 2, respectively. However, this difference in limiting drift values in higher damage states between scenarios 1 and 2 decreases. The limiting drifts corresponding to the four damage states adopted for piers obtained in scenario 2 are delayed compared to those obtained in scenario 1 due to the axial tensile forces arising from the deck uplift by the waves thus altering the material responses in the piers.

Chapter 5 Fragility and Resiliency Assessment of Coastal Bridges under

Wave loading

5.1 General

This chapter presents the methodology used for developing the fragility curves of coastal bridges. The chapter begins with a definition of the multiple stripe analysis method used in this study for generating fragility curves. Details of the parameters required to fit the fragility functions are discussed and each step of the process is explained elaborately with equations. The bridge component fragility and consequently the system fragility curves under the IMs considered in the study are then discussed highlighting the identification of the most vulnerable component due to extreme waves. The chapter also describes the method followed for analyzing the bridge functionality and resiliency. The recovery functions and function parameters are selected based on previous studies regarding coastal bridge resiliency towards seismic and hurricane loads. Moreover, expert suggestions are followed for determining the distribution and bounding values of recovery function parameters. The results of functionality and resiliency are expressed in the form of indices. The chapter then concludes with a comparison of the variation in mean resilience index with respect to decreasing wave periods and increasing wave heights for both scenarios. Based on the mean resilience indices obtained, the bridge is then grouped into a specific resilient class following the method by Minaie and Moon (2017).

5.2 Fragility Assessment

The fragility function is typically defined using the lognormal cumulative distribution function as shown in Equation 5-1 where $P(DS | IM = x)$ presents the probability that the structure would exceed a certain DS due to hazard intensity with $IM = x$ and $\phi()$ which denotes the standard normal cumulative distribution. The parameters θ and β are median value of the fragility function and the dispersion of the IM, respectively. The multiple stripe analysis (MSA) (Baker 2015) for fitting fragility curves is best suited for this study as there are 20 different results for each of the 100 IMs analyzed. Therefore, it is difficult to note an increasing trend in the component responses exceeding a particular DS with increasing IM. The fragility function parameters (θ and β) are estimated based on the method of maximum likelihood function as presented in Equations 5-2 to 5-5.

$$P(S | IM=x) = \phi\left(\frac{\ln\left(\frac{x}{\theta}\right)}{\beta}\right) \quad (5-1)$$

$$P(z \text{ responses exceeding a } S \text{ fr om total analysis } n) = \binom{n}{z} p^z (1-p)^{n-z} \quad (5-2)$$

$$\text{Likelihood} = \prod_{i=1}^m \binom{n}{z} p^z (1-p)^{n-z} \quad (5-3)$$

$$\text{Likelihood} = \prod_{i=1}^m \binom{n}{z} \phi\left(\frac{\ln\left(\frac{x}{\theta}\right)}{\beta}\right)^z \left(1 - \phi\left(\frac{\ln\left(\frac{x}{\theta}\right)}{\beta}\right)\right)^{n-z} \quad (5-4)$$

$$\{\hat{\theta}, \hat{\beta}\} = \operatorname{argmax} \sum_{i=1}^m \left\{ \ln \binom{n}{z} + z \ln \phi\left(\frac{\ln\left(\frac{x}{\theta}\right)}{\beta}\right) + (n-z) \ln \left(1 - \phi\left(\frac{\ln\left(\frac{x}{\theta}\right)}{\beta}\right)\right) \right\} \quad (5-5)$$

where p_j is the probability that a particular hazard with $IM=x_j$ will cause the component to exceed a DS for all the m numbers of IM analyzed; n_j is the total number of analyses at each IM level which is equal to 20, whereas z_j is the number of responses that exceeded the DS considered therefore this number will be less than or equal to 20. The \prod represents the product of the binomial probabilities. Further details of the method of fragility curve fitting using the MSA is provided in following sections. The system fragility curves are then generated assuming there exists a series connection between the components.

5.2.1 Fragility Analysis Results

Figure 5-1 shows the process of fitting the fragility curve of pier drift for scenario 1 with respect to H_w considered in the study. The number of bridge piers crossing each DS is counted which is denoted by the fraction of analysis exceeding the DS in Figure 5-1(a). The fragility curves are then fit to the observed data by estimating the fragility function parameters (θ and β) through the method of maximum likelihood estimation as shown in Figure 5-1(b). The same process is done for all four DS adopted as presented in Figure 5-1(c). The fragility curves (Figures 5-2 to 5-5) present the comparison among the component responses under the two wave loading scenarios considered in this study.

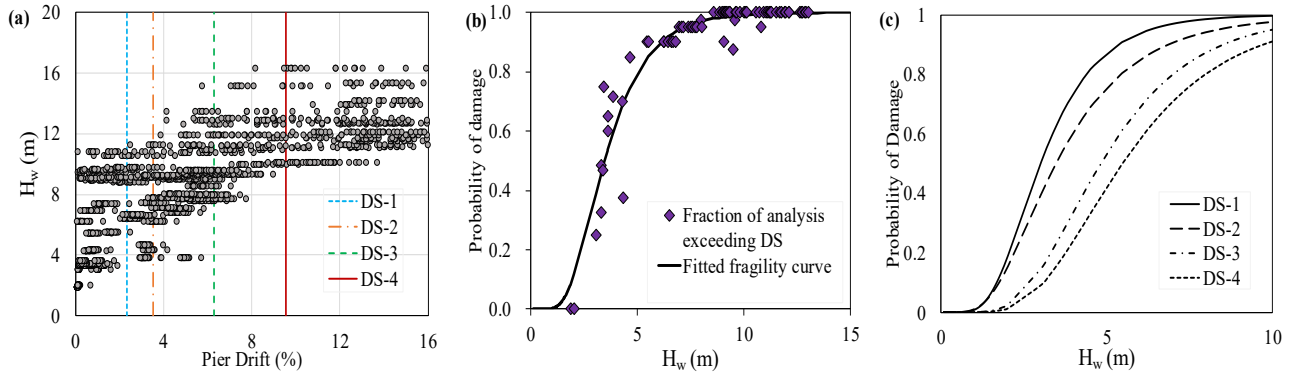


Figure 5-1 Process of fitting the fragility curve using MSA (a) Identification of fractions exceeding a DS, (b) Fitting of fragility curve, (c) Compilation of fitted fragility curves across all four DSs

As mentioned earlier, the wave force applied increased with decrease in T_w . Due to the inverse relation between wave period and wave frequency(ω), the fragility curves are plotted with respect to ω to put things into perspective. In general, the failure probability of the piers increased as ω increased which indicated that the vulnerability of the piers increased with decrease in T_w for both loading scenarios (Figures 5-2a and b). However, the vulnerability is higher in scenario 2 as the intensity of the total force due to waves reaching the deck is much higher than the other scenario. For instance, the probability of exceeding the DS-1 for piers is seen to be 80% and 82% in scenarios 1 and 2, respectively, for a frequency of 0.5sec^{-1} ($T_w = 12.57$ sec). Similarly, there is a 25% and 30% probability of pier collapse (DS-4) at 0.5sec^{-1} ($T_w = 12.57$ sec) when the waves reach the piers and deck, respectively. Interestingly, it is observed that even though the limiting drifts for each DS studied in this study are delayed in the deck loading case, the probability of damage are still higher than those observed for the pier loading case. This could be due to the fact that when wave reach the deck, the upward vertical load components (F_b , F_d , F_i and F_s) applied and overturning moments on the deck cause axial tension in the piers as well. This caused a reduction of the compressive stresses from the superstructure weight and downward vertical wave load components (F_d , F_i and F_s) in the piers, thereby decreasing the lateral load carrying capacity and hence the higher vulnerability. Figures 5-2c and d show similar trends in the vulnerability of piers corresponding to H_w . There is 60% probability of the piers to exceed DS-1 for scenario 1 whereas this probability increased to 95% for scenario 2 analyzed when $H_w = 4\text{m}$. Figure 5-2(e) presents the fragility curves plotted with respect to d_s for scenario 1 and it is observed that there is a 31% and 4% probability of crossing DS-1 and DS-4, respectively, when the d_s is at 10m. Balomenos

and Padgett (2018) also observed that, for the same inundation depth the probability of failure was increased with the decrease of the wave period for seaward pile-supported decks exposed to extreme coastal loads. Qeshta et al. (2021) studied the probability of failure of coastal rigid-frame bridges subjected to extreme waves and revealed that the probability of failure increased with increase in flow velocity for the same inundation depth. Similarly, it was also reported that for the same flow velocity, the fragility increased with increase in inundation depth (Qeshta et al. 2021). Figures 5-3(a) to (e) show the fragility curves for deck transverse displacement response for the two loading scenarios. The probability of crossing the extensive state (DS-3) at 3m wave height is about 37% higher in scenario 2 compared to that observed in scenario 1. Steeper curves are observed when the probability of damage are plotted corresponding to ω for the elastomeric bearing (Figures 5-4a and b). This means that the bearings are observed to have higher failure probability compared to the other components for a particular ω considered. For instance, the damage probability of the bearings to exceed DS-1 at $\omega = 0.5 \text{ sec}^{-1}$ is 85% whereas that obtained from the piers is 80% in scenario 1. It is seen that the piers begin to damage from $\omega = 0.2 \text{ sec}^{-1}$ whereas the shear keys begin to damage from approximately $\omega = 0.35 \text{ sec}^{-1}$ during scenario 1 (Figure 5-5). Upon observing scenario 1, the shear key deformation fragility curves are within the first three DSs when the span of wave frequency is between 0.35sec^{-1} to 0.7sec^{-1} . However, the pier drift fragility for the first three DSs for the same loading scenario lie in the range of 0.2sec^{-1} and 0.9sec^{-1} wave frequency revealing the fact that the extent of damage of the shear key components increase drastically with increasing wave frequency compared to the damage of piers. Such observations point out that the damage probability of the elastomeric bearing and shear key components are higher compared to the other components. It has been noted earlier that the main damage observed due to tsunamis is the breaking of bearing connection (Visser 2019). Similar findings observed in this study further confirms the coastal bridge failure mechanism.

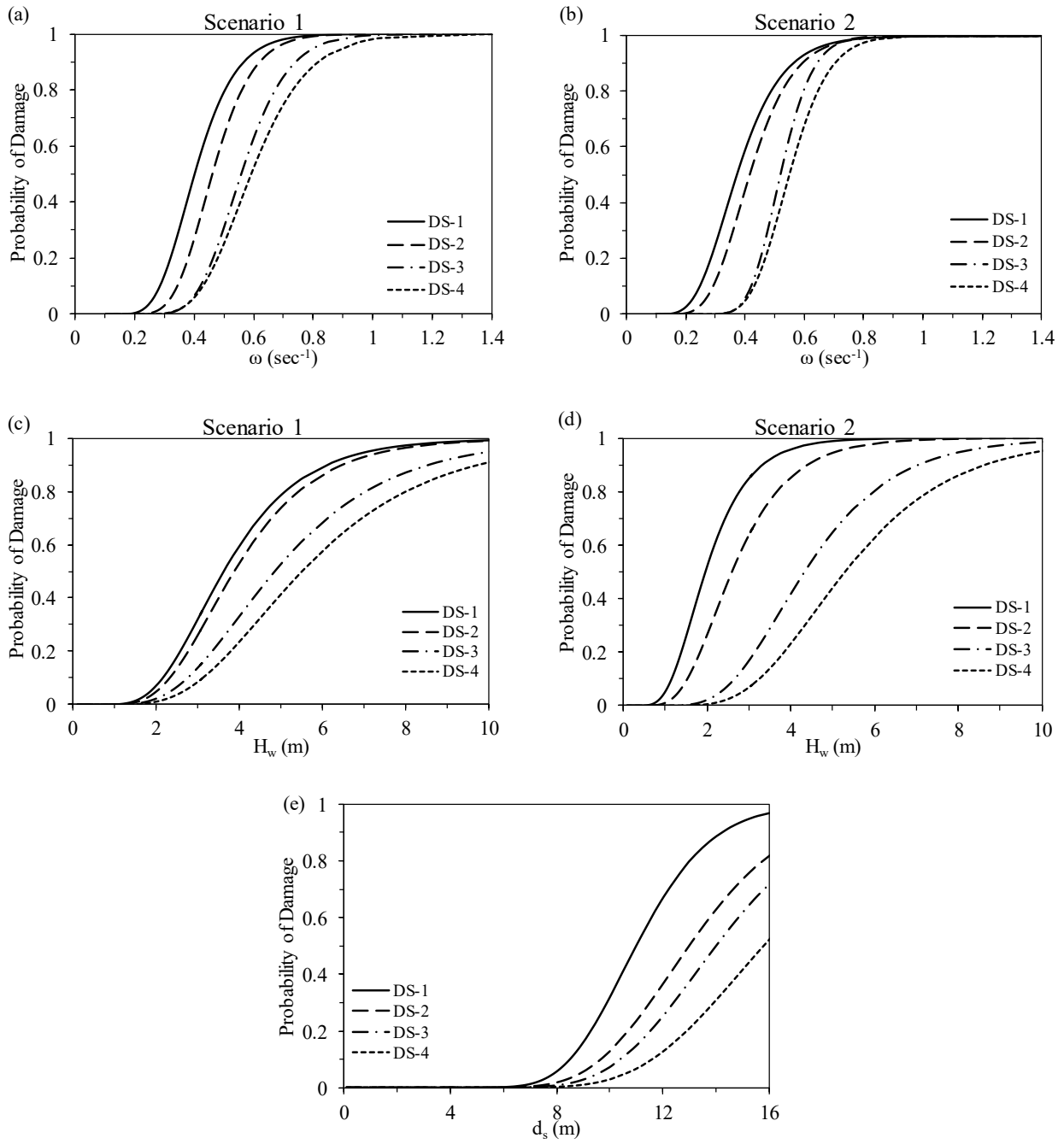


Figure 5-2 Fragility curves for the pier drift corresponding to (a and b) ω for scenario 1 and 2, (c and d) H_w for scenario 1 and 2, and (e) d_s for scenario 1

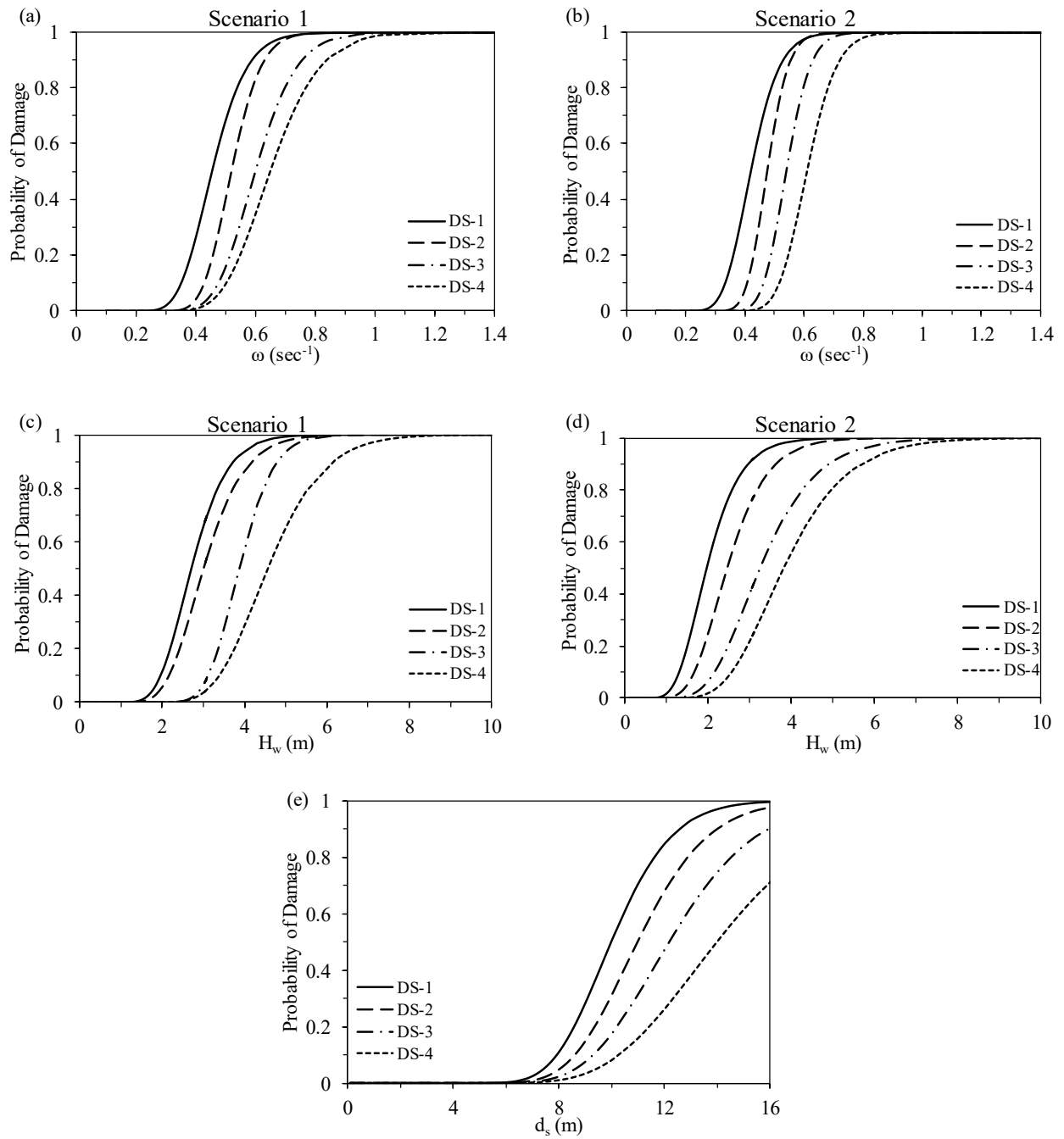


Figure 5-3 Fragility curves for the deck transverse displacement corresponding to (a and b) ω for scenario 1 and 2, (c and d) H_w for scenario 1 and 2, and (e) d_s for scenario 1

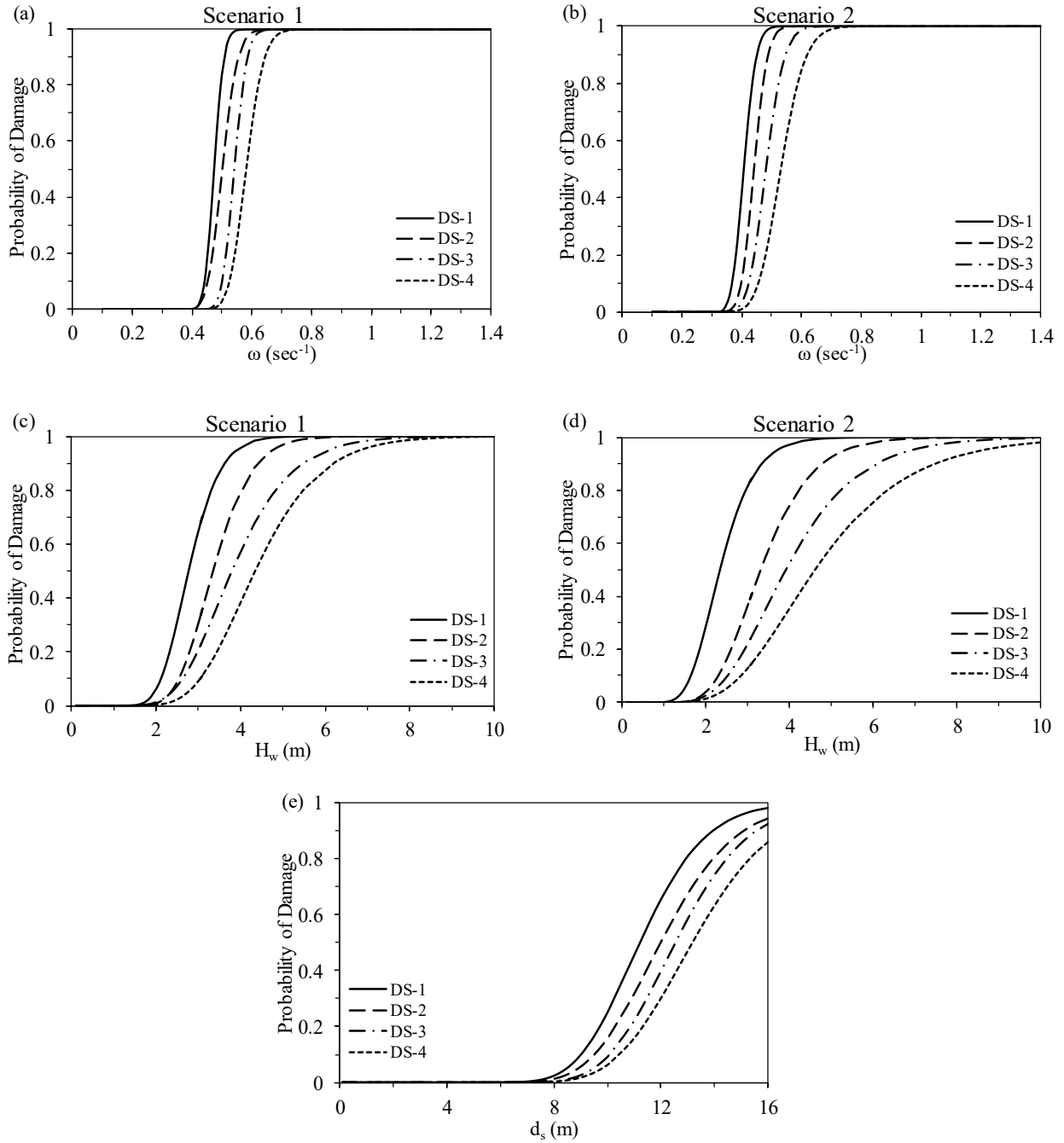


Figure 5-4 Fragility curves for the elastomer bearing deformation corresponding to (a and b) ω for scenario 1 and 2, (c and d) H_w for scenario 1 and 2, and (e) d_s for scenario 1

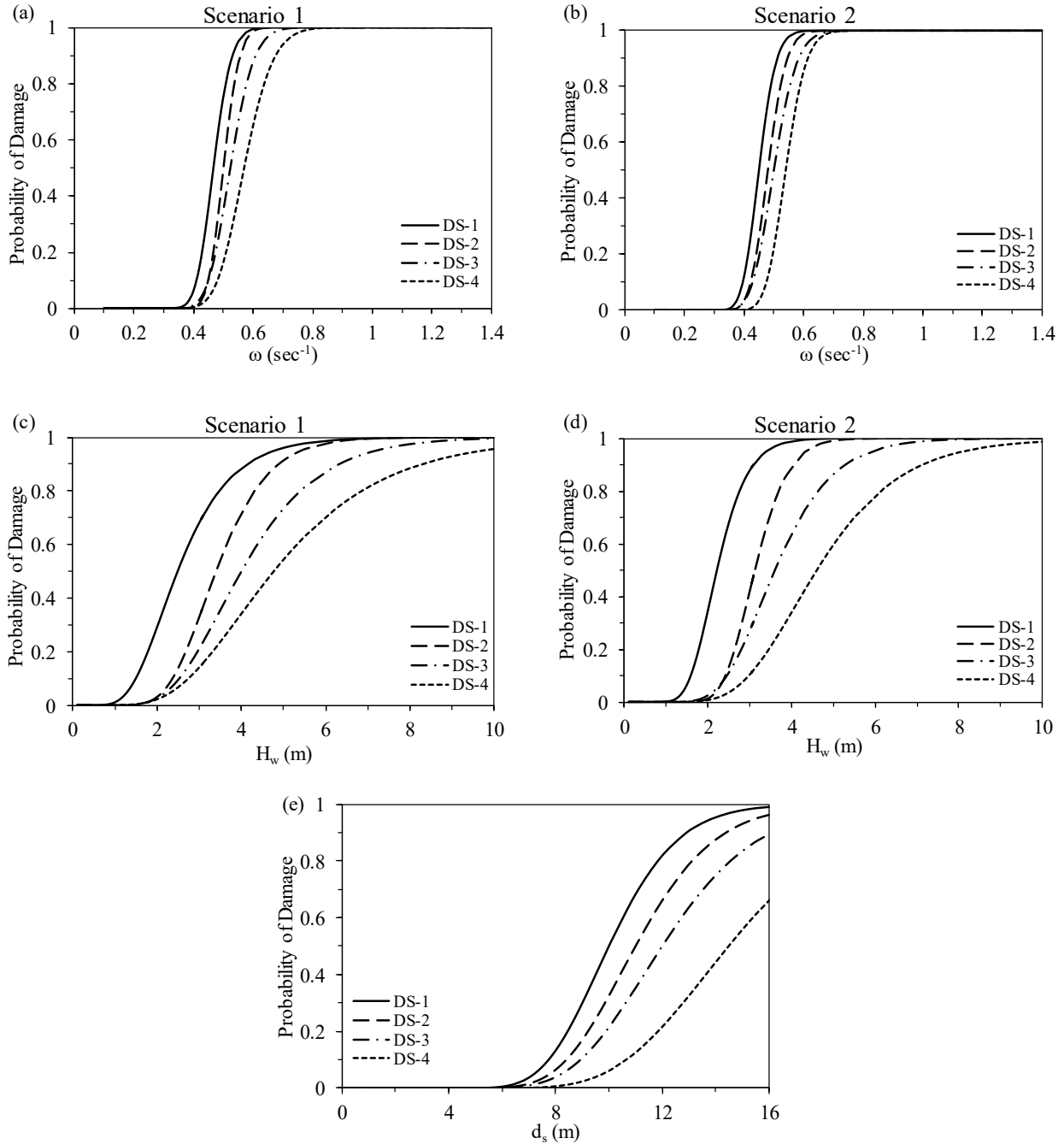


Figure 5-5 Fragility curves for the shear key deformation corresponding to (a and b) ω for scenario 1 and 2, (c and d) H_w for scenario 1 and 2, and (e) d_s for scenario 1

The system level fragility functions for wave loading at pier level (scenario 1) and at deck level (scenario 2) are presented in Figures 5-6 and 5-7, respectively. It is observed that, similar to the component level fragilities, the system fragility is also higher for the latter loading scenario due to the higher intensity of loads as waves reach the deck after completely inundating the piers. From

Figure 5-6(a), it is seen that for $\omega = 0.5 \text{ sec}^{-1}$, ($T_w = 12.57 \text{ sec}$) the system is completely in the slight and moderate DSs for the pier loading scenario. On the other hand, the system is completely in slight, moderate and extensive DSs for the same T_w during the scenario 2 (Figure 5-7a). Moreover, for wave actions at the deck, the system begins to fail when the ω is below 0.2 sec^{-1} compared to the other case where the system starts to exceed the slight DS at 0.2 sec^{-1} . At H_w 4m, the system is seen to be fully in the slight and moderate DSs for both the scenarios (Figures 5-6b and 5-7b). The system failure probability increased from 93% to 98% for extensive DS and 78% to 85% for the collapse state during scenario 1 and 2, respectively, at 4m H_w . In Figure 5-6(c) it is seen that the system is fully in the slight DS when still water is at 12m depth. At 50% probability of the system to exceed the extensive DS during the scenario 1, the shear key and bearings are observed to be the most vulnerable followed by the deck at the corresponding H_w of 3.04m. This adds evidence to the assumption that the deck begins to fail as soon as the shear key fails. On the other hand, the most vulnerable component during scenario 2 is the pier followed by the elastomeric bearings at 50% exceedance probability of extensive DS with an H_w of 2.53m. Furthermore, the shear keys are seen to be the most vulnerable component followed by the deck at 50% exceedance probability of the extensive DS corresponding to d_s of 10.25m. The system is expected to collapse completely when the d_s is at 16.3m and the H_w is approximately 6.8m at scenario 1.

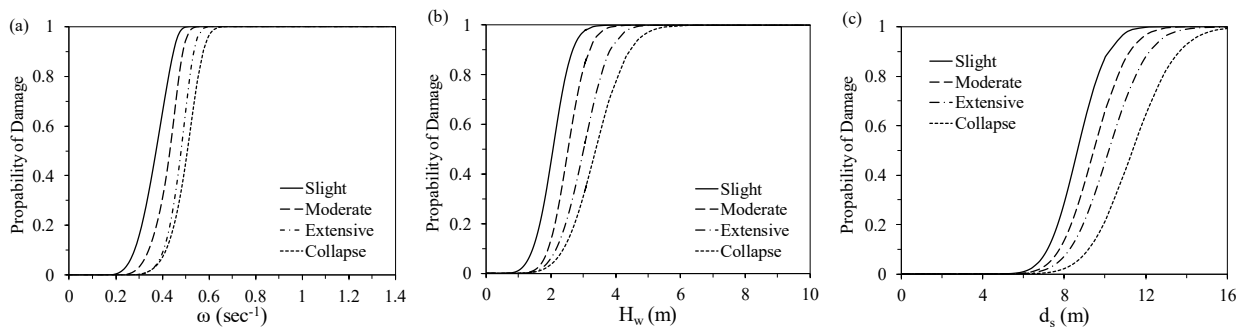


Figure 5-6 System fragility curves for scenario 1 corresponding to (a) ω , (b) H_w and (c) d_s

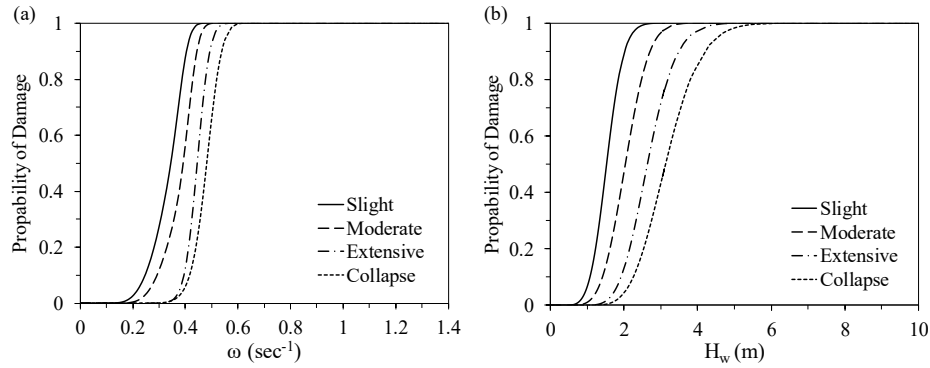


Figure 5-7 System fragility curves for scenario 2 corresponding to (a) ω and (b) H_w

5.3 Resiliency Assessment

The resiliency assessment of structures during and post hazard events dates back to 1973 (Holling 1973) where the resiliency and stability of ecology system was studied. Infrastructure resiliency became a topic of major concerns during the hurricanes Katrina, Ivan, Irene and Sandy (Minaie and Moon 2017). Resiliency is defined as the ability of a structure to withstand a shock while maintaining a certain functionality and regain a particular performance level within the shortest period of time (Argyroudis et al. 2020). Resiliency of a structure can be measured as time dependent as well as static (Frangopol and Bocchini 2011, Ouyang et al. 2012). In order to consider the aleatoric and epistemic uncertainties, the stochastic approach for resiliency assessment is followed (Decò et al. 2013). Bruneau et al. (2003) defined the four properties of resilience (4Rs) which are termed as robustness, redundancy, resourcefulness and rapidity. The robustness signifies the structure's ability to resist external hazard demands without sacrificing its functionality. According to Minaie and Moon (2017), robustness is also termed as the residual functionality subsequent to the hazard. Redundancy is the structure's ability to allow it for the alternate system to incorporate its original functionality when affected by external hazards (Zhu and Frangopol 2012). Resourcefulness is termed as the ability to mobilise the resources required to restore functionality under hazard events. Finally, rapidity is defined as the speed with which the loss of structure's functionality can be recovered. The robustness is measured through the fragility functions whereas the rapidity is measured from the recovery functions of the structure to regain a level of functionality. The recovery functions are typically based on expert opinions which depend upon the type and nature of hazard, the level of damage, availability of resources and requirements of the owner. Typical recovery functions used in past studies are summarized in Table 5-1. The conceptual definition of resilience is shown in Figure 5-8. The resiliency of a structure is generally

presented by the resilience index (R) as computed from the Equation 5-6 (Frangopol and Bocchini 2011).

$$R = \frac{\int_{t_0}^{t_h} Q(t) dt}{t_h - t_0} \quad (5-6)$$

where $Q(t)$ denotes the time dependent functionality with t representing the time, t_0 is the time when the hazard event took place and t_h denotes the investigated time horizon. The functionality $Q(t)$ is a dimensionless quantity that encompasses the damage state and the recovery process (Badroddin and Chen 2021). The functionality given a particular DS is computed following the Equation 5-7.

$$Q(t|DS_i) = Q_r + H(t-t_0-t_h) f_{rec} \left(\frac{t-t_0-t_h}{\delta_r} \right) [Q_b - Q_r] \quad (5-7)$$

where Q_r represents the residual functionality due to the hazard event at time t_0 . $H(\cdot)$ is the Heaviside step function that takes a value equal to zero for a negative argument. For instance, the $H(\cdot)$ takes on a value of zero when $t-t_0-t_h$ is negative and takes a value of one when $t-t_0-t_h$ is positive. δ_i denotes the idle time interval between the occurrence of the hazard and the immediate restoration response signifying that the functionality remains constant until the recovery process begins. δ_r is the recovery duration for the particular stage of damage. $f_{rec}(\cdot)$ denotes the recovery function that represents the process of recovery from the end of idle time. Q_b denotes the bounced back functionality at the end of the recovery process.

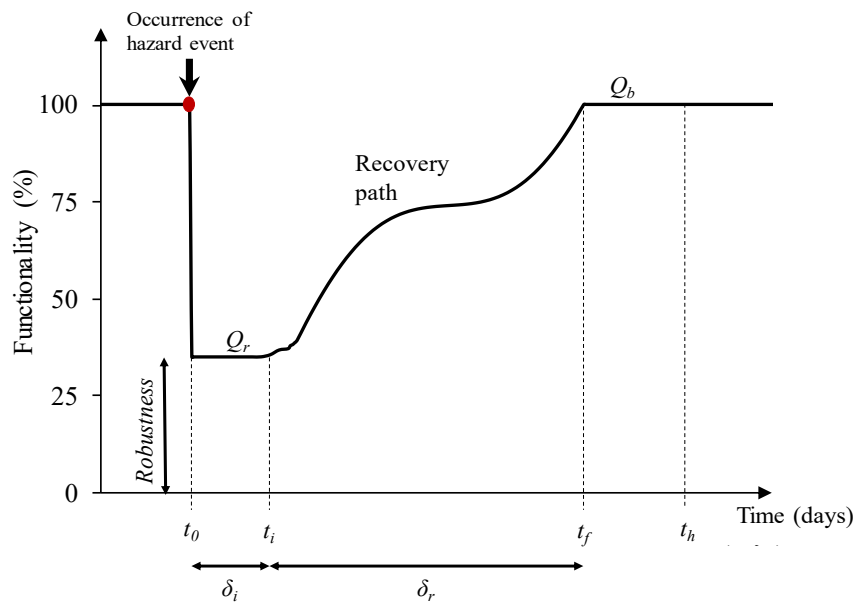


Figure 5-8 Schematic diagram defining resilience of a structure before and after a hazard event

Table 5-1 Typical recovery functions used in literature

Recovery Function	Definition	Symbols used	Reference
τ	Linear	$\tau = \frac{t-t_0-i}{r}$	(Cimellaro et al. 2010)
$0.5(1-\cos(\pi\tau))$	Trigonometric	--	(Chang and Shinozuka 2004)
$e^{-\alpha(1-\tau)}$	Positive-exponential	α =shape factor	(Biondini and Vergani 2015)
$1-e^{-\alpha\tau}$	Negative-exponential	α =shape factor	(Chang and Shinozuka 2004)
$1/(1+e^{-a(\tau-b)})$	Sigmoidal	a and b = shape parameters	(Vishwanath and Banerjee 2019)
$\phi(\tau - \frac{\mu_{t,ds}}{\sigma_{t,ds}})$	Damage-based normal distribution	$\mu_{t,ds}$ and $\sigma_{t,ds}$ = mean and standard deviation of the given damage state	(Hazus 2011)
$(\tau_{min,ds}, \tau_{max,ds})$	Damage-based uniform distribution	$\tau_{min,ds}$ and $\tau_{max,ds}$ = lower and upper bounds of the given damage state	(Shinozuka et al. 2008)

5.4 Details of Resiliency Assessment Framework

The process of quantification of resilience index can be divided into four primary steps: 1) computation of wave-induced forces, 2) Recording the component response due to the forces applied, 3) Derive the probability of failure from the maximum response obtained and the damage state adopted, and 4) The final step where post-hazard recovery functions are generated to derive the resilience index corresponding to the IM considered. These steps are derived from the basic procedure of Performance-based Earthquake Engineering (PBEE) by Pacific Earthquake Engineering Research (PEER) center (Günay and Mosalam 2013). Equation 5-6 is used for determining the resilience index (R) whereas the time dependent functionality ($Q(t)$) is computed using Equation 5-7. A probabilistic approach is followed for the resilience assessment where the residual functionality, idle time and recovery duration are considered as random variables. The distribution of these parameters depend on the corresponding DSs. The bounced back functionality (target functionality) is set equal to 1.00 implying that the system will be restored to full functionality or complete recovery. The selection of recovery functions for each of the four DSs are done following the past studies on resiliency assessment of bridges under seismic loads due to the inadequacy of literature encompassing studies on resiliency of the structures under extreme loads. The pattern of recovery depends upon the rehabilitation technique and scheduling (Decò et

al. 2013). In general, the slight damage of the structural system requires less time to recover to its desired functionality therefore fast paced negative exponential function works best to represent the restoration activity from the slight DS. A sinusoidal function represents the average pace with which a system recovers from the moderate damage due to the hazard event and restores its functionality gradually over the time. Finally, at the extensive and collapse DSs, the system goes back to its target functionality at the end of the recovery time, so it is best represented using a slow paced positive exponential function. A schematic representation of the recovery functions at each damage condition is shown in Figure 5-9. Equations 5-8 through 5-10 shows the recovery functions adopted in this study where $\tau = \frac{t-t_0-\delta_i}{\delta_r}$ and α denotes shape factor. According to Biondini et al. (2015), to effectively model the recovery profile based on the selected speed and magnitude of recovery functions, a proper tuning of the shape parameter is very important. Typically, α is assumed between 6 to 10 (Pang et al. 2020). It has been identified that the selected recovery profiles for bridges undergone similar level of damages are best represented using an α value of 10 (Biondini et al. 2015, Pang et al. 2020, Badroddin and Chen 2021). Following these past studies, the α selected in this study is 10.

$$f_{rec, slight}(\tau) = 1 - e^{-\alpha\tau} \quad (5-8)$$

$$f_{rec, moderate}(\tau) = \frac{1}{2} [1 - \cos(\pi\tau)] \quad (5-9)$$

$$f_{rec, extensive and collapse}(\tau) = e^{-\alpha(1-\tau)} \quad (5-10)$$

Table 5-2 presents the distribution and definition of the variables used to describe the recovery function parameters used in this study. A triangular distribution is chosen to represent the variation in recovery duration and residual functionality whereas a uniform distribution for the idle time is considered following the past studies on resiliency of structures subjected to seismic loads (Decò et al. 2013, Venkittaraman and Banerjee 2014). The bounding values for each of these recovery function parameters are selected based on the actual data obtained from the physical rehabilitation process of bridges after hurricanes, the practical field values considered during the rehabilitation of bridges after seismic events and formulas presented by Minaie and Moon (2017). It is assumed that the damage inspection is to be done by visual inspection and by using analytical techniques. The bridge is considered to carry an average daily traffic of more than 10,000 and less than 50,000. It is assumed that the replacement costs are less than 25% but more than 5% of the budget proposed by the agency and the bridge carries utility service lines. It is assumed that a proper extreme event

management practice will be followed after a hazard event and the bridge is in a region where moderate amount of hazards involving extreme waves happens each year. For the complete damage, zero residual functionality is considered. With the time dependent functionality thus defined using the recovery functions for each system damage conditions, the functionality with respect to the IM corresponding to each hazard condition considered in the study ($Q(t)$) is evaluated using Equation 5-11. The n_{DS} denotes the total number of DSs considered in this study. Functionality index obtained from Equation 5-11 is a value between 0 to 1, which is then used to finally compute the resiliency index (a value within 0 to 1) following Equation 5-6. The framework adopted for resiliency assessment in this study is presented in Figure 5-10.

$$Q(t) = Q(t|IM) = \sum_{i=0}^{n_{DS}} Q(t|S_i)P(S_i|IM) \quad (5-11)$$

For a particular IM, a number of iterations is carried out and the mean resilience index is reported as the resiliency of the coastal bridge. To achieve results with 95% confidence interval and a 1% margin of error the sample size obtained from statistical analysis for the required iterations is obtained as 10,000. Therefore, 10,000 samples of the recovery function parameters are generated using LHS and finally the mean resilience index is computed.

Table 5-2 Definition and distribution of variables used to derive the recovery functions

Symbol	Description	Damage State			
		Slight	Moderate	Extensive	Collapse
δ_r	Recovery duration (months)	T (0.33, 2.67, 5)	T (0.67, 3.67, 6.67)	T (2, 5.17, 8.33)	T (3.5, 7.25, 13)
Q_r	Residual functionality	T (0.5, 0.75, 1)	T (0, 0.25, 0.7)	T (0, 0.1, 0.4)	0
δ_i	Idle time interval (months)	U (1, 2)	U (1, 2)	U (1, 2)	U (1, 2)

*Note: T (a, b, c) = Triangular distribution with a and c being lower and upper bounds and b being the mode, respectively. U(a, b) = Uniform distribution with a and b being upper and lower bounds, respectively.

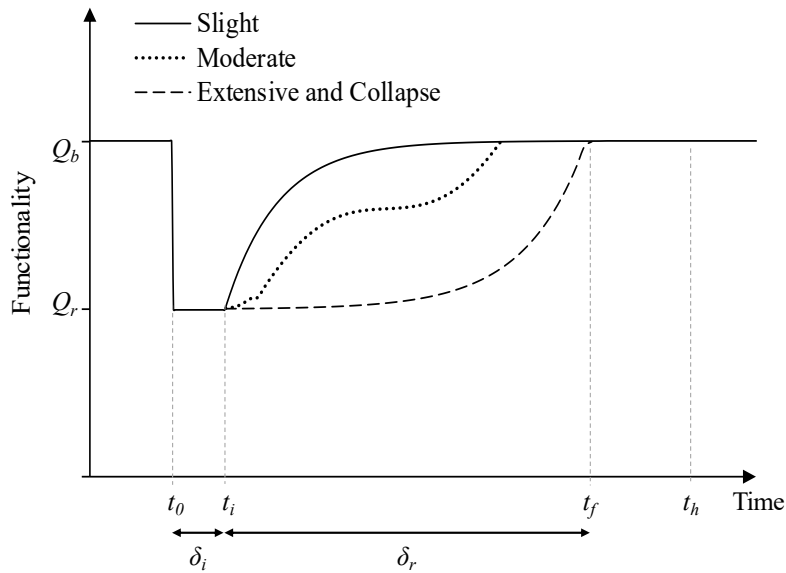


Figure 5-9 Schematic diagram of recovery functions at different damage stages chosen for this study

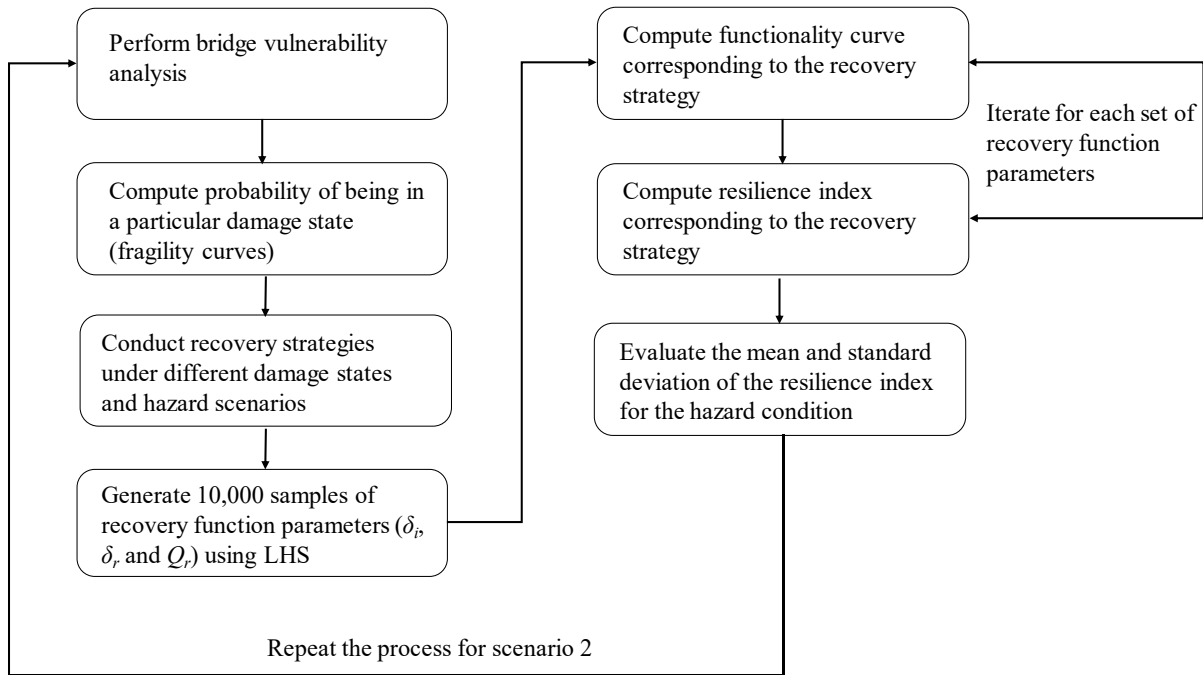


Figure 5-10 Framework adopted for resilience assessment in this study

5.4.1 Resiliency Analysis Results

It is seen that, in general, the variation in sample resiliencies is higher for higher intensity hazards. The functionality is represented using an index where 1.00 signifies that the system is in full function with no loss in performance. It is seen that as the intensity of the hazard increased, the residual functionality decreased and the area under the functionality curve decreased therefore revealing that the resiliency reduces. Figure 5-11 presents the mean functionality curve and resilience indices for scenario 1 with respect to T_w . Figure 5-11(a) shows that the mean resiliency is 86.6% and the residual functionality drops to 64.5% during an event with $T_w = 13.5$ sec. For $T_w = 12.6$ sec, the resiliency drops to 81.3% with a residual functionality of 54.5%. On the other hand, at $T_w = 12$ sec, the resilience index drops to 72.7%. As a general trend, it is observed that, the residual functionality and consequently the resiliency of the bridge decreased for smaller wave periods signifying that the lower wave periods will require greater efforts to recover the bridge into its target functionality. Figure 5-11(l) reveals that for the lowest value of T_w considered in this study (3.37 sec) the resiliency is the lowest at 36.2% with 0% residual functionality. According to the ranking scale provided in the paper by Minaie and Moon (2017) (Table 5-3), for $T_w = 3.37$ seconds, the bridge falls in the extremely low resilience class. Conversely, the bridge can be classified into a high resilience group when the wave periods are between 12.6 to 13.5 seconds. In comparison, the resiliency for the same wave periods as shown in Figure 5-11 are found to be reduced for the scenario 2. In Figure 5-12, the resiliency is dropped to 80.3% with a residual functionality of 49%. The residual functionality and corresponding resiliency dropped to 37.1% and 72.1%, respectively at $T_w = 12.6$ seconds. As mentioned in earlier sections, the scenario 2 is evidently more severe and therefore the bridge is less resilient when the piers are completely submerged compared to scenario 1.

Figure 5-13 presents the variation in resiliency and functionality of the bridge with respect to H_w during scenario 1. With increasing wave heights, the resiliency is reduced, for instance, at $H_w = 2$ m the residual functionality is at 79% and a corresponding resiliency of 93% (Figure 5-13a). From Figure 5-13(b) it can be seen that the indices are reduced when H_w is 4.64m (31.87% residual functionality and 79% resiliency). Moreover, at $H_w = 5.43$ m the resiliency of the bridge is observed to be 58.9%. These results can be compared with those obtained in the study by Li et al. (2020), where the limit states were based on deck uplift capacity and a linear simplified method of recovery function were utilized for resiliency analysis. At wave heights of 4.60m and 5.35m, the resiliencies

obtained for the case study bridge was 92% and 64.7%, respectively (Li et al. 2020). The difference in results are comparable. As the method used for resilience analysis was a simplified one with the use of linear recovery functions in the study by Li et al. (2020), it is prone to give less accurate results compared to the more precise recovery functions and corresponding parameters adopted in this study.

The resilience indices obtained during the scenario 2 analysis are presented in Figure 5-14. Once again it is observed that the impact of increasing wave heights is higher when the piers are completely inundated. The mean residual functionality at 4.64m wave height is 0.32 for scenario 1 whereas that observed in scenario 2 is reduced to 0.15 indicating that the bridge will require more resources and longer time to bounce back to its target functionality. Figure 5-15 illustrates the variation in resiliency and functionality with increasing levels of still water depth for scenario 1. The resiliency decreases from 98.6% to 49.5% when still water depth increased from 7.2m to 12m, respectively. Figures 5-16 (a) and (b) show the variation in mean resiliency with respect to the IMs considered in this study for scenarios 1 and 2, respectively. It can be seen that, at 12.6 second wave period, the bridge is in the high resiliency class in scenario 1, whereas it is in the moderate resiliency class in scenario 2 loading. On the other hand, the bridge is in extremely low resilient group at 3.37 seconds wave period in scenario 2. The bottom most ranking in resiliency due to the variations in wave height is found to be low at $H_w = 5.43\text{m}$ for both the scenarios. The bridge is seen to be in the same resilient group irrespective of the changes in wave height in both scenarios except at 2m wave height where the bridge is in the very high resiliency class in scenario 1 compared to being in the high resiliency class during scenario 2.

Table 5-3 Resilient ranking scale (Minaie and Moon 2017)

Resilience Class	Resilience Value range
Very high	91-100
High	81-90
Moderate	61-80
Low	41-60
Extremely low	21-40
Non-resilient	0-20

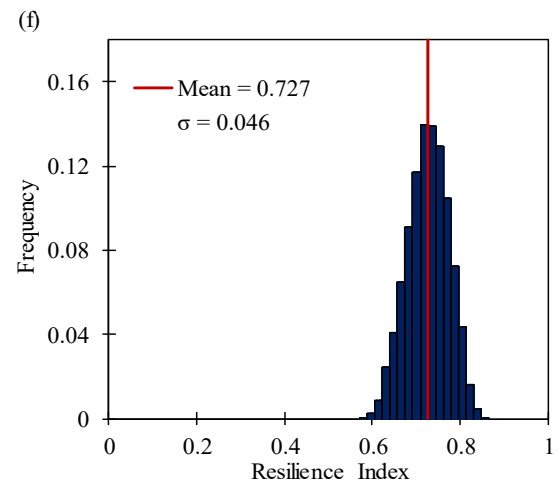
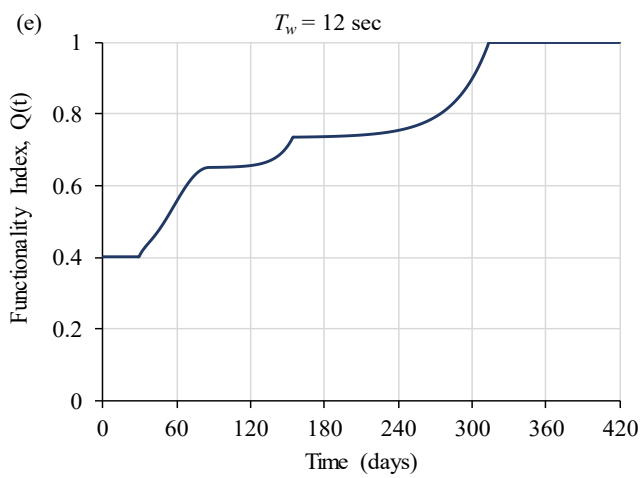
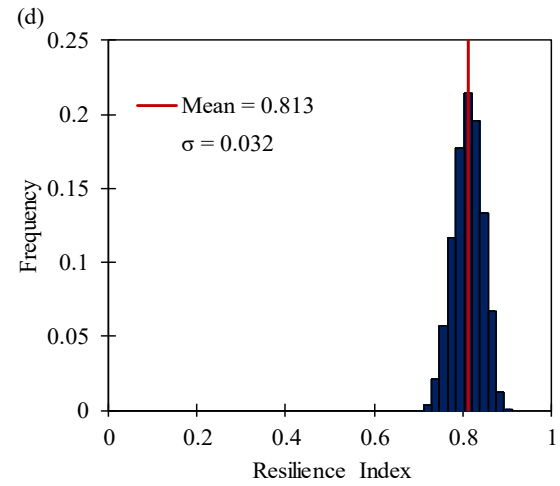
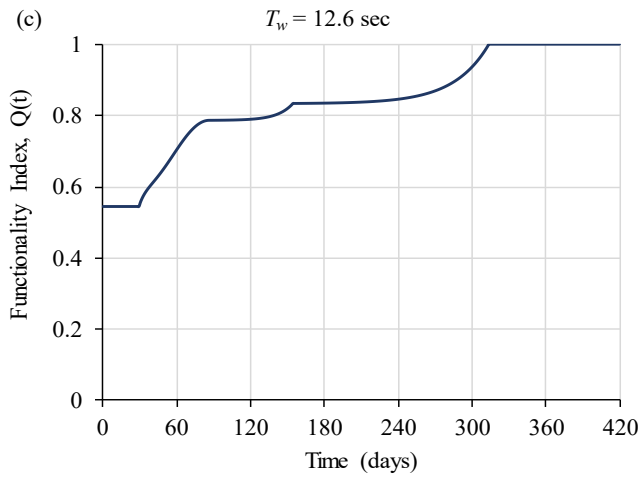
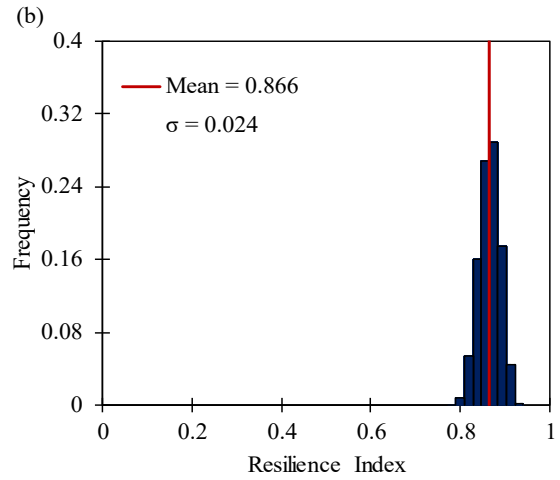
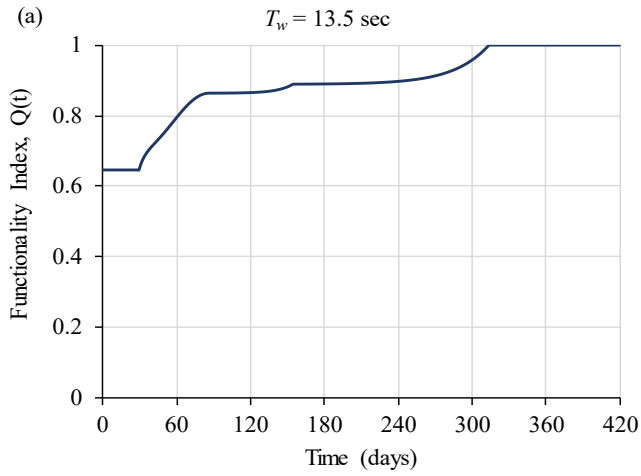


Figure 5-11 Functionality index and variation in resilience index due to wave periods at (a and b) 13.5 sec, (c and d) 12.6 sec, (e and f) 12 sec of scenario 1.

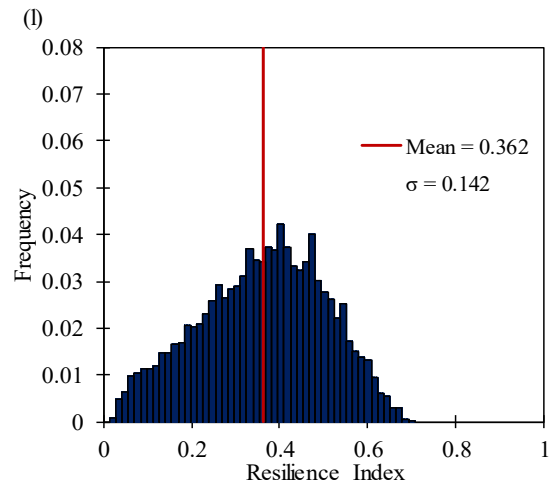
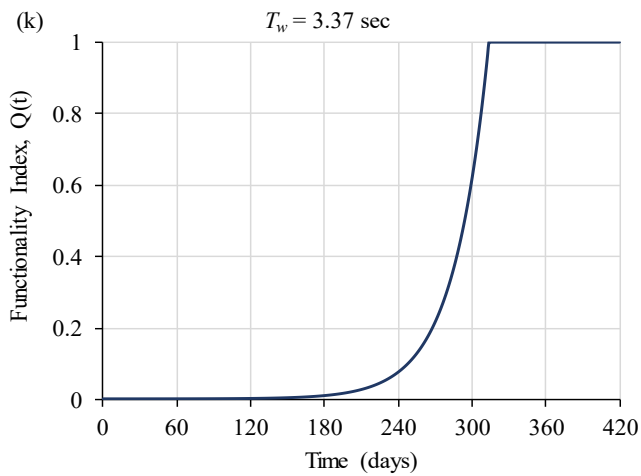
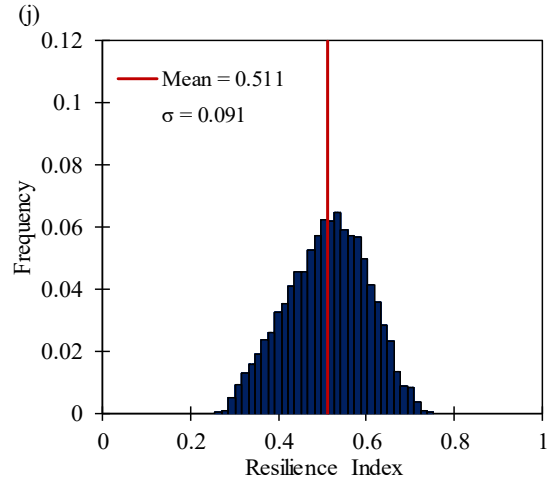
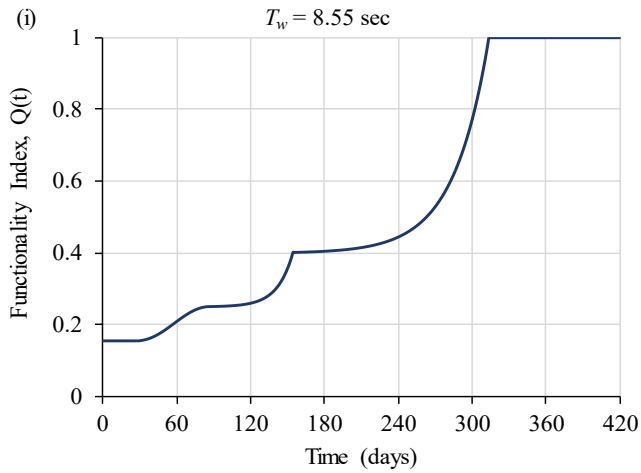
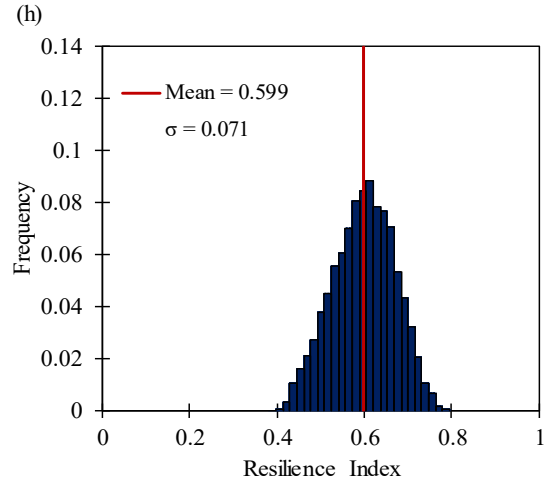
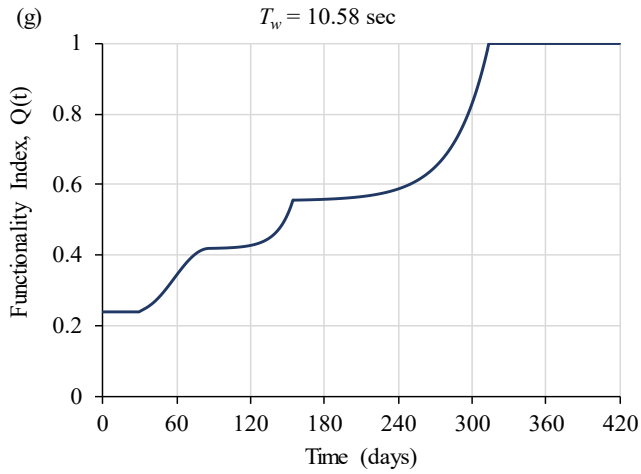


Figure 5-11 Functionality index and variation in resilience index due to wave periods at (g and h) 10.58 sec, (i and j) 8.55 sec, (k and l) 3.37 sec of scenario 1.

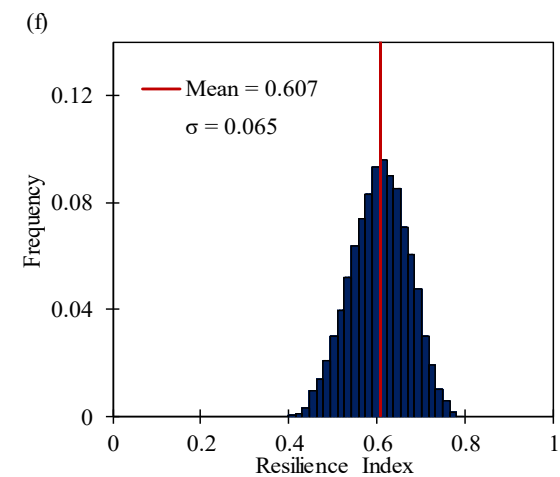
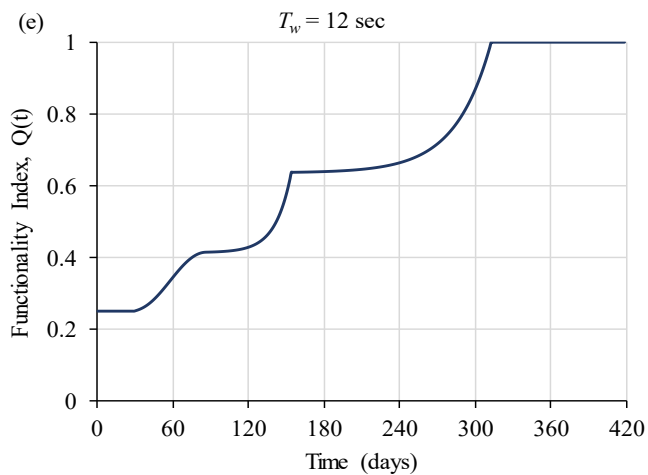
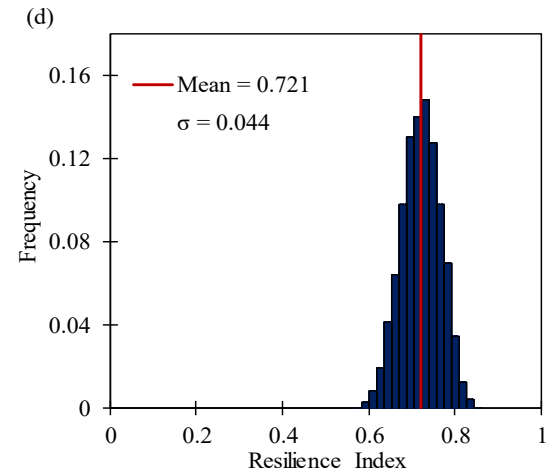
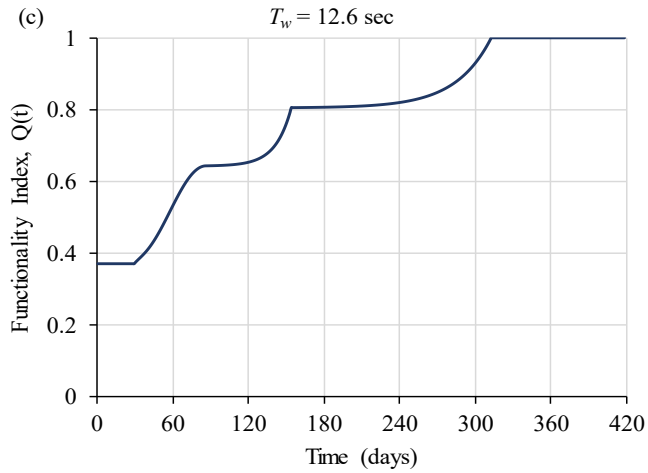
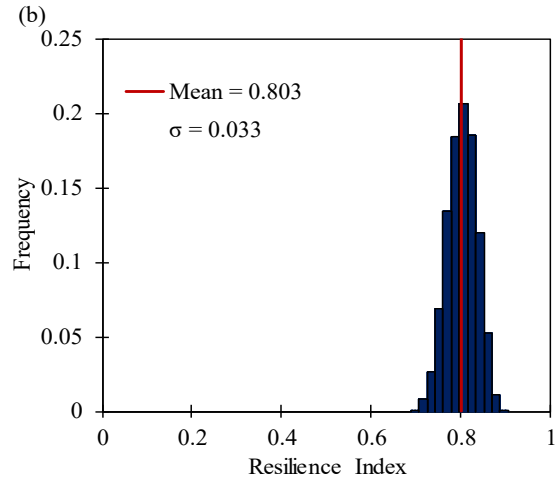
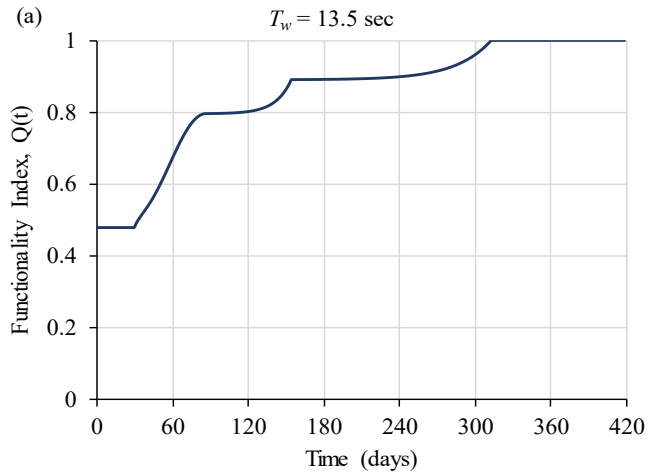


Figure 5-12 Functionality index and variation in resilience index due to wave periods at (a and b) 13.5 sec, (c and d) 12.6 sec, (e and f) 12 sec of scenario 2.

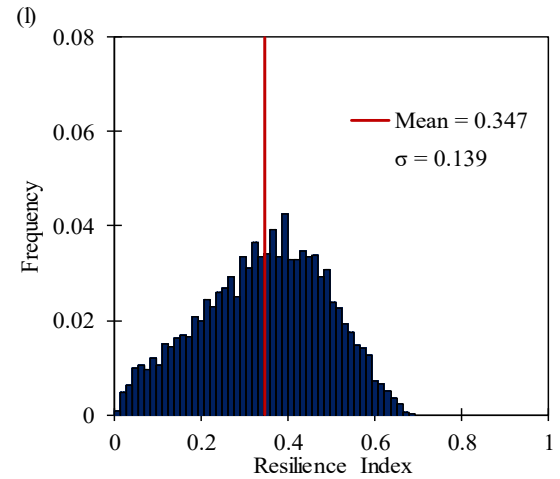
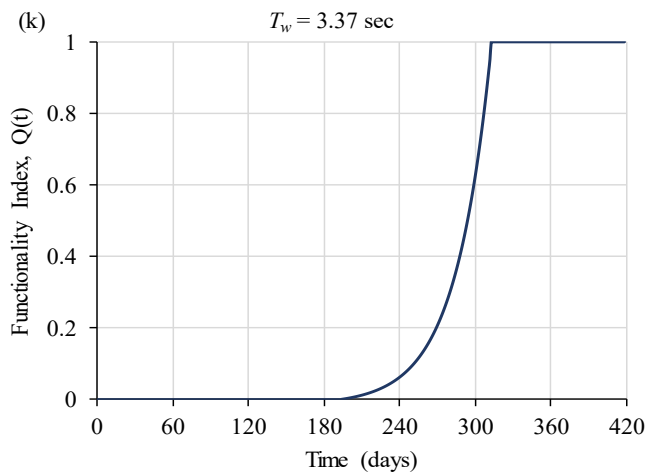
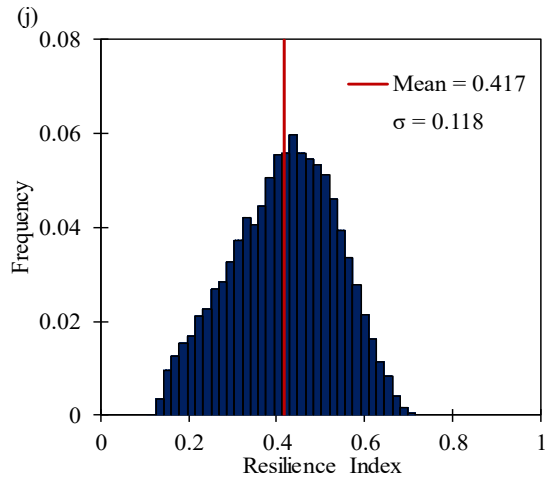
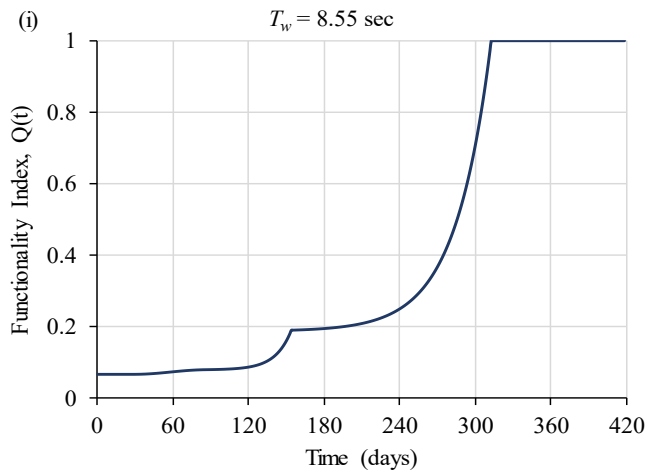
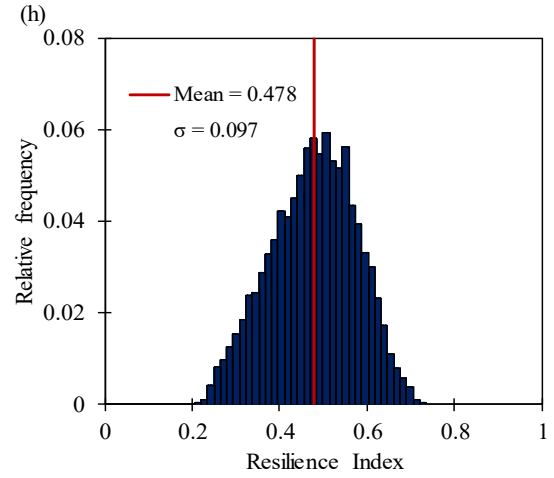
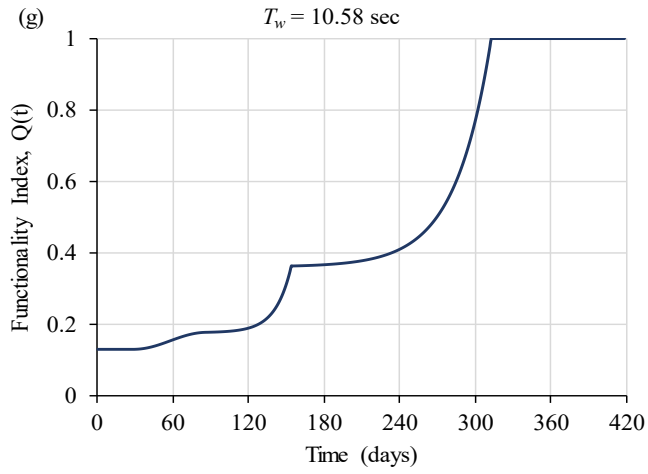


Figure 5-12 Functionality index and variation in resilience index due to wave periods at (g and h) 10.58 sec, (i and j) 8.55 sec, (k and l) 3.37 sec of scenario 2.

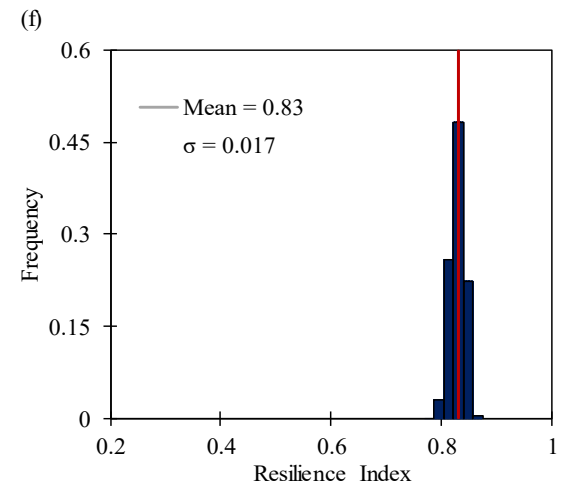
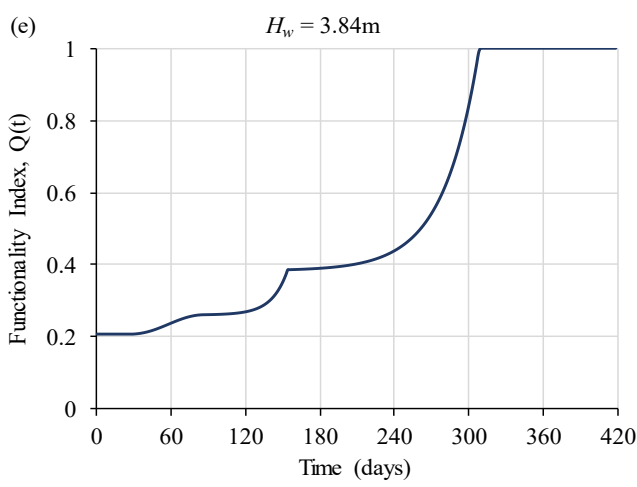
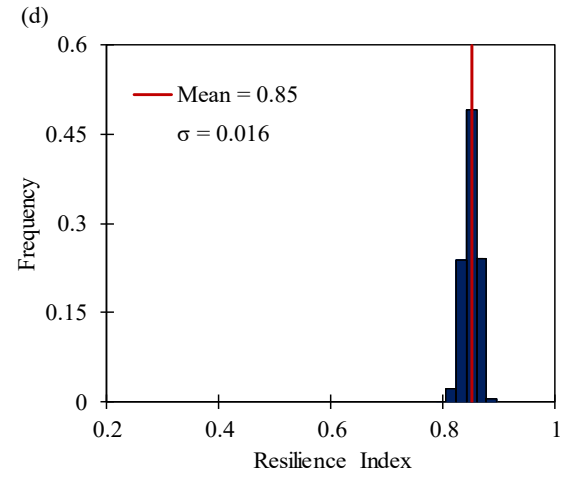
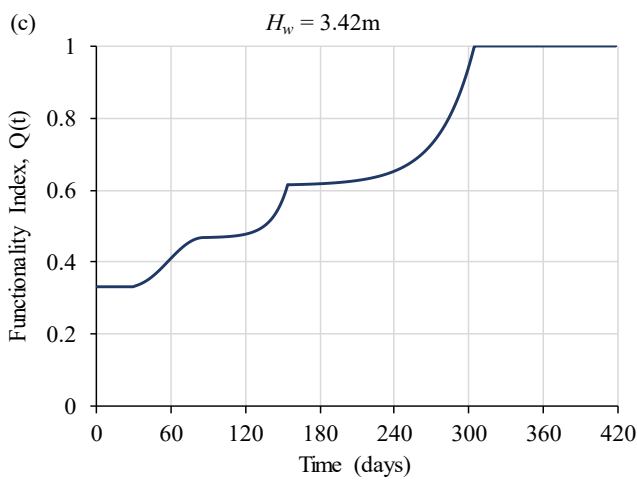
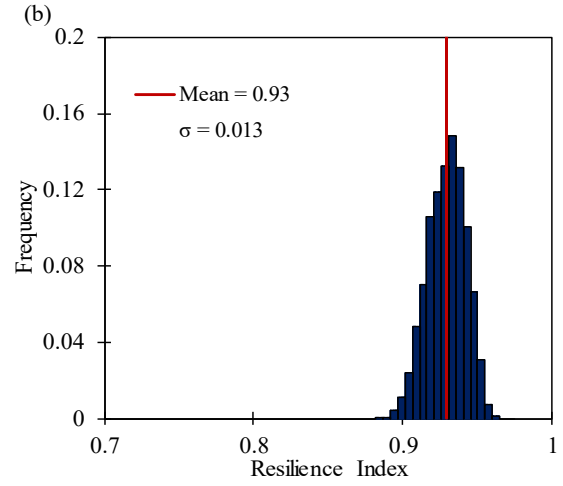
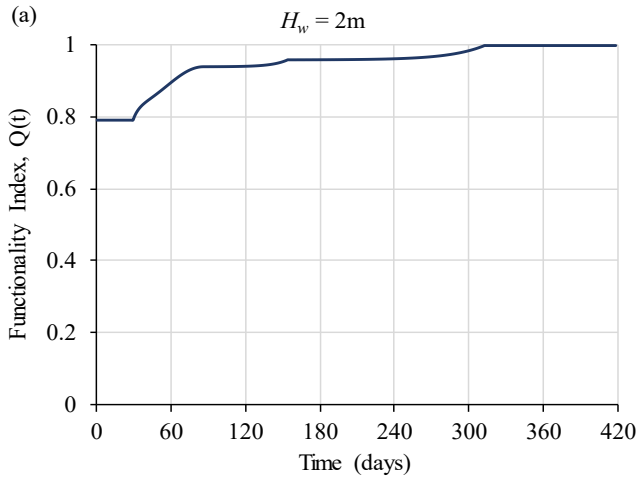


Figure 5-13 Functionality index and variation in resilience index due to wave heights at (a and b) 2m, (c and d) 3.42m, (e and f) 3.84m of scenario 1

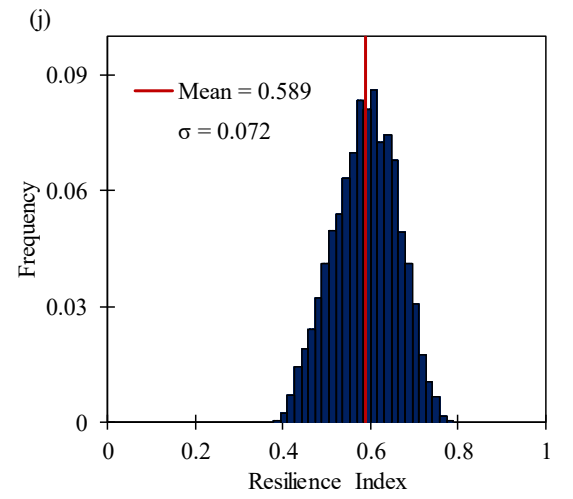
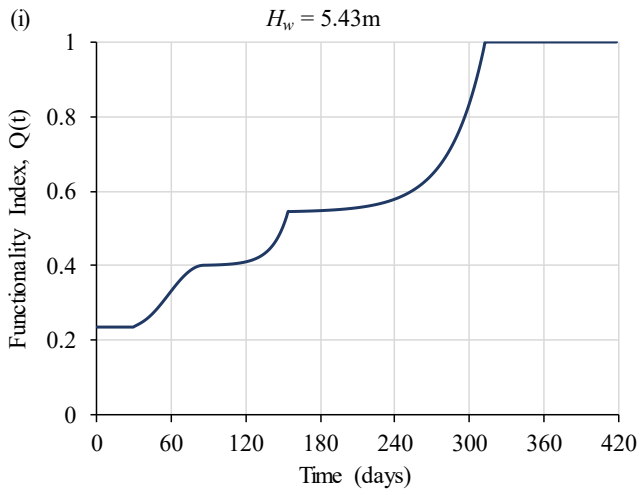
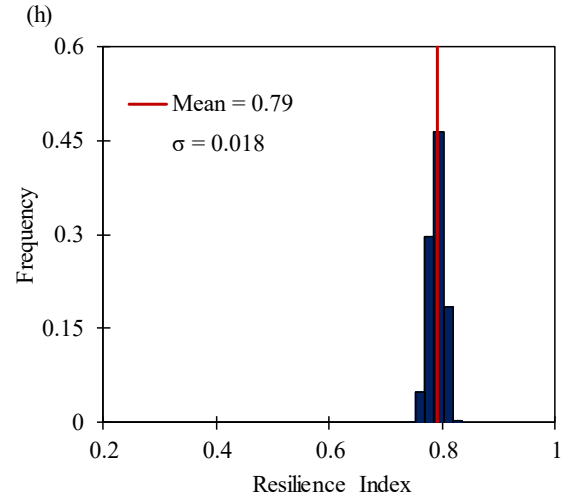
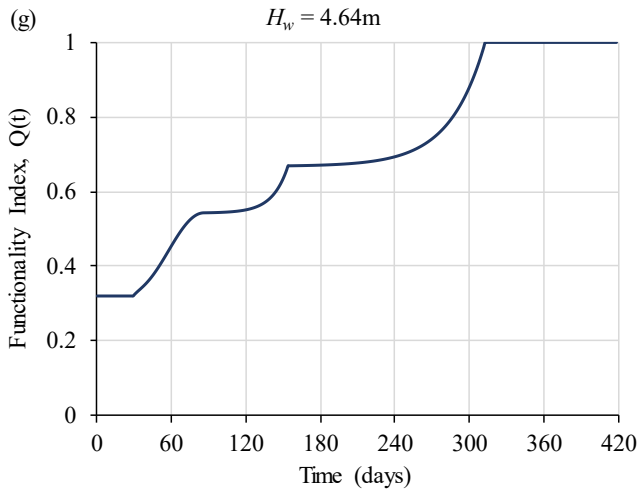


Figure 5-13 Functionality index and variation in resilience index due to wave heights at (g and h) 4.64m, (i and j) 5.43m of scenario 1.

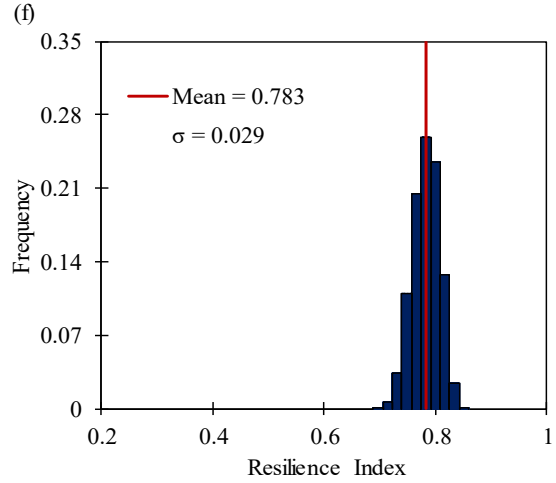
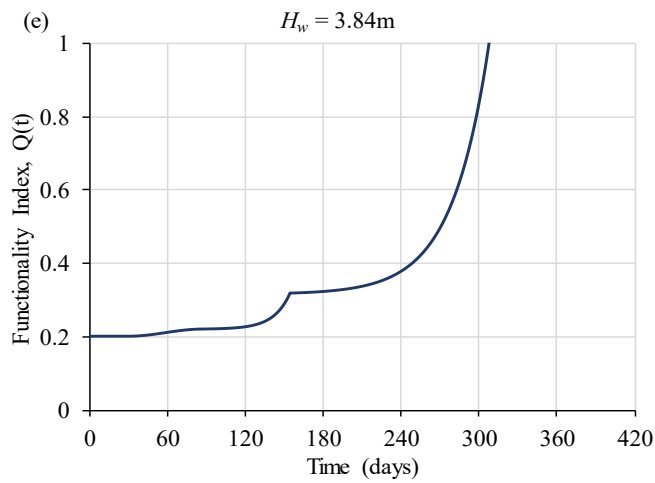
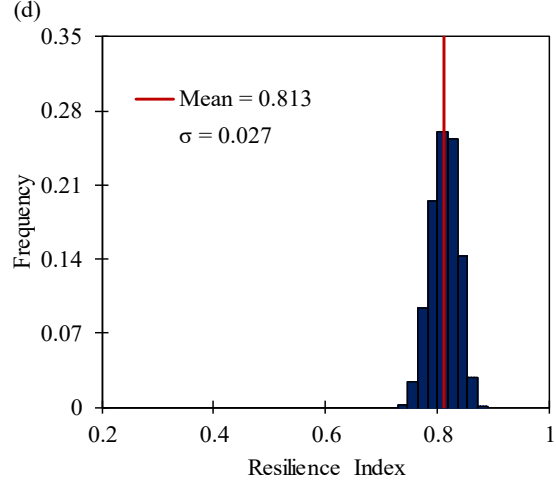
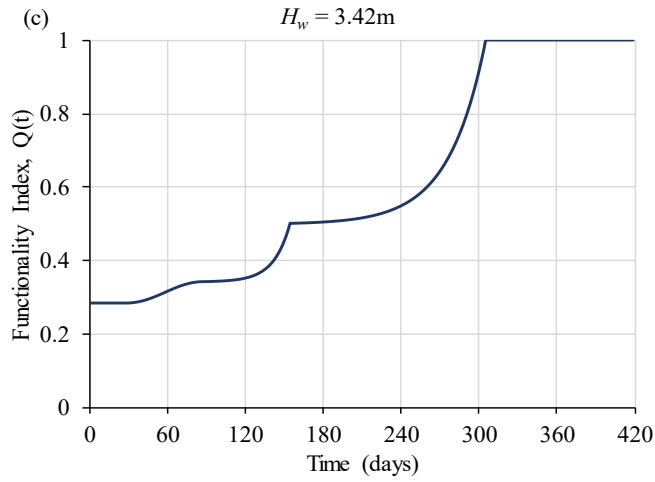
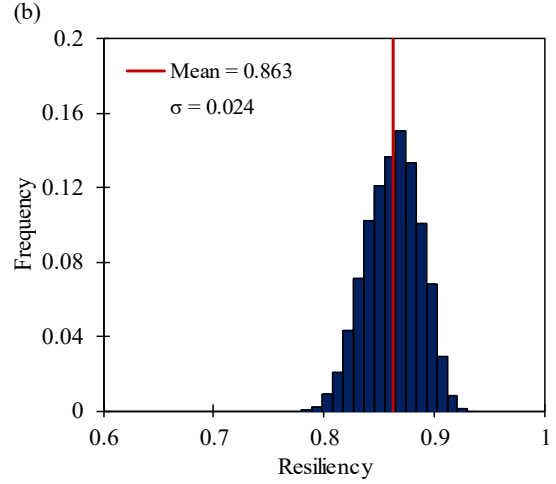
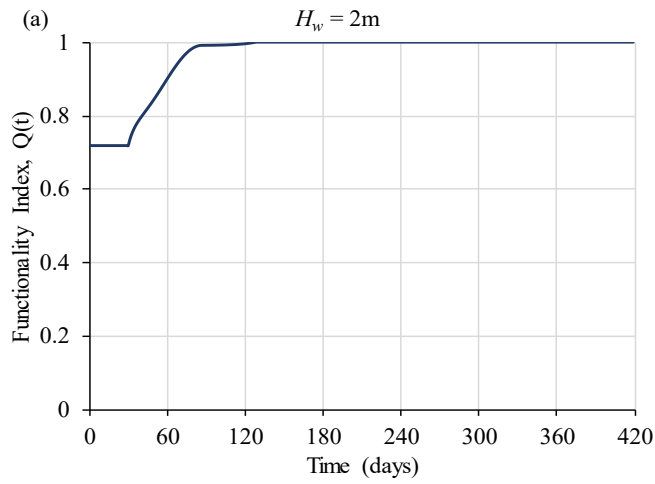


Figure 5-14 Functionality index and variation in resilience index due to wave heights at (a and b) 2m, (c and d) 3.42m, (e and f) 3.84m of scenario 2.

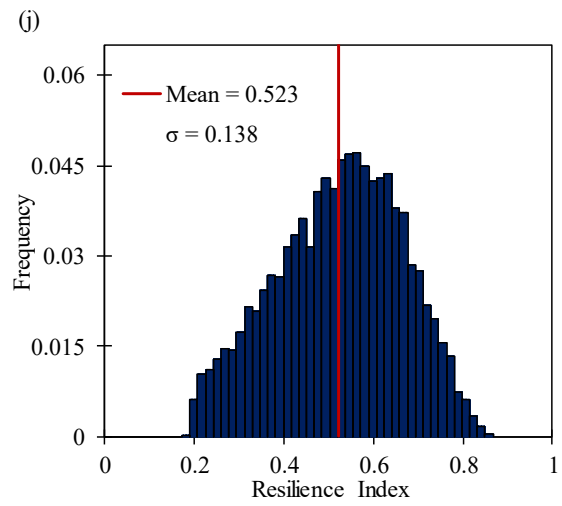
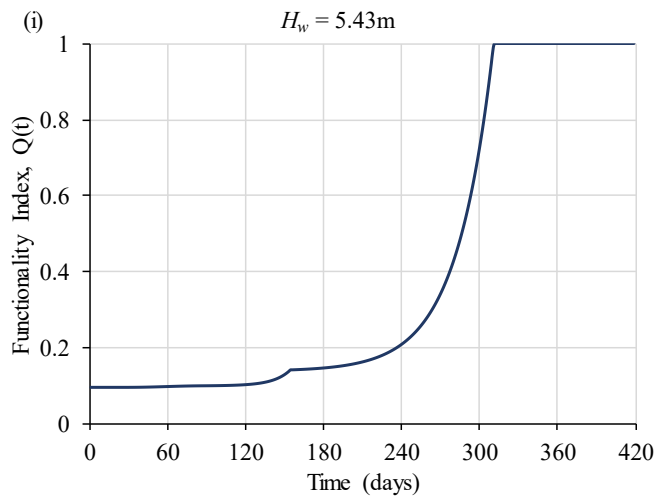
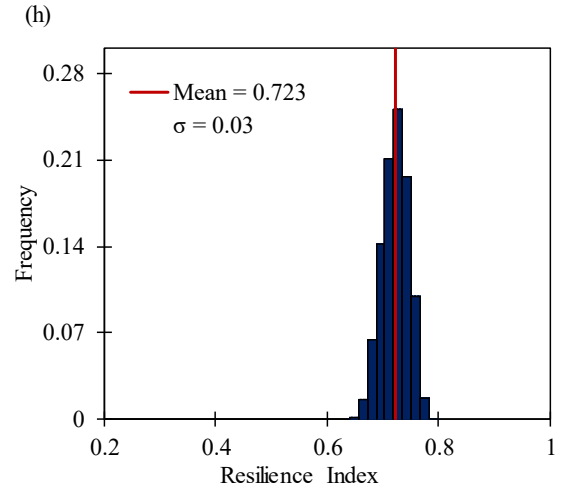
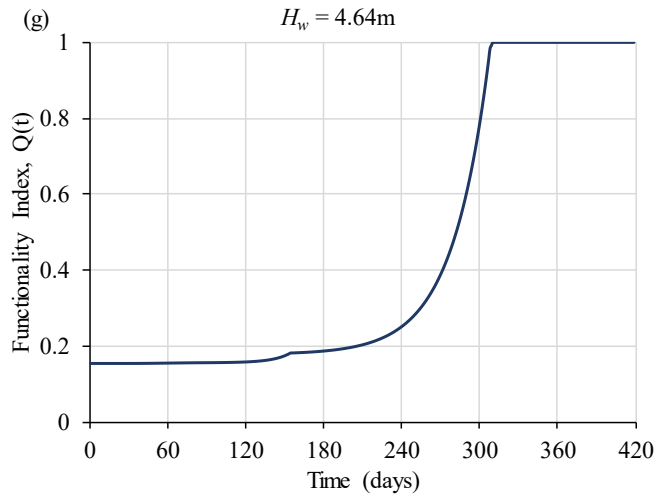


Figure 5-14 Functionality index and variation in resilience index due to wave heights at (g and h) 4.64m, (i and j) 5.43m of scenario 2.

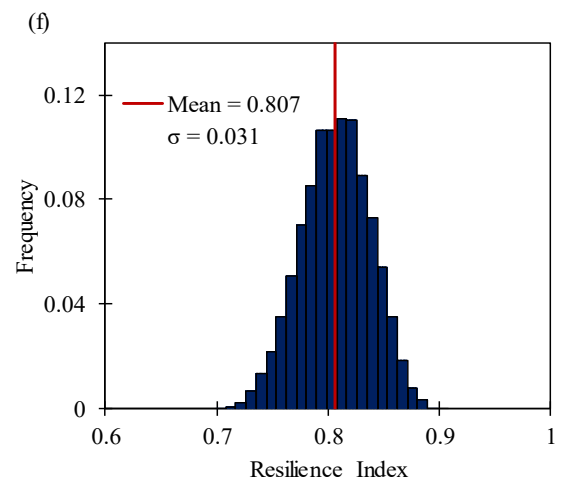
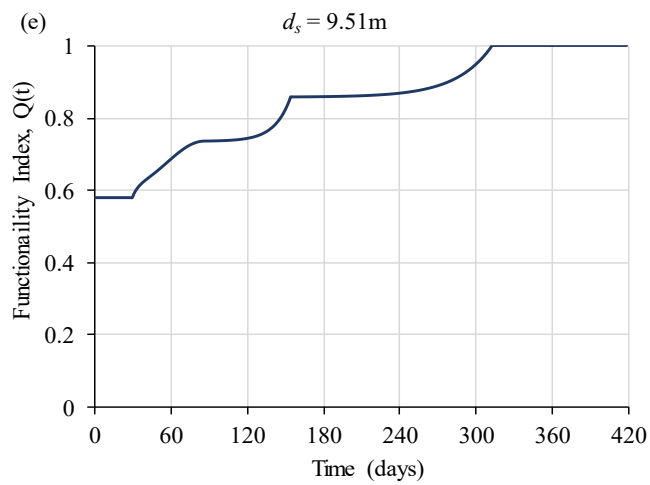
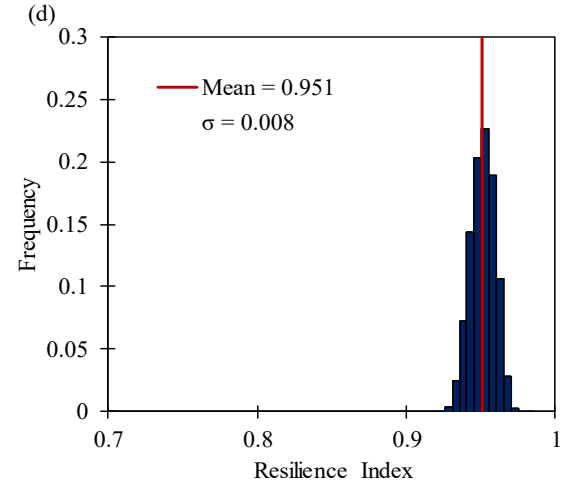
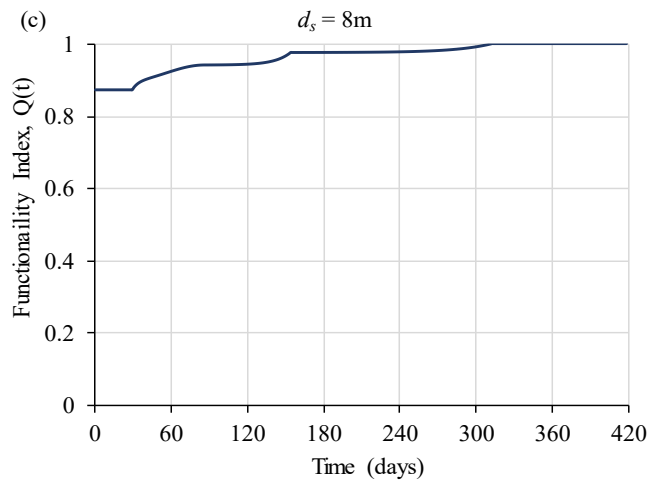
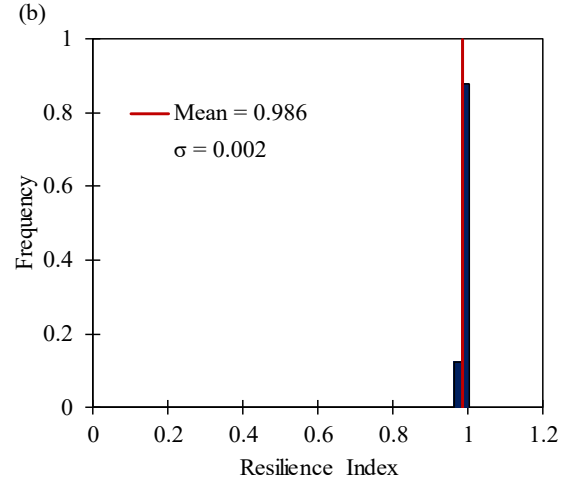
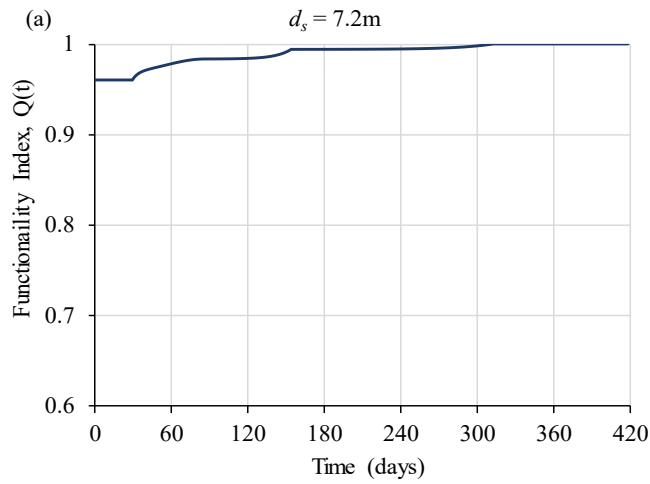


Figure 5-15 Functionality index and variation in resilience index due to still water depths at (a and b) 7.2m, (c and d) 8m, (e and f) 9.51m of scenario 1.

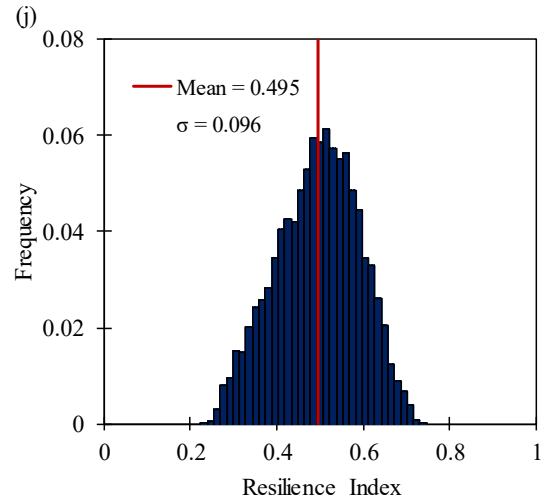
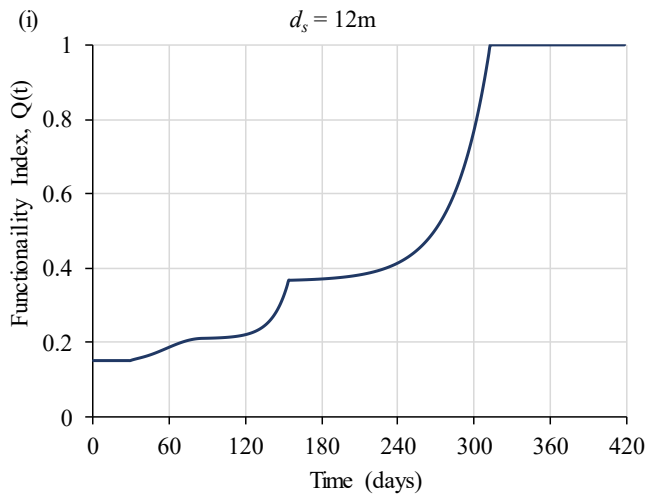
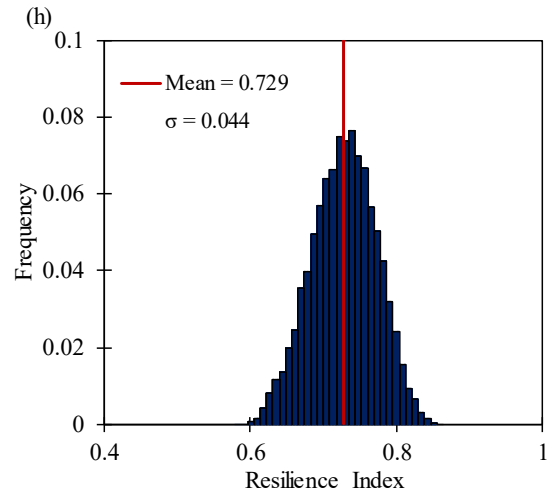
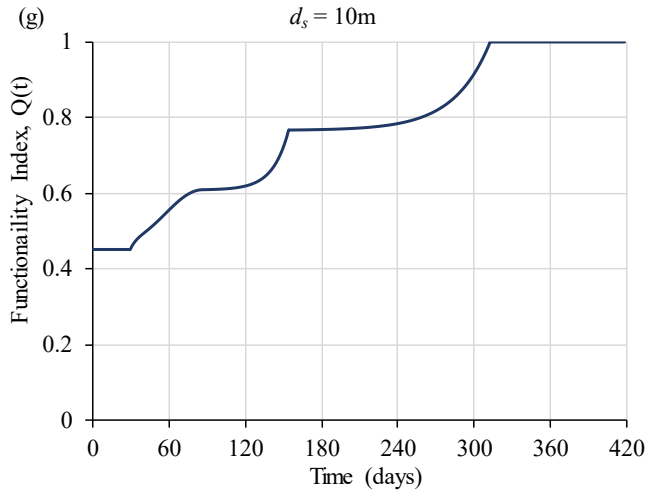


Figure 5-15 Functionality index and variation in resilience index due to still water depths at (g and h) 10m, (i and j) 12m of scenario 1.

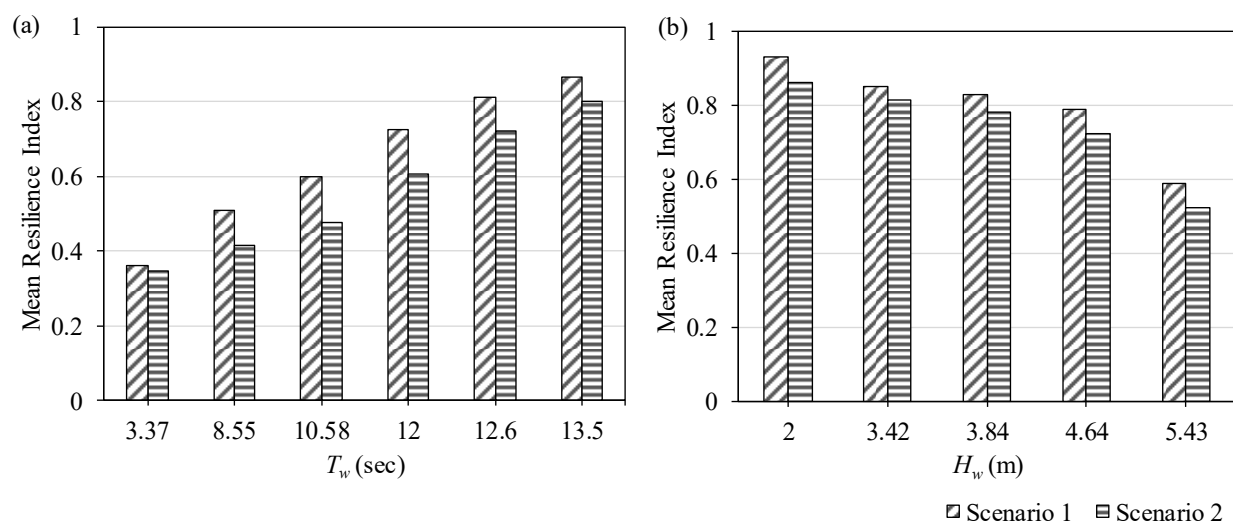


Figure 5-16 Variation in mean resilience index corresponding to (a) T_w and (b) H_w

5.5 Summary

This chapter presents the fragility curves and resiliency assessment of the case study coastal bridges under extreme wave load combinations. Multiple stripe analysis technique is adopted to fit the fragility curves with the use of maximum likelihood function to derive the fitting parameters. Results from the fragility analysis show that the failure probability of the elastomeric bearing is higher compared to the other components studied in both the scenarios. Moreover, the shear keys experience higher damage beyond a certain intensity measure compared to the other components. This reveals that the failure probability of bearings and shear keys due to extreme waves are higher irrespective of the scenario considered. Mean resilience indices are computed from a number of iterations in order to obtain results with 95% confidence level. It is seen that as the hazard intensity increased, the variation in resilience indices obtained from the iterations also increased. Using the value of mean resilience index corresponding to a level of hazard intensity, the bridge can also be classified according to a resilience rank. Results reveal that there is a variation in resiliency class while comparing between the two scenarios considering T_w as IM whereas the bridge system is observed to be in the same class for both scenarios taking H_w as the IM.

Chapter 6 Conclusions and Future Works

6.1 Summary

In order to address the growing concerns of coastal bridge resiliency towards extreme wave loads originating from hurricanes, tsunamis and storm surges, quantification of the damages posed by these hazards is required. Current design standards including the Canadian Highway Bridge Design Code provide empirical formulas to accommodate the water and wave action loading on the structures but fail to include the provisions for the dynamic nature of wave-induced loads which are typically more devastating. Moreover, from the extensive literature review, it is observed that most of the vulnerability analysis of bridge systems is correlated to the failures that occur in the superstructure and very little attention is given to the strain-based damages in the substructure components. To help bridge these gaps, this thesis focused on the vulnerability and resiliency assessment of coastal bridges under the action of extreme waves considering the behaviour of both superstructure (bridge deck) and substructure (piers) as well as the connection elements (elastomeric bearings and shear keys).

6.2 Core Contributions

The results of this study are expected to enhance the current knowledge of bridge failure mechanisms during extreme wave induced hazards. Moreover, the outcomes can help to modify the design practices to consider the dynamic nature of wave actions. The contributions of this research are:

- Identification of the most influential wave parameter affecting the magnitude and intensity of the wave loads.
- Identification of the most vulnerable component of the bridge system for a particular level of hazard intensity.
- Development of a simplified method of resiliency assessment and classification of the bridge corresponding to its resilience rank.

6.3 Conclusions

6.3.1 Literature Review

- Most studies include superstructure behaviour under the action of extreme wave-induced loads and little attention is paid to the substructure vulnerability assessments, especially the piers.
- Current design methods only deal with the quasi-static/hydrodynamic loads and not the impact force as well as the time-varying loading nature of the waves. Empirical formulas are developed based on limited connectivity between superstructure and substructure. Moreover, the application of these formulas is limited to certain hazard parameters and site conditions. A simplified method to account for a wider range of hazard intensity is required as the frequency and intensity of extreme waves are increasing as a result of global warming.
- Fragility assessments of coastal bridges are done using wave heights, and surge/inundation depth as intensity measures so far. The vulnerability of systems due to wave period is yet to be analyzed.
- The existing resilience assessment analysis results of coastal bridges under extreme waves can be improved by incorporating more accurate assumptions of the recovery patterns. Further advancement is needed to include wider variations in hazard intensity and recovery elements.

6.3.2 Wave Load Calculation Method

This study is performed considering two scenarios, one is where the waves reach only the piers and so only horizontal wave forces are applied on the piers. The second scenario depicts the case when the waves inundate the substructure completely and hit the deck and so both vertical and horizontal wave forces are applied to the deck including the horizontal forces on piers. Wave particle velocity and acceleration time history are first determined through the linear wave theory which creates sinusoidal wave profile. The dispersion theory is used to compute the wavelength from the known hazard parameters (i.e. wave period). The quasi-static force component is generated using time period equal to wave period whereas that of the slamming force is generated using $5/8^{\text{th}}$ of the wave period. The following points are highlighted as conclusions:

- This method of wave load calculation is verified against experimental studies where the difference with numerical results is within 10%.
- Magnitude of the total vertical force time history is higher than that of the horizontal component for the same wave load parameters.
- Similar to the observations in the available literature, three distinct peaks are seen within each wave period in both the horizontal and vertical wave force time histories generated for the case study bridge superstructure having three I-girders.

6.3.3 Variation in Component Demands and The Most Affecting Wave Parameter

A total of 100 sets of wave parameter combinations are generated using the Latin Hypercube sampling technique for each wave loading scenario. The same technique is used to generate different combinations of bridge material parameters to model a total of 20 case study bridges in the finite element software OpenSees. Guidelines from the CHBDC (CSA S6:19) is followed to generate the total wave force time histories in both directions. Each of these models are applied with the 100 wave force time history generated in the two scenarios giving 4000 simulation results to analyze in MATLAB. Based on the engineering demand parameters chosen (pier drift, deck transverse displacement, elastomeric bearing and shear key displacements), the responses of the components are recorded and analyzed to identify the most influential wave parameter. Based on the analysis results, the following conclusions are drawn:

- The component responses increased with increase in wave height and still water depth in both horizontal and vertical directions. This identifies the fact that the wave load intensity increased with an increase in wave height and still water depth.
- Similarly, from the component responses, it is noted that the wave-induced loads increased with decreasing wave periods. For instance, it is observed that the pier drift as well as displacement of the deck and connecting elements increased with decreasing wave periods for the same still water depth. Also, the wave load intensity increased with decreasing wave period even though the wave height decreased for the same still water depth. This identified that wave period is the most influential parameter affecting the wave load intensity.
- Upon comparing the material parameters, it is observed that piers with higher concrete compressive strength showed higher spalling and crushing drifts. Similarly, piers with

reinforcement of greater yield strength exhibited higher yielding and buckling drift capacities.

- Upon comparing both the scenarios, the component responses were observed to be higher for scenario 2. This signifies that the intensity of wave loads in scenario 2 is higher where the still water depth is the largest among the combinations analyzed.

6.3.4 Damage State Definitions

Four damage states are adopted for each of the components considered in the response analyses. The elastomeric bearing damage states are chosen based on seismic load analysis in available literature as no damage states are developed to this date using shear deformation of bearings as the engineering demand parameter under extreme wave forces. Shear key damage states are selected based on the deformation pertaining to the stages of visible material damage during wave loading. Deck transverse displacement damage states are selected at the same displacement levels as defined in the shear key damage states because it is assumed that as the transverse movement of the deck is restrained using shear keys, the deck will begin to fail as soon as the shear key does. Strain-based damage detection method is followed to derive the limiting drift values corresponding to yielding of longitudinal reinforcement, spalling of cover concrete, crushing of core concrete and buckling of longitudinal reinforcement in order to define the damage states of the piers. The Kolmogorov-Smirnov test is used to determine the most suitable distribution of the drift values obtained in each damage state. The calculated median from the distributions are then termed as the limiting drift values for the corresponding damage states. The following conclusions can be drawn from the pier-drift based damage state definition:

- The median drifts computed show that the yielding damage state is crossed when the drift is at 0.91% and 2.34% for scenarios 1 and 2, respectively.
- Similarly, the spalling damage state is exceeded at 1.48% and 3.61% pier drifts for scenarios 1 and 2, respectively.
- As the severity of damage increased the difference in limiting drifts between scenarios 1 and 2 decreased. For instance, the difference in drift corresponding to spalling damage state between scenarios 1 and 2 is 59% whereas that corresponding to the crushing damage state is only 18%.

- The limiting drifts corresponding to the four damage states adopted for piers obtained in scenario 2 are delayed compared to those obtained in scenario 1 due to the axial tensile forces arising from the deck uplift by the waves thus altering the material responses in the piers.

6.3.5 Fragility Curve Analysis

The damage states defined are used to develop fragility curves which pave the way for resilience assessment and consequently will help in devising retrofit technologies. As 20 bridges are analyzed for each combination of wave parameters, there are 20 different fragility data for each of the 100 IMs considered in this study. Therefore, it is difficult to note an increasing trend in the component responses exceeding particular damage with increasing IM. The MSA is best suited for this type of data and so it is adopted to fit the fragility curves using the method of maximum likelihood estimation. The following points from the analysis of fragility curves are highlighted as the main conclusions:

- It is observed that the failure probability of piers during scenario 2 is higher compared to scenario 1 even though the limiting drift values in all the damage states are delayed.
- The failure probability of the elastomeric bearing is higher compared to the other components studied. Moreover, the shear keys experience higher damage beyond a certain intensity measure compared to the other components. This reveals that the failure probability of bearings and shear keys due to extreme waves is higher.
- Similar to the component-level fragility curves, the system fragility is also higher during scenario 2 loading. Moreover, the most vulnerable components during scenario 1 were found to be the bearings and shear keys followed by the deck. On the other hand, the piers are identified to be the most vulnerable followed by the elastomeric bearings, during scenario 2.

6.3.6 Resilience Assessment Results

Recovery strategies are selected based on previous studies of coastal bridges under seismic loads and post-hazard survey data available in literature. 10,000 samples of recovery function parameters are generated using Latin Hypercube sampling. The functionality curve is generated corresponding to each of the recovery functions considered. The resilience index is computed for each recovery strategy and the mean resilience index is calculated. The bridges are then classified into ranks

corresponding to the indices obtained. Based on the results of the resiliency analysis the following points are concluded:

- As indicated by the standard deviations corresponding to each IM analyzed, the variations in sample resiliencies increased with increasing IMs.
- The residual functionality and thereby resilience of the bridge decreased with an increase in hazard intensity. With the lowest wave period of 3.37 seconds, the bridge resiliency drops to 36% with no residual functionality. This resiliency decreased to 34.7% with zero residual functionality in scenario 2.
- At 4.64m wave height, the mean residual functionality under scenario 2 loading is about half of that observed in scenario 1 loading indicating that the bridge will require more resources and a longer time to bounce back to its target functionality when the substructure is completely inundated.
- At 3.37 sec wave period, the bridge is identified to be in the “extremely low” resilient group during both wave loading scenarios. The bottom most ranking due to the variations in wave height is found to be “low” at 5.43m wave height for both scenarios. Also, the bridge is seen to be in the same resilient group irrespective of the changes in wave height in both scenarios except at 2m wave height where the bridge is in the “very high resiliency” class in scenario 1 compared to being in the “high resiliency” class during scenario 2.

6.4 Recommendation for Future Studies

The following recommendations are proposed for future studies:

- This study considered one type of pier cross-section for the development of performance-based damage states and subsequent fragility assessment. Future studies are necessary to investigate various types and geometric properties of piers to evaluate the resiliency of the bridge systems due to extreme waves.
- Corrosion is very common in coastal regions which is aggravated due to the increasing temperature and humidity as a result of climate change. The detrimental effect of chloride-induced and carbonation-induced corrosion on the resiliency of the piers and the system towards extreme waves needs to be analyzed.
- Future studies are also expected to include the effects of variation in superstructure and substructure connection types (i.e. LRB, elastomer bearing, steel laminated elastomeric

bearings, PTFE sliding bearings) on the fragility probability of the bridge system due to extreme waves.

- Recent applications for surrogate modeling are observed in earthquake engineering and design whereas its ability to provide accurate fragility models for bridges under extreme wave loads is yet to be analyzed. Future studies can include the application of surrogate modeling techniques to generate fragility surfaces of bridge systems under a combination of two or more intensity parameters.

References

- AASHTO (American Association of State Highway and Transportation Official). 2008. Guide Specifications for Bridges Vulnerable to Coastal Storms. Association of State Highway and Transportation Officials. Washington D.C.
- Aguíñiga, F., K. Matakis, H. Estrada, J. Sai, P. Leelani and J. Shelden. 2008. *Report synthesis of wave load design methods for coastal bridges*. Report No. FHWA/TX-08/0-5516. 2. Texas A&M University. Kingsville, Texas.
- Akiyama, M., D. M. Frangopol, M. Arai and S. Koshimura. 2013. "Reliability of bridges under tsunami hazards: Emphasis on the 2011 Tohoku-oki earthquake." *Earthquake Spectra* **29**(1_suppl): 295-314.
- Alam, M. S., A. R. Barbosa, M. H. Scott, D. T. Cox and J. W. van de Lindt. 2018. "Development of physics-based tsunami fragility functions considering structural member failures." *Journal of Structural Engineering* **144**(3): 04017221.
- Argyroudis, S. A., S. A. Mitoulis, L. Hofer, M. A. Zanini, E. Tubaldi and D. M. Frangopol. 2020. "Resilience assessment framework for critical infrastructure in a multi-hazard environment: Case study on transport assets." *Science of the Total Environment* **714**: 136854.
- ASCE 7-16. 2016. Minimum design loads for buildings and other structures. American Society for Civil Engineers. Reston, VA.
- Ataei, N. 2013. Vulnerability assessment of coastal bridges subjected to hurricane events, Ph.D. Thesis, Rice University, Houston, Texas.
- Ataei, N. and J. E. Padgett. 2013. "Limit state capacities for global performance assessment of bridges exposed to hurricane surge and wave." *Structural Safety* **41**: 73-81.
- Ataei, N. and J. E. Padgett. 2013. "Probabilistic modeling of bridge deck unseating during hurricane events." *Journal of Bridge Engineering* **18**(4): 275-286.
- Ataei, N. and J. E. Padgett. 2015. "Fragility surrogate models for coastal bridges in hurricane prone zones." *Engineering Structures* **103**: 203-213.
- Ataei, N. and J. E. Padgett. 2015. "Influential fluid–structure interaction modelling parameters on the response of bridges vulnerable to coastal storms." *Structure and Infrastructure Engineering* **11**(3): 321-333.

- Ataei, N., M. Stearns and J. E. Padgett. 2010. "Response sensitivity for probabilistic damage assessment of coastal bridges under surge and wave loading." *Transportation Research Record* **2202**(1): 93-101.
- Attary, N., J. W. van de Lindt, V. U. Unnikrishnan, A. R. Barbosa and D. T. Cox. 2017. "Methodology for development of physics-based tsunami fragilities." *Journal of Structural Engineering* **143**(5): 04016223.
- Azadbakht, M. and S. C. Yim. 2015. "Simulation and estimation of tsunami loads on bridge superstructures." *Journal of Waterway, Port, Coastal, and Ocean Engineering* **141**(2): 04014031.
- Azadbakht, M. and S. C. Yim. 2016. "Effect of trapped air on wave forces on coastal bridge superstructures." *Journal of Ocean Engineering and Marine Energy* **2**(2): 139-158.
- Baarholm, R. and O. M. Faltinsen. 2004. "Wave impact underneath horizontal decks." *Journal of Marine Science and Technology* **9**(1): 1-13.
- Badroddin, M. and Z. Chen. 2021. "Lifetime resilience measurement of river-crossing bridges with scour countermeasures under multiple hazards." *Journal of Engineering Mechanics* **147**(9): 04021058.
- Baker, J. W. 2015. "Efficient analytical fragility function fitting using dynamic structural analysis." *Earthquake Spectra* **31**(1): 579-599.
- Balomenos, G.P. and J. E. Padgett. 2018. "Effects of wave loading conditions on the fragility of pile-supported wharves/piers." *Coastal Engineering Proceedings* (36): 29-29
- Balomenos, G. P. and J. E. Padgett. 2018. "Fragility analysis of pile-supported wharves and piers exposed to storm surge and waves." *Journal of Waterway, Port, Coastal, and Ocean Engineering* **144**(2): 04017046.
- Balomenos, G.P., Y. Hu, J. E. Padgett, K. Shelton. 2019. "Impact of Coastal hazards on Residents' Spatial Accessibility to Health Services." *ASCE Journal of Infrastructure Systems* **25**(4): 04019028.
- Balomenos, G. P., S. Kameshwar and J. E. Padgett. 2020. "Parameterized fragility models for multi-bridge classes subjected to hurricane loads." *Engineering Structures* **208**: 110213.
- Bea, R., T. Xu, J. Stear and R. Ramos. 1999. "Wave forces on decks of offshore platforms." *Journal of Waterway, Port, Coastal, and Ocean Engineering* **125**(3): 136-144.

- Billah, A. H. M. M. and M. S. Alam. 2016. "Performance-based seismic design of shape memory alloy–reinforced concrete bridge piers. I: Development of performance-based damage states." *Journal of Structural Engineering* **142**(12): 04016140.
- Billah, A. H. M. M. and M. S. Alam. 2021. "Seismic fragility assessment of multi-span concrete highway bridges in British Columbia considering soil–structure interaction." *Canadian Journal of Civil Engineering* **48**(1): 39-51.
- Biondini, F. and M. Vergani. 2015. "Deteriorating beam finite element for nonlinear analysis of concrete structures under corrosion." *Structure and Infrastructure Engineering* **11**(4): 519-532.
- Bocchini, P. and D. M. Frangopol. 2012. "Optimal resilience-and cost-based post disaster intervention prioritization for bridges along a highway segment." *Journal of Bridge Engineering* **17**(1): 117-129.
- Bonakdar, L. and Oumeraci, H., 2015. "Pile group effect on the wave loading of a slender pile: A small-scale model study." *Ocean Engineering* **108**: 449-461.
- Bonakdar, L., H. Oumeraci and A. Etemad-Shahidi. 2015. "Wave load formulae for prediction of wave-induced forces on a slender pile within pile groups." *Coastal Engineering* **102**: 49-68.
- Bradner, C., T. Schumacher, D. Cox and C. Higgins. 2009. Large-scale laboratory measurements of wave forces on highway bridge superstructures. *Coastal Engineering* 2008: (In 5 Volumes), World Scientific: 3554-3566.
- Bruneau, M., S. E. Chang, R. T. Eguchi, G. C. Lee, T. D. O'Rourke, A. M. Reinhorn, M. Shinozuka, K. Tierney, W. A. Wallace and D. Von Winterfeldt. 2003. "A framework to quantitatively assess and enhance the seismic resilience of communities." *Earthquake Spectra* **19**(4): 733-752.
- Cai, Y., A. Agrawal, K. Qu and H. Tang. 2018. "Numerical investigation of connection forces of a coastal bridge deck impacted by solitary waves." *Journal of Bridge Engineering* **23**(1): 04017108.
- Carey, T. J., H. B. Mason, A. R. Barbosa and M. H. Scott. 2019. "Multihazard earthquake and tsunami effects on soil–foundation–bridge systems." *Journal of Bridge Engineering* **24**(4): 04019004.
- Chang, G. and J. Mander. 1994. *Seismic Energy Based Fatigue Damage Analysis of Bridge Columns: Part I-Evaluation of Seismic Capacity*. Technical Report No. NCEER-94-0006.

- Multidisciplinary Center for Earthquake Engineering Research (MCEER), University at Buffalo, New York.
- Chang, S. E. and M. Shinozuka. 2004. "Measuring improvements in the disaster resilience of communities." *Earthquake Spectra* **20**(3): 739-755.
- CHBDC (Canadian Highway Bridge Design Code). 2019. CSA S6:19. CSA Group. Toronto, Ontario.
- Cimellaro, G. P., A. M. Reinhorn and M. Bruneau. 2010. "Framework for analytical quantification of disaster resilience." *Engineering Structures* **32**(11): 3639-3649.
- Dale, V. H., L. A. Joyce, S. McNulty, R. P. Neilson, M. P. Ayres, M. D. Flannigan, P. J. Hanson, L. C. Irland, A. E. Lugo and C. J. Peterson. 2001. "Climate change and forest disturbances: climate change can affect forests by altering the frequency, intensity, duration, and timing of fire, drought, introduced species, insect and pathogen outbreaks, hurricanes, windstorms, ice storms, or landslides." *BioScience* **51**(9): 723-734.
- Dean, R.G. and R. A. Dalrymple. 1991. Water wave mechanics for engineers and scientists. Vol. 2. World Scientific Publishing Company.
- Decò, A., P. Bocchini and D. M. Frangopol. 2013. "A probabilistic approach for the prediction of seismic resilience of bridges." *Earthquake Engineering & Structural Dynamics* **42**(10): 1469-1487.
- Douglas, S. L., Q. Chen, J. M. Olsen, B. L. Edge and D. Borwn. 2006. *Wave forces on bridge decks*. Final Report Prepared for U.S. Department of Transportation and Federal Highway Administration Office of Bridge Technology. Washington, D.C.
- Douglass, S. L., S. Hughes, S. Rogers and Q. Chen. 2004. *The impact of Hurricane Ivan on the coastal roads of Florida and Alabama: A preliminary report*. Report to Coastal Transportation Engineering Research and Education Center, University of South Alabama, Mobile, Alabama. 1-19.
- Dueñas-Osorio, L. and J. E. Padgett. 2011. "Seismic Reliability Assessment of Bridges with User-Defined System Failure Events." *Journal of Engineering Mechanics* **137**(10): 680-690.
- Duncan, J. M. and R. L. Mokwa. 2001. "Passive earth pressures: theories and tests." *Journal of Geotechnical and Geoenvironmental Engineering* **127**(3): 248-257.
- Emanuel, K. 2020. "Evidence that hurricanes are getting stronger." In Proc. of the National Academy of Sciences **117**(24): 13194-13195.

- Ertekin, R. C., M. Hayatdavoodi and J. W. Kim. 2014. "On some solitary and cnoidal wave diffraction solutions of the Green–Naghdi equations." *Applied Ocean Research* **47**: 125-137.
- FEMA. 2013. Federal Emergency Management Agency. Tsunami methodology technical manual. Washington, DC.
- Filippou, F. C., E. P. Popov and V. V. Bertero. 1983. *Effects of bond deterioration on hysteretic behavior of reinforced concrete joints*. Report No UCB/EERC 83-19. University of California Bekeley, California, Earthquake Engineering Research Center.
- Finnemore, E. J. and J. B. Franzini. 2002. Fluid mechanics with engineering applications, McGraw-Hill.
- Frangopol, D. M. and P. Bocchini. 2011. "Resilience as optimization criterion for the rehabilitation of bridges belonging to a transportation network subject to earthquake." In Proc. of Structures Congress 2011, Las Vegas, Nevada.
- Gidaris, I., J. E. Padgett, A. R. Barbosa, S. Chen, D. Cox, B. Webb and A. Cerato. 2017. "Multiple-hazard fragility and restoration models of highway bridges for regional risk and resilience assessment in the United States: state-of-the-art review." *Journal of Structural Engineering* **143**(3): 04016188.
- Godazgar, B., Balomenos, G., Tighe, S. 2022. "Restoration curves for infrastructure: preliminary case study on a bridge in Quebec, Canada." In Proc. of the Institution of Civil Engineers-Bridge Engineering, Thomas Telford Ltd.
- Goel, R. K. and A. K. Chopra. 2008. "Role of Shear Keys in Seismic Behavior of Bridges Crossing Fault-Rupture Zones." *Journal of Bridge Engineering* **13**(4): 398-408.
- Goodnight, J. C., M. J. Kowalsky and J. M. Nau. 2016. "Strain limit states for circular RC bridge columns." *Earthquake Spectra* **32**(3): 1627-1652.
- Goring, D. G. 1978. *Tsunamis--the propagation of long waves onto a shelf*. Report 38. W. M. Keck Laboratory of Hydraulics and Water Resources, California Institute of Technology. Pasadena, CA.
- Gullett, P. M., M.-M Dickey and I. L. Howard. 2012. *Numerical modeling of bridges subjected to storm surge for mitigation of hurricane damage*. Southeast Region Research Initiative (SERRI) Report No. 70015-005, US Department of Homeland Security Directorate.

- Gullett, P. M., M.-M. Dickey and I. L. Howard. 2020. "Finite Element Analysis of Highway Bridges Subjected to Hurricane Storm Surge via the AMBUSH Framework." *Journal of Bridge Engineering* **25**(9): 04020065.
- Günay, S. and K. M. Mosalam. 2013. "PEER performance-based earthquake engineering methodology, revisited." *Journal of Earthquake Engineering* **17**(6): 829-858.
- Guo, A., Q. Fang, X. Bai and H. Li. 2015. "Hydrodynamic experiment of the wave force acting on the superstructures of coastal bridges." *Journal of Bridge Engineering* **20**(12): 04015012.
- Hayatdavoodi, M. and R. C. Ertekin. 2014. *Storm wave forces on selected prototype coastal bridges on the island of Oahu*. Report No. UHMORE-14101. Dept. of Ocean and Resources Engineering, University of Hawaii, Honolulu.
- Hayatdavoodi, M. and R. C. Ertekin. 2015. "Wave forces on a submerged horizontal plate-Part I: Theory and modelling." *Journal of Fluids and Structures* **54**: 566-579.
- Hayatdavoodi, M., K. Treichel and R. C. Ertekin. 2019. "Parametric study of nonlinear wave loads on submerged decks in shallow water." *Journal of Fluids and Structures* **86**: 266-289.
- HAZUS-MH. 2011. Multi-hazard loss estimation methodology: earthquake model HAZUS-MH MR5. Washington, DC.
- HAZUS. 2013. Tsunami Methodology Technical Manual. Federal Emergency Management Agency (FEMA). Washington, DC.
- Henry, A. M. 2011. Wave forces on bridge decks and damping techniques to reduce damages. Master's Thesis, Louisiana State University, Baton Rouge, LA.
- Holland, G. J. 2012. "Hurricanes and rising global temperatures." In Proc. of The National Academy of Sciences of the United States of America, National Academy of Sciences.
- Holling, C. S. 1973. "Resilience and stability of ecological systems." *Annual review of ecology and systematics*: 1-23.
- Holmes, W. T. 2000. "A vision for a complete performance-based earthquake engineering system." In Proc. of 12th World Conference on Earthquake Engineering, Auckland, New Zealand.
- Hong, J., K. Wei and B. Xu. 2021. "Experimental Study of Breaking Wave Loads on Sea-Crossing Bridges Piers." *Earth and Space* 2021: 271-279.
- Huang, B., L. Liao, Q. Ren, X. Cui, J. Zhang and B. Zhu. 2022. "Fragility analysis of the box-girder coastal bridge with different connections subjected to extreme random waves." *Ocean Engineering* **245**: 110580.

- Huang, B., Z. Yang, B. Zhu, J. Zhang, A. Kang and L. Pan. 2019. "Vulnerability assessment of coastal bridge superstructure with box girder under solitary wave forces through experimental study." *Ocean Engineering* **189**: 106337.
- Huang, W. and H. Xiao. 2009. "Numerical modeling of dynamic wave force acting on Escambia Bay Bridge deck during Hurricane Ivan." *Journal of Waterway, Port, Coastal, and Ocean Engineering* **135**(4): 164-175.
- Imamura, F., S. P. Boret, A. Suppasri and A. Muhari. 2019. "Recent occurrences of serious tsunami damage and the future challenges of tsunami disaster risk reduction." *Progress in Disaster Science* **1**: 100009.
- Isaacson, M. and S. Prasad. 1993. "Wave slamming on a horizontal circular cylinder." In Proc. of The Third International Offshore and Polar Engineering Conference, International Society of Offshore and Polar Engineers, Singapore.
- Jin, J. and B. Meng. 2011. "Computation of wave loads on the superstructures of coastal highway bridges." *Ocean Engineering* **38**(17-18): 2185-2200.
- Kafali, C. 2008. System performance under multihazard environment. Ph.D. Thesis, Cornell University, Ithaca, NY.
- Kameshwar, S. and J. E. Padgett. 2014. "Multi-hazard risk assessment of highway bridges subjected to earthquake and hurricane hazards." *Engineering Structures* **78**: 154-166.
- Kanji, G. K. 2006. 100 statistical tests. 3rd Edition, Sage Publications Ltd.
- Kaplan, P. 1992. "Wave impact forces on offshore structures: re-examination and new interpretations." In Proc. of Offshore Technology Conference, Offshore Technology Conference.
- Kaplan, P., J. Murray and W. Yu. 1995. "Theoretical analysis of wave impact forces on platform deck structures." In Proc. of 14th International Conference on Offshore Mechanics and Arctic Engineering. Sponsored by American Society of Mechanical Engineers, Copenhagen, Denmark.
- Kawashima, K. and I. Buckle. 2013. "Structural performance of bridges in the Tohoku-oki earthquake." *Earthquake Spectra* **29**(1_suppl): 315-338.
- King, R. 1987. "The determination of design allowable properties for advanced composite materials." *GEC Journal of Research* **5**(2): 76-87.

- Knabb, R. D., J. R. Rhome and D. P. Brown. 2005. *Tropical cyclone report: Hurricane Katrina, 23-30 august 2005*, National Hurricane Center and Central Pacific Hurricane Center. National Oceanic and Atmospheric Administration.
- Knutson, T. R., J. L. McBride, J. Chan, K. Emanuel, G. Holland, C. Landsea, I. Held, J. P. Kossin, A. Srivastava and M. Sugi. 2010. "Tropical cyclones and climate change." *Nature Geoscience* **3**(3): 157-163.
- Kunnath, S. K., A. El-Bahy, A. W. Taylor and W. C. Stone. 1997. *Cumulative seismic damage of reinforced concrete bridge piers*. Technical Report NCEER 07-0006. Buffalo, NY: US National Center for Earthquake Engineering Research.
- Lehrman, J. B., C. Higgins and D. Cox. 2012. "Performance of highway bridge girder anchorages under simulated hurricane wave induced loads." *Journal of Bridge Engineering* **17**(2): 259-271.
- Li, Y., Y. Dong, D. M. Frangopol and D. Gautam. 2020. "Long-term resilience and loss assessment of highway bridges under multiple natural hazards." *Structure and Infrastructure Engineering* **16**(4): 626-641.
- Lukic, E. A. and C. C. Auditor. 2009. *Review of Hurricane Wilma Expenditures and Reimbursements*. Technical Report 09-04, Office of the County Auditor.
- Marin, J. and D. M. Sheppard. 2009. "Storm surge and wave loading on bridge superstructures." In Proc. of Structures Congress 2009: Don't Mess with Structural Engineers: Expanding Our Role, Austin, Texas.
- Mas, E., J. Bricker, S. Kure, B. Adriano, C. Yi, A. Suppasri and S. Koshimura. 2015. "Field survey report and satellite image interpretation of the 2013 Super Typhoon Haiyan in the Philippines." *Natural Hazards and Earth System Sciences* **15**(4): 805-816.
- McKenna, F., G. Fenves and M. Scott. 2013. "Computer program OpenSees: Open system for earthquake engineering simulation." Pacific Earthquake Engineering Center, University of California, Berkeley, CA. (<http://opensees.berkeley.edu>).
- McPherson, R. L. 2008. Hurricane induced wave and surge forces on bridge decks, Master's Thesis, Texas A & M University, Kingsville, Texas.
- McConnell, K., Allsop, W., and Cruickshank, I. 2004. "Piers, jetties and related structures exposed to waves: guidelines for hydraulic loadings." Thomas Telford, London.

- Megally, S., P. Silva and F. Seible. 2002. *Seismic response of sacrificial shear keys in bridge abutments*. Report No. SSRP-2001/24, Department of Structural Engineering, University of California, San Diego.
- Menegotto, M. and P. Pinto. 1973. "Method of analysis for cyclically loaded reinforced concrete plane force and bending." In Proc. IABSE Symposium on Resistance and Ultimate Deformability of Structures Acted on by Well Defined Repeated Loads, Lisbon.
- Michael, A. S. 1986. Goodness-of-fit techniques, STATISTICS: textbooks and monographs, Marcel Dekker, Inc. New York and Basel.
- Minaie, E. and F. Moon. 2017. "Practical and simplified approach for quantifying bridge resilience." *Journal of Infrastructure Systems* **23**(4): 04017016.
- Mo, W., K. Irschik, H. Oumeraci and P. L.-F. Liu. 2007. "A 3D numerical model for computing non-breaking wave forces on slender piles." *Journal of Engineering Mathematics* **58**(1): 19-30.
- Mohammed, Y. M. and N. Uddin. 2018. "Bridge Resiliency during the Hurricanes." In Proc. of the joint ICVRAM ISUMA UNCERTAINTIES conference, Florianópolis, SC, Brazil.
- Moideen, R., M. Ranjan Behera, A. Kamath and H. Bihs. 2019. "Effect of girder spacing and depth on the solitary wave impact on coastal bridge deck for different airgaps." *Journal of Marine Science and Engineering* **7**(5): 140.
- Montoya, A., A. Matamoros, F. Testik, R. Nasouri, A. Shahriar and A. Majlesi. 2019. "Structural Vulnerability of Coastal Bridges Under Extreme Hurricane Conditions." Project No. 18STTSA04. University of Texas San Antonio. San Antonio, Texas. https://digitalcommons.lsu.edu/transet_pubs/54.
- Mood, A. M., F. A. Graybill and D. C. Boes. 1974. Introduction to the Theory of Statistics 1974, McGraw-Hill Kogakusha.
- Morison, J., J. Johnson and S. Schaaf. 1950. "The force exerted by surface waves on piles." *Journal of Petroleum Technology* **2**(05): 149-154.
- Muthukumar, S. 2003. A contact element approach with hysteresis damping for the analysis and design of pounding in bridges, Ph.D. Thesis, Georgia Institute of Technology, Atlanta, Georgia.
- Nakao, H., G. Zhang, T. Sumimura and J. Hoshikuma. 2013. "Effect of cross-sectional configuration of superstructure on hydrodynamic behavior of bridges subjected to tsunami-induced loading." *Journal of Japan Society of Civil Engineers*, Ser. A 1.

- Nasouri, R., A. Shahriar, A. Matamoros and A. Montoya. 2019. "Evaluating the Hydrodynamic Response of Coastal Bridges during an Extreme Weather Event." In Proc. of MATEC Web of Conferences, EDP Sciences. **271**(1):01002.
- Navaratnam, C. U., A. Tørum and Ø. A. Arntsen. 2013. *Preliminary analysis of wave slamming force response data from tests on a truss structure in large wave flume, Hannover, Germany*. Technical Report No. BAT/MB-R1/2013. Department of Civil and Transport Engineering, Norwegian University of Science and Technology (NTNU), Trondheim, Norway.
- Neumann, B., A. T. Vafeidis, J. Zimmermann and R. J. Nicholls. 2015. "Future coastal population growth and exposure to sea-level rise and coastal flooding-a global assessment." *PloS one* **10**(3): e0118571.
- Nielson, B. G. 2005. Analytical fragility curves for highway bridges in moderate seismic zones, Ph.D. Thesis, Georgia Institute of Technology, Atlanta, Georgia.
- Nielson, B. G. and R. DesRoches. 2007. "Seismic fragility methodology for highway bridges using a component level approach." *Earthquake Engineering & Structural Dynamics* **36**(6): 823-839.
- NOAA (National Oceanic and Atmospheric Administration). 2020. National Data Buoy Center. Accessed September 12, 2020, from <https://www.ndbc.noaa.gov/>.
- Ouyang, M., L. Dueñas-Osorio and X. Min. 2012. "A three-stage resilience analysis framework for urban infrastructure systems." *Structural Safety* **36**: 23-31.
- Padgett, J. E. and R. DesRoches. 2007. "Bridge functionality relationships for improved seismic risk assessment of transportation networks." *Earthquake Spectra* **23**(1): 115-130.
- Padgett, J., R. DesRoches, B. Nielson, M. Yashinsky, O.-S. Kwon, N. Burdette and E. Tavera. 2008. "Bridge damage and repair costs from Hurricane Katrina." *Journal of Bridge Engineering* **13**(1): 6-14.
- Palermo, D., I. Nistor and M. Saatcioglu. 2013. "Tsunami loads on infrastructure." *Encyclopedia of Earth Sciences Series*: 1046-1053.
- Pang, Y., K. Wei and W. Yuan. 2020. "Life-cycle seismic resilience assessment of highway bridges with fiber-reinforced concrete piers in the corrosive environment." *Engineering Structures* **222**: 111120.
- Paulay, T. and M. N. Priestley. 1992. Seismic design of reinforced concrete and masonry buildings. Wiley, New York.

- Priestley, M. N., F. Seible and G. M. Calvi. 1996. *Seismic design and retrofit of bridges*, John Wiley & Sons.
- Qeshta, I. 2019. *Fragility and resilience of bridges subjected to extreme wave-induced forces*, Ph.D. Thesis, RMIT University, Melbourne, Australia.
- Qeshta, I. M., M. J. Hashemi, R. Gravina and S. Setunge. 2019. "Review of resilience assessment of coastal bridges to extreme wave-induced loads." *Engineering Structures* **185**: 332-352.
- Qeshta, I. M., M. J. Hashemi, M. R. Hashemi, R. J. Gravina and S. Setunge. 2021. "Development of fragility functions for rigid-frame bridges subjected to tsunami-induced hydrodynamic forces." *Structure and Infrastructure Engineering*: 1-18.
- Rahman, J. and A. H. M. M. Billah. 2021. "Wave Loading on Bridges: A State-of-The-Art Review." In *Proc. of the Canadian Society of Civil Engineering Annual Conference 2021*, Springer.
- Ramanathan, K. N., 2012. *Next generation seismic fragility curves for California bridges incorporating the evolution in seismic design philosophy*. Ph.D. Thesis, Georgia Institute of Technology, Atlanta, Georgia.
- Robertson, I. N., H. R. Riggs, S. C. Yim and Y. L. Young. 2007. "Lessons from Hurricane Katrina storm surge on bridges and buildings." *Journal of Waterway, Port, Coastal, and Ocean Engineering* **133**(6): 463-483.
- Scott, M. H. and G. L. Fenves. 2006. "Plastic hinge integration methods for force-based beam-column elements." *Journal of Structural Engineering* **132**(2): 244-252.
- Scott, M. H., P. Franchin, G. L. Fenves and F. C. Filippou. 2004. "Response sensitivity for nonlinear beam-column elements." *Journal of Structural Engineering* **130**(9): 1281-1288.
- Seiffert, B., M. Hayatdavoodi and R. Ertekin. 2015. "Cnoidal wave loads on a bridge deck with girders: experiments and computations." *European Journal of Mechanics-B/Fluids* **52**: 191-205.
- Shamsabadi, A., K. M. Rollins and M. Kapuskar. 2007. "Nonlinear soil-abutment-bridge structure interaction for seismic performance-based design." *Journal of Geotechnical and Geoenvironmental Engineering* **133**(6): 707-720.
- Sheppard, D. M. and J. Marin. 2009. *Wave loading on bridge decks: Final Report*. Report No. BD545-58. Florida Department of Transportation, Tallahassee, Florida, United States.

- Shinozuka, M., Y. Zhou, S. Kim, Y. Murachi, S. Banerjee, S. Cho and H. Chung. 2008. *Socio-economic effect of seismic retrofit implemented on bridges in the Los Angeles highway network*. Report No. CA06-0145, California. Dept. of Transportation.
- Shoji, G. and T. Moriyama. 2007. "Evaluation of the structural fragility of a bridge structure subjected to a tsunami wave load." *Journal of Natural Disaster Science* **29**(2): 73-81.
- Stefanidou, S. P. and A. J. Kappos. 2017. "Methodology for the development of bridge-specific fragility curves." *Earthquake Engineering & Structural Dynamics* **46**(1): 73-93.
- Stefanidou, S. P., E. A. Paraskevopoulos, V. K. Papanikolaou and A. J. Kappos. 2022. "An online platform for bridge-specific fragility analysis of as-built and retrofitted bridges." *Bulletin of Earthquake Engineering* **20**(3): 1717-1737.
- Ti, Z., M. Zhang, Y. Li and K. Wei. 2019. "Numerical study on the stochastic response of a long-span sea-crossing bridge subjected to extreme nonlinear wave loads." *Engineering Structures* **196**: 109287.
- US Army. 1984. *Shore Protection Manual (2 Vols)*. US Army Engineer Waterways Experiment Station, Coastal Engineering Research Center, US Government Printing Office, Washington, DC.
- Venkittaraman, A. and S. Banerjee. 2014. "Enhancing resilience of highway bridges through seismic retrofit." *Earthquake Engineering & Structural Dynamics* **43**(8): 1173-1191.
- Vishwanath, B. S. and S. Banerjee. 2019. "Life-cycle resilience of aging bridges under earthquakes." *Journal of Bridge Engineering* **24**(11): 04019106.
- Visser, B. 2019. "Building a better bridge to survive tsunamis." AP News. Accessed June 16, 2022, from <https://apnews.com/article/a86569f1c4a945bf89f1ac3b3704fef3>.
- Wagner, H. D., S. L. Phoenix and P. Schwartz. 1984. "A study of statistical variability in the strength of single aramid filaments." *Journal of composite Materials* **18**(4): 312-338.
- Wang, P., M. Zhao, X. Du and J. Liu. 2019. "Dynamic Response of Bridge Pier under Combined Earthquake and Wave–Current Action." *Journal of Bridge Engineering* **24**(10): 04019095.
- Winter, A. O., M. R. Motley and M. O. Eberhard. 2018. "Tsunami-like wave loading of individual bridge components." *Journal of Bridge Engineering* **23**(2): 04017137.
- Xiong, H., J. Yang and X. Tian. 2020. "An experimental study on the inline wave force on a truncated vertical cylinder." *Ships and Offshore Structures* **15**(1): 39-52.

- Xu, G., C. Cai and L. Deng. 2017. "Numerical prediction of solitary wave forces on a typical coastal bridge deck with girders." *Structure and Infrastructure Engineering* **13**(2): 254-272.
- Zhang, J. and Y. Huo. 2009. "Evaluating effectiveness and optimum design of isolation devices for highway bridges using the fragility function method." *Engineering Structures* **31**(8): 1648-1660.
- Zhang, J., B. Zhu, A. Kang, R. Yin, X. Li and B. Huang. 2020. "Experimental and numerical investigation of wave-current forces on coastal bridge superstructures with box girders." *Advances in Structural Engineering* **23**(7): 1438-1453.
- Zhu, B. and D. M. Frangopol. 2012. "Reliability, redundancy and risk as performance indicators of structural systems during their life-cycle." *Engineering Structures* **41**: 34-49.
- Zhu, D., P. Yuan and Y. Dong. 2021. "Probabilistic performance of coastal bridges under hurricane waves using experimental and 3D numerical investigations." *Engineering Structures* **242**: 112493.
- Zhu, J., W. Zhang and M. Wu. 2018. "Coupled dynamic analysis of the vehicle-bridge-wind-wave system." *Journal of Bridge Engineering* **23**(8): 04018054.

Appendices

Appendix A

Table A. Equations developed for wave load estimation

AASHTO Guide Specifications for Bridges Vulnerable to Coastal Storms (AASHTO 2008)

First Case:

$$F_{V-MAX} = \gamma_w \bar{W} \beta \left(-1.3 \frac{H_{max}}{d_s} + 1.8 \right) \cdot [1.35 + 0.35 \tanh(1.2(T_p) - 8.5)] \cdot \left(b_0 + b_1 x + \frac{b_2}{y} + b_3 x^3 + \frac{b_4}{y^2} + \frac{b_5}{y} + b_6 x^3 \right) \cdot TAF$$

Vertical slamming force:

$$F_S = A \gamma_w H_{max}^2 \left(\frac{H_{max}}{\lambda} \right)^B$$

Associated horizontal force:

$$F_{H-AV} = \gamma_w H_{max}^2 (a_0 + a_1 x + a_2 x^2 + a_3 x^3 + a_4 x^4 + a_5 x^5 + a_6 \ln(y)) \left[a_7 + a_8 \left(\frac{W}{\lambda} \right) \right]$$

Associated overturning moment:

$$M_{T-AV} = [F_{V-MAX} W^* + F_{H-AV} (d_b + r)] \left\{ a_m + \frac{b_m}{\left(\frac{W}{\lambda} \right)} + \frac{c_m}{\left(\frac{H_{max}}{\lambda} \right)} \right\} + \frac{2F_S W^*}{3}$$

Second Case:

$$F_{H-MAX} = \gamma_w \pi (d_b + r) (\omega + \frac{1}{2} H_{max}) \left(\frac{H_{max}}{\lambda} \right) e^{-3.18 + 3.76 e^{\left(\frac{\omega}{\lambda} \right)} - 0.95 \left[\ln \left(\frac{\eta_{max} - Z_c}{d_b + r} \right) \right]^2}$$

Associated vertical force:

$$F_{V-AH} = \gamma_w \alpha (\eta_{max} - Z_c) e^{[-0.3 + 2.04 e^{-9.01 \left(\frac{\alpha}{\lambda} \right)} - 0.16 \left(\frac{\eta_{max} - Z_c}{d_b} \right)^2]}$$

Associated overturning moment:

$$M_{T-AH} = \left[F_{H-MAX} (d_b + r) + \frac{2}{3} (F_{V-AH} + F_S) W \right] 1.37 \tanh \left(\frac{d_b}{\eta_{max} - Z_c} \right)$$

here,

F_{V-MAX} = vertical maximum hydrostatic force, F_{H-MAX} = horizontal maximum hydrostatic force γ_w = unit weight of water, H_{max} = maximum wave height, d_s = water depth, T_p = wave period, TAF = trapped air factor, λ = wave length, W = width of the deck, W^* = effective deck width, d_b = height of girder plus deck thickness, r = rail height, \bar{W} , β , B , A , a_0 - a_6 , b_0 - b_6 are coefficients based on clearance, wave length, wave crest elevation and deck width.

ASCE 7-16 (2016)

Force load due to breaking waves:

$$F_D = 0.5 \gamma_w C_D D H_b^2$$

$$H_b = 0.78 d_s$$

$$d_s = 0.65 (BFE - G)$$

$$F = \frac{\pi W V_b C_I C_O C_D C_B R_{max}}{2g\Delta t}$$

$$V_1 = d_s / (1 \text{ sec})$$

$$V_2 = (gd_s)^{0.5}$$

here,

γ_w = unit weight of water, C_D = drag coefficient of breaking waves, H_b = breaking wave height, d_s = local still water depth, BFE = base flood elevation and G = ground elevation, F = impact load, W = debris weight,

V_b = velocity of debris, g = acceleration due to gravity, Δt = impact duration, C_I = importance coefficient,

C_O = orientation coefficient, C_D = depth coefficient, C_B = blockage coefficient, R_{max} = maximum response ratio for impulsive load, V_1 and V_2 = average velocities of water.

Gullett et al. (2012)

Wavelength,

$$L = \frac{g}{2\pi} T^2 \tanh \frac{2\pi}{L} d$$

Buoyancy force,

$$F_b = \rho g V_s$$

Slamming force,

$$F_{sx} = 0.5 C_s \rho A_x u^2$$

$$F_{sy} = 0.5 C_s \rho A_y w^2$$

Drag force,

$$F_{dx} = 0.5 C_{dx} \rho A_x u^2$$

$$F_{dy} = 0.5 C_{dy} \rho A_y w^2$$

Inertial drag force,

$$F_{ix} = \rho C_{mx} V_s \dot{u}$$

$$F_{iy} = \rho C_{my} V_s \dot{w}$$

here,

ρ = mass density of water, V_s = submerged volume of bridge F_{sx} and F_{sy} = slamming force in the horizontal and vertical directions, C_s = slamming coefficient, A_x and A_y = projected area of wave crest impact on the vertical and horizontal planes, F_{dx} and F_{dy} = drag force in the horizontal and vertical directions, C_{dx} and C_{dy} = horizontal and vertical drag coefficients, F_{ix} and F_{iy} = horizontal and vertical inertial drag forces, C_{mx} and C_{my} = horizontal and vertical inertia coefficients.

Wang et al. (2019)

$$P_1 = \frac{\rho g H_w}{2 \cosh kh} \left[1 - \frac{\omega_2 k^2 H_w^2}{2(kU_0 - \omega_0)} \right]$$

$$P_2 = \frac{3\rho H_w^2}{8} \left[\frac{w_0(w_0 - kU_0)}{2 \sinh^4(kh)} - \frac{gk}{3 \sinh 2kh} \right]$$

$$P_3 = \frac{3\rho k H_w^3 \omega_0 (\omega_0 - kU_0) (9 - 4\sinh^2 kh)}{512 \sinh^7(kh)}$$

$$\omega_* = \omega_0 + (kH_w)^2 \omega_2$$

$$\omega_0 = kU_0 + \sqrt{gk \tanh kh}$$

$$\omega_2 = \frac{(9 + 8\sinh^2 kh + 8\sinh^4 kh)}{64\sinh^4} (\omega_0 - kU_0)$$

Force per unit length in the horizontal and vertical direction,

$$f_x^w = -\cos \alpha \sum_{j=1}^3 \frac{4}{jk} P_j \cosh jkz A(jka) \sin(\omega_* t - \varphi_j)$$

$$f_y^w = -\sin \alpha \sum_{j=1}^3 \frac{4}{jk} P_j \cosh jkz A(jka) \sin(\omega_* t - \varphi_j)$$

$$A(jka) = 1 / \sqrt{[J_1'(jka)]^2 + [Y_1'(jka)]^2}$$

$$\tan(\varphi_j) = J_1'(jka) / Y_1'(jka)$$

here,

U_0 = current velocity, ω_* = incident wave angular velocity, P_j = pressure of the incident wave, J_n = Bessel function of order n of first kind, Y_n = Bessel function of second kind of order n , φ_i = lagging angle.

Zhu et al. (2018)

Surface elevation along the wave propagation

$$\eta(y, t) = \sum_{i=1}^{N_f} a_i \cos(k_i y - \tilde{\omega}_i t + \varepsilon_i)$$

$$a_i = \sqrt{2S_\eta(\omega_i) \Delta\omega}$$

$$\omega_i = [i\Delta\omega + (i-1)\Delta\omega]$$

$$\omega_i^2 = k_i g \tanh(k_i h)$$

$$\Delta\omega = (\omega_{\max} - \omega_{\min}) / N_f$$

$$k_i = 2\pi / \lambda_i$$

here,

N_f = number of frequencies, a_i = the wave amplitude of each wave component, S_η = wave spectrum, $\Delta\omega$ is the frequency resolution, ω_{\min} and ω_{\max} are the lower and upper cutoff frequencies, $\tilde{\omega}_i$ = frequency of the i^{th} wave, k_i = wave number, h = water depth, λ_i = wavelength of the i^{th} wave, g = acceleration due to gravity,

$\varepsilon_i = N_f$ sequences of the independent random phase angles distributed uniformly over the interval $[0, 2\pi]$.

Water particle velocity in the direction of propagation at time t :

$$u_x(y,z,t) = \sum_{i=1}^{N_f} a_i \tilde{\omega}_i \frac{\cosh k_i(h+z)}{\sinh k_i h} \cos(k_i y - \tilde{\omega}_i t + \varepsilon_i)$$

Water particle acceleration in the direction of propagation at time t :

$$\dot{u}_x(y,z,t) = \sum_{i=1}^{N_f} a_i \tilde{\omega}_i^2 \frac{\cosh k_i(h+z)}{\sinh k_i h} \sin(k_i y - \tilde{\omega}_i t + \varepsilon_i)$$

Following the Morrison equation (Morison et al. 1950):

$$F_{wave} = \frac{1}{2} \rho_w C_{wD} D (u_w - u_b) |u_w - u_b| + \rho_w A \dot{u}_w + (C_{wM} - 1) \rho_w A (\dot{u}_w - \dot{u}_b)$$

here,

C_{wD} and C_{wM} = drag and inertia coefficients taken as 1.2 and 1.5 from AASHTO (2008), ρ_w = density of water, D and A diameter and section area of the pile respectively.

Appendix B

Table B1. Wave load IMs generated from LHS

Wave ID	Wave Period, T_w (sec)	Wave Height, H_w (m)	Still Water Depth, d_s (m)
W1	8.23	3.84	8.64
W2	13.18	7.21	8.04
W3	3.60	2.04	6.24
W4	4.27	3.42	8.04
W5	3.37	3.30	7.38
W6	9.77	6.43	8.50
W7	6.62	8.84	9.10
W8	7.38	8.58	14.44
W9	3.59	3.30	5.20
W10	3.59	3.62	8.04
W11	3.59	3.37	8.57
W12	3.59	3.42	7.38
W13	12.78	12.61	8.74
W14	9.34	11.93	7.06
W15	11.81	8.97	7.48
W16	13.09	15.33	6.88
W17	4.27	3.30	8.57
W18	4.27	3.62	6.24
W19	4.27	3.37	7.38
W20	4.27	2.04	5.20
W21	13.25	10.80	8.45
W22	12.74	12.70	8.52
W23	9.13	10.10	9.77
W24	8.19	9.56	8.47
W25	8.55	9.56	9.73
W26	3.37	3.62	5.20

Table B1 Continued.

Wave ID	Wave Period, T_w (sec)	Wave Height, H_w (m)	Still Water Depth, d_s (m)
W27	3.37	3.37	8.04
W28	3.37	3.42	6.24
W29	11.46	12.87	8.13
W30	12.60	9.06	7.20
W31	4.33	4.30	7.70
W32	4.33	4.64	3.55
W33	4.33	3.61	7.11
W34	13.71	11.94	7.61
W35	9.70	9.01	8.48
W36	12.73	9.66	5.74
W37	12.99	12.70	6.86
W38	10.42	11.25	7.55
W39	8.63	11.12	6.98
W40	11.56	15.17	6.09
W41	6.63	9.14	6.91
W42	10.11	12.90	6.97
W43	8.37	9.34	7.37
W44	12.81	13.45	6.44
W45	10.32	6.65	7.08
W46	11.38	10.92	5.91
W47	10.87	13.03	7.22
W48	9.61	13.91	9.52
W49	13.09	9.47	7.06
W50	10.92	16.00	7.83
W51	7.43	7.08	7.56
W52	12.21	12.09	5.37
W53	10.58	9.17	15.25

Table B1 Continued.

Wave ID	Wave Period, T_w (sec)	Wave Height, H_w (m)	Still Water Depth, d_s (m)
W54	8.96	7.48	16.50
W55	12.61	7.37	7.17
W56	9.84	11.92	9.89
W57	9.07	12.10	9.71
W58	9.07	7.98	10.08
W59	4.61	3.28	8.64
W60	4.61	4.34	14.80
W61	4.61	3.84	7.94
W62	4.61	3.04	15.37
W63	3.37	1.87	8.64
W64	3.37	3.28	4.80
W65	3.37	4.34	7.94
W66	3.37	3.84	5.37
W67	3.37	3.04	4.50
W68	9.07	7.98	10.08
W69	13.09	8.02	15.58
W70	11.57	11.67	12.82
W71	13.42	10.72	8.80
W72	7.46	11.52	8.33
W73	11.95	6.79	7.42
W74	10.38	6.58	11.93
W75	12.92	6.21	15.22
W76	11.96	9.25	7.54
W77	7.92	11.74	5.31
W78	13.08	14.19	7.66
W79	8.16	7.13	11.00
W80	6.12	9.80	7.43

Table B1 Continued.

Wave ID	Wave Period, T_w (sec)	Wave Height, H_w (m)	Still Water Depth, d_s (m)
W81	13.11	6.93	13.36
W82	9.11	10.13	8.12
W83	8.60	9.61	15.00
W84	10.14	5.43	14.62
W85	9.40	9.10	15.22
W86	7.74	9.31	7.11
W87	8.55	7.71	7.07
W88	11.79	9.47	6.74
W89	13.50	12.76	7.27
W90	9.84	11.05	8.21
W91	6.54	5.53	13.89
W92	12.03	9.00	7.44
W93	7.52	11.28	9.43
W94	9.73	10.00	9.51
W95	8.66	7.72	8.89
W96	10.18	10.56	5.13
W97	10.13	7.79	9.12
W98	9.21	7.58	5.47
W99	13.75	6.22	9.95
W100	6.38	9.34	8.47

Table B2. Bridge model parameters generated from LHS

Bridge ID	f_c' (MPa)	f_y (MPa)	ρ_s (%)
B1	33.68	375.36	1.41
B2	43.89	394.16	1.27
B3	36.00	453.50	1.16
B4	30.54	574.03	1.13
B5	33.12	479.19	1.17
B6	35.92	461.62	1.26
B7	34.23	474.01	1.43
B8	40.87	441.29	1.33
B9	31.51	401.99	1.22
B10	32.15	510.60	1.33
B11	38.16	493.66	1.40
B12	33.41	484.45	1.47
B13	42.21	501.37	1.17
B14	38.85	458.59	1.20
B15	34.48	397.13	1.26
B16	36.16	458.55	1.48
B17	39.21	469.33	1.34
B18	37.73	423.05	1.47
B19	38.14	400.70	1.36
B20	34.93	412.18	1.23